学位論文

Simulation Study of Astrophysical Shocks Mediated by Cosmic Rays

(宇宙線の影響を受けた天体衝撃波
についてのシミュレーション研究)

平成27年12月博士 (理学)　申請

東京大学大学院理学系研究科
地球惑星科学専攻
斎藤　達彦

DOCTORAL THESIS

Simulation Study of Astrophysical Shocks Mediated by Cosmic Rays

Tatsuhiko Saito

Space and Planetary Science Group
Department of Earth and Planetary Science
Graduate School of Science, The University of Tokyo

December, 2015

Abstract

Galactic cosmic rays (GCRs) are believed to be accelerated at the shockwaves of supernova remnants (SNRs) in our galaxy. The diffusive shock acceleration (DSA), which is known as the first-order Fermi acceleration, is the standard theory to explain the particle acceleration at the shocks, and have a good agreement with the observed power-law energy spectrum. It is known that the spectral index for the power-law spectrum can be determined only by the shock compression ratio. Although the standard DSA theory assumed that not only the cosmic ray (CR) density but also the energy density is negligible compared with the thermal gas (test-particle assumption), several recent observations suggest that the energy densities of CRs around the shocks are not necessarily negligible, and can be more or less comparable to those of the background plasma. In such a situation, the dynamical feedback effect of the CRs should be taken into account. Since the CR pressure has a spatial gradient in front of the shocks, the flow structures of the background plasma are modified drastically, and then the total shock compression ratio may increase. As the result, CRs can be accelerated more efficiently than the test-particle limit of DSA. This acceleration mechanism is known as the nonlinear DSA (NLDSA), and the modified shocks in NLDSA are called as the cosmic ray modified shocks (CRMSs). The CR production rate in NLDSA is thought to be optimistically enhanced, simply because the larger population of CRs can make shocks more compressive and the spectrum more harder. Such a positive feedback effect, however, might not be permitted in the nature of physics. Our main purpose of this study is to address the question how efficiently the NLDSA can produce CRs.

In this thesis, two important issues on cosmic ray physics are investigated: one is the stability/stationarity of the non-linear shock in a fluid approximation. The other is to understand the

kinetic plasma process in the non-linear shock beyond the fluid approximation. It is well known that the CRMSs have the multiple (up to three) steady-state solutions for a given upstream parameter. These three solutions are different in the CR production efficiency, and one of the solutions with the maximum efficiency is believed to be realized, for example, in the supernova shocks. As the first step to understand the nature of CRMSs, we investigate the stability of these solutions in the two-fluid approach, where both of the thermal gas and non-thermal CRs are approximated by fluids. By the numerical simulations for a set of two-fluid, time evolutional equations, we find that two solutions/branches with the maximum and minimum CR efficiencies and stable, while the intermediate branch is unstable in time, and this stability features are independent of any shock parameters. We also study the time evolution of the CR production and find that only the inefficient branch with the minimum CR production is realized among three multiple solutions. Our findings suggest that the CR production efficiency of CRMSs is less efficient than believed before. We can conclude that the production of CRs plays a role of negative feedback in NLDSA.

Next, we extend the above two-fluid model by taking into account of the momentum-dependent CR kinetic effects. This model is called CR-kinetic model, and enables us to discuss about the spectrum of the CRs that can be compared with cosmic ray observations. In addition, we investigate the effect of Alfvénic waves excitation on NLDSA, which is believed to play an important role in NLDSA. In the shock precursor region where the CRs are streaming upstream, the streaming CRs have a free energy that can excite the Alfvénic waves through a current-driven plasma instability. The energy density for these excited waves may become comparable to or not be negligible to that of the thermal background plasma. Hence, we should take into account the feedback from the amplified waves as the essential behavior of CRMSs. We include the elementary processes of the wave generation and dissipation model in the CR-kinetic system, and study the steady-state solutions with our own semi-analytical methods. Our numerical parameter surveys about the steady-state solutions clearly reveal that the wave pressure effect reduces the CR production by suppressing the shock compression ratio. Moreover, the heating of the background plasma in the precursor region by the dissipation of waves leads to

the further depression of the CR production efficiency. Such tendencies are robust regardless of the Mach numbers, the injection parameters and the wave parameters, such as Alfvén velocities and subshock compression ratios for the waves. These results conclude that the CR production is less efficient than the "standard" (without consideration of waves) NLDSA predicts.

Finally, our findings suggest that the negative feedback process involved in NLDSA may be carefully taken into account in the theoretical/observational studies for collisionless shocks such as supernova shocks and Interplanetary shocks and so on.

Acknowledgments

First of all, the author deeply grateful to his supervisor in the master and doctoral course in The University of Tokyo, Prof. Masahiro Hoshino, for his enthusiastic guidance and continuous encouragement. The author has learned innumerable things required to conduct academic research from him, not only the scientific knowledge of the astrophysical plasma, but also the sincere attitudes for the logicality and the natural sciences. This thesis could not finished without his direction.

The author would also like to thank Dr. Takanobu Amano who have given him the insightful comments and suggestions. Discussions with him were invaluable aid to his research and this thesis.

The author sincerely thanks to Prof. M. Fujimoto, Prof. T. Yokoyama, Prof. T. Terasawa, Prof. T. Imamura, Prof. T. Shimizu, Prof. N. Iwagami, Prof. K. Seki, Prof. S. Sugita, and Prof. I. Yoshikawa for their valuable suggestions. The author would also like to express the gratitude to Dr. M. Takamoto, Dr. K. Shirakawa, Dr. K. Higashimori, K. Hirabayashi, M. Iwamoto, R. Yoshitake, and M. Hirai for the helpful comments and support.

Contents

List of Figures

List of Tables

Chapter 1

GENERAL INTRODUCTION

1.1 History and Observations of Cosmic Rays

Cosmic ray (CR) is the generic name of high energy particles coming from space. These particles collide with the atoms or molecules of the earth's atmosphere and generate many photons and elementary particles, which are called the secondary cosmic rays. In 1912, Victor Hess discovered the existence of these particles [Hess, 1912]. About 90% of the primary CRs are protons, 9% are alpha particles and 1% are heavier ions and electrons (electron/proton number ratio in the primary CRs $K_{ep} \sim 10^{-2}$). Figure 1.1 shows the energy spectra of CRs measured by the satellites and ground based observations (from Amato [2014]). The CR energy spectrum is nearly a power law ranging from $10^9\,\mathrm{eV}$ to about $10^{20}\,\mathrm{eV}$. The spectrum is described $\propto E^{-2.7}$ up to $(3-5)\times 10^{15}\,\mathrm{eV}$ which is called "knee". After the knee, the spectrum steepens, $\propto E^{-(3.0-3.2)}$ until $3\times 10^{18}\,\mathrm{eV}$ which is called "ankle". Over the ankle, we detect higher energy up to about $4\times 10^{19}\,\mathrm{eV}$ (so-called Greisen-Zatsepin-Kuzumin (GZK) cut-off energy), energy at which particles begin to interact with the cosmic microwave background (CMB) photons and to be suppressed. CRs with energies below the knee are called "Galactic cosmic rays (GCRs)", because their origin is thought to be in our Galaxy. On the other hand, CRs whose energies are above the knee are thought to be of extragalactic origin. Possible candidates of these extragalactic CRs include such as active galactic nuclei (AGN), clusters of galaxies, or radio galaxies.

From the early age of CR research history, the shock waves driven by supernova explosions

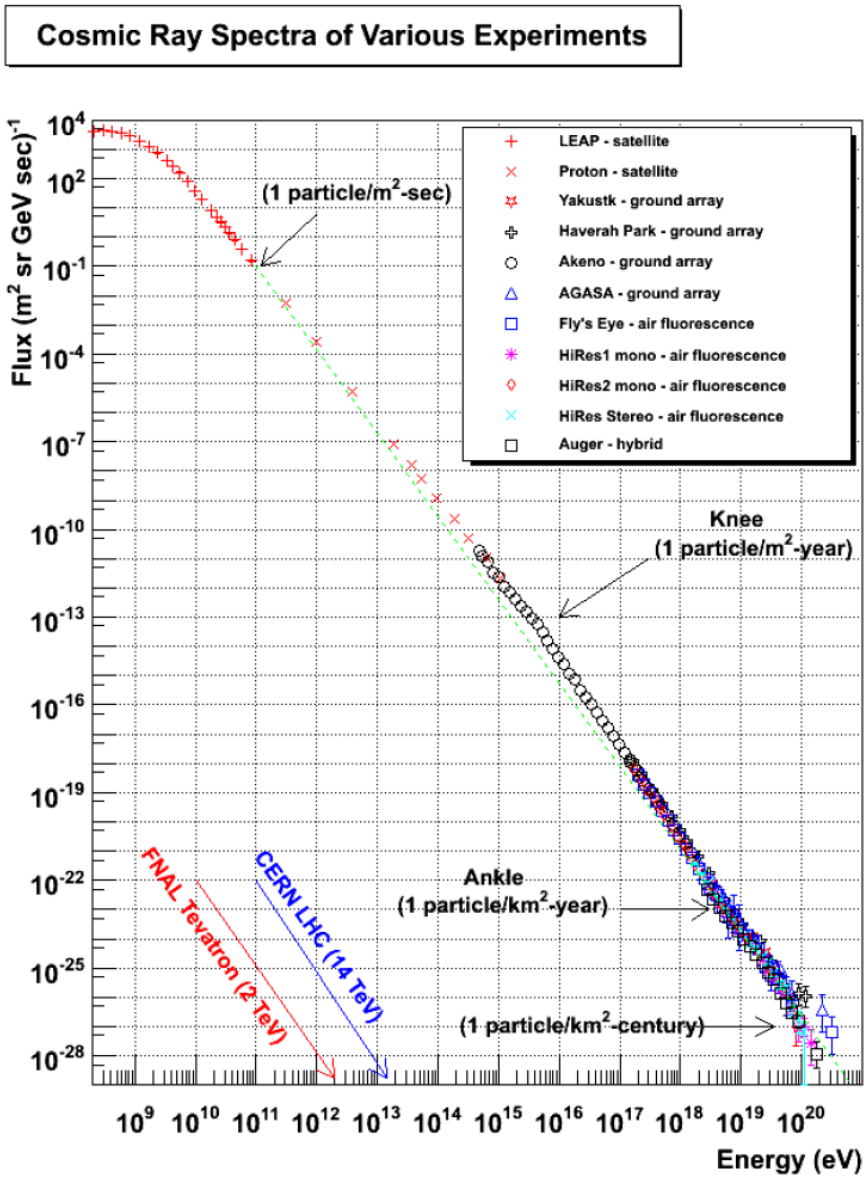

Figure 1.1: Energy spectrum of CRs measured by various experiments (from Blasi [2013]; Amato [2014]). The horizontal axis means the energies of each CR particles and vertical axis means the number fluxes. Each symbol means the results of experiments.

have been considered as the reliable origins of GCRs. After the explosions, there are nebulae left, which are called supernova remnants (SNRs). The average kinetic energy released by supernova explosions is $\sim 10^{51}\,\mathrm{erg}$. A supernova rate is estimated to be about 2 times per century [van den Bergh and Tammann, 1991]. This leads to the energy input rate $\sim 6 \times 10^{41}\,\mathrm{erg/s}$. On the other hands, the average energy density of CRs confined in our galaxy is typically $\sim 1\,\mathrm{eV/cm^3}$ [Gaisser, 1990] that is comparable to that of the magnetic fields and CMB photons. Since the volume of our galaxy is about $10^{67}\,\mathrm{cm^3}$, the total energy of GCRs is $\sim 10^{67}\,\mathrm{eV}$. The lifetime of these GCRs is equal to the confinement time, which has been estimated by the isotope $^{10}\mathrm{Be}$ generated by the spallation of CR carbon and oxygen near the SNRs. From the comparison of the abundance of $^{10}\mathrm{Be}$ around SNRs with that of near the earth, the escape time can be inferred as $\sim 10^{7}\,\mathrm{yr}$. Then, the required CR production rate is $\sim 5 \times 10^{40}\,\mathrm{erg/s}$. This is satisfied if about 10% of the supernova explosion energy is converted into the energy of GCRs and there is no candidates in our galaxy other than supernova explosions that can provide such large energies. There is increasing evidences that suggest the above hypothesis is indeed correct.

SNRs are classified into three categories based on the radio morphology, i.e. "Shell-type", "Filled-center" and "Composite". Shell-type SNRs have bright rings that corresponds to the expanding shock fronts, and filled-center SNRs have the pulsars at the center of the remnants and bright nebula called as "Pulsar Wind Nebula (PWN)". Composite SNRs show the features of the both types. Most SNRs, about 79% of the known SNRs in out galaxy, are categorized into Shell-type [Green, 2014]. Figure 1.2 shows one of the typical examples of Shell-type SNRs, which is the remnant of the supernova explosion in 1006, therefore, called as SN 1006. This is the X-ray image by Chandra X-ray observatory. At the northeast and southwest rims (the upper left and lower right in the figure), the brightest X-ray radiations are observed (blue color in the figure), which are the emissions from the relativistic CR electrons. Not only in X-ray band, but also in the broad range from radio to γ-ray, radiations from non-thermal (relativistic) particles have been detected in the observations of SNRs.

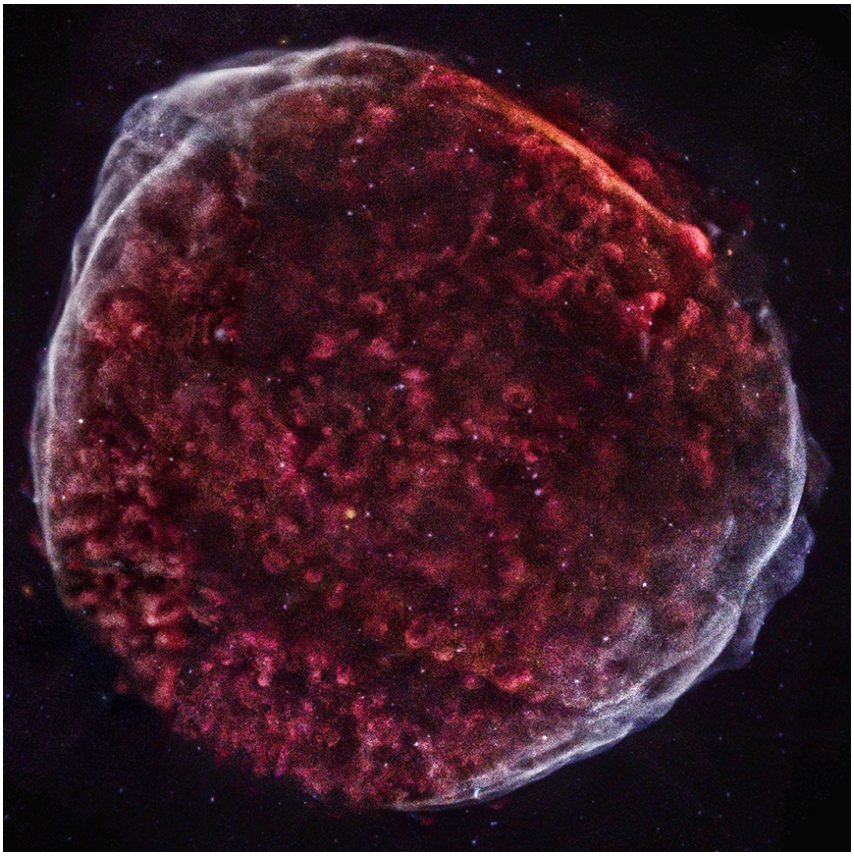

Figure 1.2: X-ray image of the SN1006 by Chandra (Courtesy of NASA/CXC/SAO). Colors show the different energies of X-ray photons (red: $0.50-0.91\,\mathrm{keV}$, cyan: $0.91-1.34\,\mathrm{keV}$, blue: $1.34-3.00\,\mathrm{keV}$).

1.1.1 Radiation processes of CRs

The emission process related to the non-thermal particles are summarized as follows. Relativistic electrons produce non-thermal emissions by synchrotron radiation, non-thermal bremsstrahlung and Inverse Compton (IC) scattering. Synchrotron radiation is emitted by relativistic electrons in the gyro-motion around the magnetic fields. Typical magnetic fields in the interstellar medium (ISM) $\sim 3\,\mu\mathrm{G}$, which shows the almost equal energy density to that of the GCRs in our galaxy ($\sim 1\,\mathrm{eV/cm^3}$) [Gaisser, 1990]. Synchrotron radiation can be detected from the radio to X-ray bands for such a strength of magnetic fields. Radiations by non-thermal bremsstrahlung and Inverse Compton (IC) scattering are observed in the X-ray $\sim \gamma$-ray band. Bremsstrahlung (or free-free emission) occurs when the relativistic electrons are scattered by the ions or electrons. IC scattering is a process where relativistic electrons conflict with low-energy photons, and produce high-energy emission. This is an opposite case of Compton scattering where the

high-energy photons conflicts with the low-energy electrons. On the other hand, emissions from the non-thermal protons are thought to be generated by nuclear reaction. Collisions of relativistic protons and the ambient proton (or nucleus) in ISM generate a neutral pion (π^0) through nuclear reaction $p+p \to \pi^0$. Subsequently, γ-ray photons are generated via π^0 decays. This γ-ray emission is called a "hadronic" process in contrast with a "leptonic" process by bremsstrahlung and IC due to the relativistic electrons.

A relativistic electron with the energy E emits the synchrotron radiation at the critical frequency ν_c defied as

$$\nu_c = \frac{3}{2}\frac{eB\sin\alpha}{2\pi m_e c}\left(\frac{E}{m_e c^2}\right)^2 \sim 16.08\left(\frac{B}{\mu\mathrm{G}}\right)\left(\frac{\sin\alpha}{1}\right)\left(\frac{E}{\mathrm{GeV}}\right)^2 \mathrm{MHz}. \tag{1.1}$$

α is the pitch angle between the electron's velocity vector and the magnetic field. At this critical frequency, a photon has the energy $E_{p,sync}$:

$$E_{p,sync} = h\nu_c \sim 6.65\times10^{-8}\left(\frac{B}{\mu\mathrm{G}}\right)\left(\frac{\sin\alpha}{1}\right)\left(\frac{E}{\mathrm{GeV}}\right)^2 \mathrm{eV}. \tag{1.2}$$

The frequency (and the photon energy) depends on the energy of the electron and the strength of the local magnetic field. When B is equal to the typical value of the interstellar magnetic fields (a few μG), the electrons with the GeV energies emit the synchrotron radiation in radio band: the frequencies of $\mathrm{MHz}-\mathrm{GHz}$ (or the photon energies of $10^{-8}-10^{-3}\,\mathrm{eV}$). Electrons with TeV energies can be detected in X-ray band: the photon energies of $\sim\mathrm{keV}$. If the non-thermal electrons are assumed to be in power-law distributions, $N(E)\propto E^{-s}$, the spectra of the synchrotron radiation also become power-law, i.e. energy flux $F(\nu)$ per unit frequency ν is described as $F(\nu)\propto\nu^{-\alpha}$. The index α is expressed by the formula $\alpha=(s-1)/2$. The energy loss rate P_{sync} of electrons emitting the synchrotron radiations is

$$\begin{aligned} P_{sync} &\sim \frac{4}{3}\left(\frac{8\pi e^4}{3m_e^2c^4}\right)c\left(\frac{B^2}{8\pi}\right)\left(\frac{E}{m_e c^2}\right)^2 \\ &\sim 4.06\times10^{-21}\left(\frac{B}{\mu\mathrm{G}}\right)^2\left(\frac{E}{\mathrm{GeV}}\right)^2 \mathrm{erg/s}, \end{aligned} \tag{1.3}$$

and the cooling time τ_{cool} of relativistic electrons by the synchrotron radiations is

$$\tau_{cool} \sim \frac{E}{P_{sync}} \sim 1.25 \times 10^{10} \left(\frac{B}{\mu \mathrm{G}} \right)^{-2} \left(\frac{E}{\mathrm{GeV}} \right)^{-1} \mathrm{yr}. \tag{1.4}$$

Under a few μG magnetic fields, the cooling time is sufficiently large.

An electron whose energy is E typically emits the bremsstrahlung photon of the energy $E_{p,brems} \sim E/3$. Therefore, suprathermal electrons of $10-1000\,\mathrm{keV}$ are responsible for the hard X-ray, where the photon energy is over $10\,\mathrm{keV}$, and relativistic electrons of MeV-TeV energies that cause synchrotron radiation in radio - X-ray bands, contribute to the γ-ray photons. Non-thermal bremsstrahlung from relativistic electrons is distinguished from thermal bremsstrahlung by thermal Maxwellian electrons, which shows the flat photon spectrum independent from the frequencies in the radio band. It has power-law distributions, expressed by $F(\nu) \propto \nu^{1-s}$, when the relativistic electrons are in $N(E) \propto E^{-s}$.

The energy of the IC photon $E_{p,IC}$ becomes maximum at the frequency ν_{max}:

$$\nu_{max} \sim 4 \left(\frac{E}{m_e c^2} \right) \nu_0 \sim 2.50 \times 10^{12} \left(\frac{E}{\mathrm{GeV}} \right)^2 \left(\frac{\nu_0}{\nu_{CMB}} \right) \mathrm{MHz}, \tag{1.5}$$

and

$$(E_{p,IC})_{max} \sim 1.03 \times 10^4 \left(\frac{E}{\mathrm{GeV}} \right)^2 \left(\frac{\nu_0}{\nu_{CMB}} \right) \mathrm{eV} \tag{1.6}$$

where ν_0 and ν_{CMB} are the frequency of incident, unscattered photon and the peak frequency of CMB ($\nu_{CMB} = 1.6 \times 10^{11}\,\mathrm{Hz}$), which is the most likely candidate for seed photons scattered by relativistic electrons, respectively. When CMB photons are scattered by $1\,\mathrm{GeV}$ electrons, the scattered photons become keV energy photons, i.e. X-ray photons. Spectrum of IC photons is $F(\nu) \propto \nu^{-(s-1)/2}$, which shows the same index as that of the synchrotron radiation, and this power-law spectrum continues up to ν_{max}, then has an exponential cut-off after the frequency.

The energy loss rate of the electrons P_{IC} by IC scattering is

$$P_{IC} \sim \frac{4}{3}\left(\frac{8\pi e^4}{3m_e^2c^4}\right) cU_{rad}\left(\frac{E}{\mathrm{GeV}}\right)^2 \mathrm{erg/s}. \tag{1.7}$$

U_{rad} is the energy density of the radiation.

Emissions by π^0 decay are detected only in the γ-ray band, where the photons energies are MeV-TeV. The creation of π^0 by the reaction $p+p \to \pi^0$ occurs when the energies of the CR protons are above $1.2\,\mathrm{GeV}$. π^0 quickly decays into two γ-ray photons ($\pi_0 \to 2\gamma$), whose energies are $m_{\pi^0}c^2/2 \sim 67.5\,\mathrm{MeV}$ in the rest frame of π_0, where m_{π^0} is the mass of the neutral pion. In the lab frame, the photons have roughly one-tenth the energies of the parent CR protons. The resulting spectrum is $F(\nu) \propto \nu^{1-s}$ when the parent CR protons are in the power-law distribution: $N(E) \propto E^{-s}$, and it has the characteristic low-energy cut-off around $0.1\,\mathrm{GeV}$.

Typical examples of the shape of the spectra described above are shown in Figure 1.3, which indicates the broadband spectral energy distribution of Tycho's SNR [Giordano et al., 2012]. Each line means the different radiation models: synchrotron radiation, IC scattering of CMB, non-thermal bremsstrahlung, π_0 decay and the sum of the four. Horizontal axis means the photon energy $E(=h\nu)$, and the vertical axis means the photon energy flux $E^2dN/dE(=\nu F(\nu))$, where N is the photon flux in the interval energy dE, therefore this map is qualitatively equal to the $\nu - \nu F(\nu)$ map. The power-law indices of both of CR electrons and protons are assumed to be 2.3 ($N(E) \propto E^{-2.3}$). The spectrum of the synchrotron radiations that continues from the radio to the X-ray (keV photons) is $\nu F(\nu) \propto \nu^{-(s-3)/2} \propto \nu^{0.35}$, and IC has the same index ($\nu F(\nu) \propto \nu^{0.35}$) but is seen in the different energies (X-ray - TeV γ-ray). Non-thermal bremsstrahlung (X-ray - TeV γ-ray) has slope $\nu F(\nu) \propto \nu^{2-s} \propto \nu^{-0.3}$ in the higher energies. The radiation by π^0 decay (GeV-TeV γ-ray) show the same trend as the non-thermal bremsstrahlung ($\nu F(\nu) \propto \nu^{-0.3}$) above the low-energy cutoff around $0.1\,\mathrm{GeV}$. The colored dots show the observational results of the different experiments: radio data, X-ray from Suzaku X-ray satellite, GeV γ-ray from Large Area Telescope (LAT) on Fermi γ-ray space telescope, TeV γ-ray from Very Energetic Radiation Imaging Telescope Array System (VERITAS).

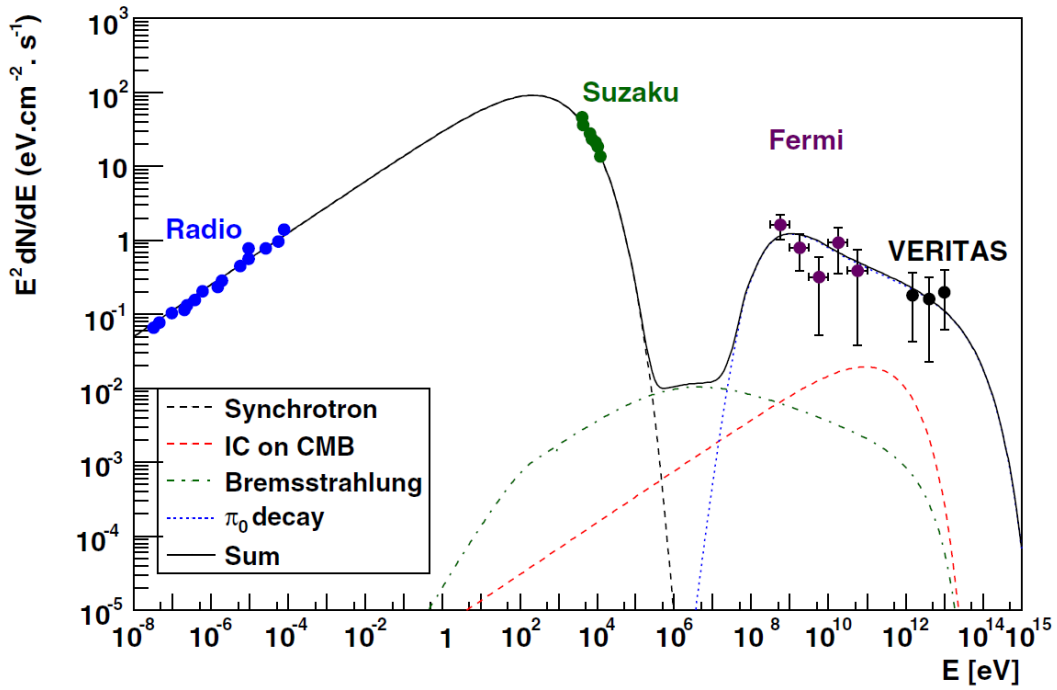

Figure 1.3: The broadband spectra of the Tycho's SNR in the hadronic scenario (from Giordano et al. [2012]). Each line shows the different radiation models: synchrotron radiation, IC scattering of CMB, non-thermal Bremsstrahlung, π_0 decay and the sum of them. Each color dot shows the observational results obtained by the different experiment: radio data, X-ray from Suzaku, GeV γ-ray from Fermi-LAT, and TeV γ-ray from VERITAS. The horizontal axis means the energies of photons, and the vertical axis means the photon energy flux.

1.1.2 Observations of SNR shocks

The radio observations of SNRs have a long history from 1940's, radio spectra have been obtained from 274 SNRs out of 294 known in our galaxy [Green, 2014]. These observations revealed that the radio emissions, which was the synchrotron radiations from GeV electrons, had power-law spectra. Although there are the variations among SNRs, their spectral indices α were approximately 0.5 [Green, 2014; Dubner and Giacani, 2015]. From the relation between α and the spectral indices of CR electrons s, such values of α imply $s \sim 2$, which have a good agreement with the index of GCRs. This fact was one of the evidences that SNR shocks were the origins of GCRs. However, steeper CR electron spectra ($\alpha \gtrsim 0.5$) are also reported typically in young SNRs, these spectra can be qualitatively explained by the nonlinear shock accelerations due to the efficient CR generations [Reynolds and Ellison, 1992].

The X-ray observations began in 1970's by means of the astronomy satellites. In 1995,

Koyama et al. [1995] discovered synchrotron X-rays from SN 1006 by ASCA X-ray astronomy satellite. The observed spectra continued to $\sim 20\,\mathrm{keV}$. From Equation (1.2), the energies of electrons responsible for the X-ray emission were up to $\sim 200\,\mathrm{TeV}$, when the strength of the magnetic fields was assumed to be $\sim \mu\mathrm{G}$. This was the first direct evidence suggesting that non-thermal electrons are accelerated to around the knee energy. After then, X-ray observations revealed X-ray synchrotron radiations in various SNRs, such as RX J1713.7-3946 [Koyama et al., 1997; Slane et al., 1999; Allen et al., 1997], RCW 86 [Borkowski et al., 2001], Cas A [Allen et al., 1997], G266.2-1.2 [Aschenbach, 1998; Slane et al., 2001], indicating the acceleration of GCR electrons. In addition to the X-ray spectra, the thin filament structures around the shells of some SNRs were discovered by the observations in the X-ray band. Typical examples is shown in the northeast and southwest rims of SN1006 in Figure 1.2. Bamba et al. [2003] investigated those filaments, and the width of the filaments were about $0.1\,\mathrm{pc}$, which was the 1% of the diameter of the remnant. If the width of the filament is equal to the length of the mean free path of the parent ($\sim 100\,\mathrm{TeV}$) CR electron, the cooling time by the synchrotron radiations becomes so short, $10-100\,\mathrm{yr}$. This requires the magnetic fields of $10-100\,\mu\mathrm{G}$, which is more than 10 times larger than that of ISM [Bamba et al., 2004; Yamazaki et al., 2004]. In the other SNRs, thin X-ray filaments also inferred the amplified magnetic fields to $10-100\,\mu\mathrm{G}$ [Vink and Laming, 2003; Bamba et al., 2005]. Such amplification was deduced from the rapid time variation of synchrotron X-ray. Figure 1.4 is the X-ray images of the western shell of SNR RX J1713.7-3946 by Chandra [Uchiyama et al., 2007]. In the overall image of Figure 1.4a, the bluish white hotspots mean the strong synchrotron X-ray emissions. The enlarged images 1.4b and 1.4c for the boxes (b) and (c) in 1.4a show the more compact hotspots, which change brightness in less than a few years. If such a rapid variability reflects the time scale of the energy loss of CR electrons by the synchrotron cooling, the strength of the magnetic fields can be estimated as $B \sim 1\,\mathrm{mG}$ from the relation

$$\tau_{cool} \sim 2.86 \left(\frac{B}{\mathrm{mG}}\right)^{-1.5} \left(\frac{E_{p,sync}}{\mathrm{keV}}\right)^{-0.5} \mathrm{yr}, \tag{1.8}$$

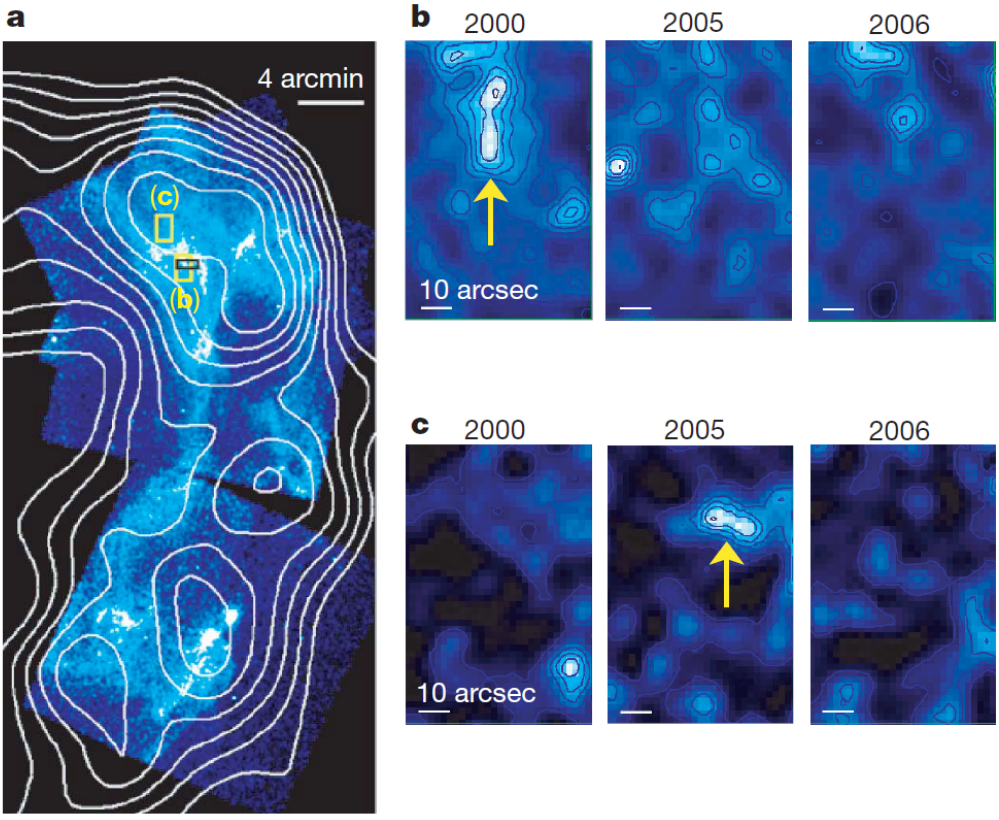

Figure 1.4: Chandra X-ray images of the western shell of SNR RX J1713.7-3946 (from Uchiyama et al. [2007]). **a**: Chandra X-ray ($1-2.5\,\mathrm{keV}$) color image overlaid with TeV γ-ray contours from HESS. **b**: a time sequence of X-ray observations in the same energy band as **a** ($1-2.5\,\mathrm{keV}$) in July 200, July 2005 and May 2006 for a small box labeled (b) in **a**. **c**: a time sequence in hard X-ray band ($3.5-6\,\mathrm{keV}$) for a box (c) in **a**, in the same time as **b**.

which is derived from Equations (1.2) and (1.4). Similar year-scale variability was also observed in SNR Cassiopeia A, and inferred the strong magnetic fields of $1\,\mathrm{mG}$ [Uchiyama and Aharonian, 2008].

The γ-ray observations started in 1960's with the satellites, and in late 1980's, observations with the ground-based Cherenkov telescopes began. These telescopes detected the Cherenkov radiations emitted by the numerous secondary CRs, which were generated by the interaction between the molecules of the upper atmosphere and the incident γ-ray photons. Though the acceleration of the CR electrons in the SNR shocks is confirmed by the synchrotron radiations, an evidence of the acceleration of the CR protons, which are made up of the majority of CRs has been a matter of debate. That is because whether the origin of γ-ray is in hadoronic process or in leptonic process is difficult to determine only from the spectrum. CANGAROO, a

ground-based atmospheric Cherenkov telescope, first detected TeV γ-rays from RX J1713.7-3946 [Enomoto et al., 2002] and High Energy Stereoscopic System (HESS) observed this SNR with high spatial resolutions [Aharonian et al., 2004, 2006; Aharonian et al., 2007]. Whereas some authors suggested the TeV γ-ray emissions are the hadronic origin [Morlino et al., 2009; Berezhko and Völk, 2008; Yamazaki et al., 2009], others suggested that these are due to the leptonic process [Zirakashvili and Aharonian, 2010; Ellison et al., 2010]. As explained above, if non-thermal protons (or electrons) are in the power law distributions: $N(E) \propto E^{-s}$, the theoretically predicted spectra of photons: $F(\nu) \propto \nu^{1-s}$ in the bremsstrahlung and π^0 decay, $F(\nu) \propto \nu^{(s-3)/2}$ in IC. The former is softer than the latter (when $s = 2$ that is the standard value of GCRs), and should be more dominant in lower energies. In addition, for the π^0 decay scenario, a certain density of "target" thermal protons with which non-thermal protons interact around the shocks is required. However, thermal X-ray that these thermal protons should radiate is very faint [Lazendic et al., 2004]. Furthermore, GeV γ-ray observations of RX J1713.7-3946 by the Fermi-LAT show the smooth connection with the TeV γ-ray spectra of HESS [Abdo et al., 2011]. The resulting broadband photon spectra (GeV-TeV) indicate a flatter index than the π^0 decay predicts, and can not sustain the dominance of π^0 decay scenario in the lower energies. Therefore, recently, the leptonic scenario is preferred to explain the TeV emission of RX J1713.7-3946.

RX J1713.7-3946 is a young and most energetic TeV γ-ray SNRs. As for other young ($\lesssim 5\,\mathrm{kyr}$) SNRs with bright γ-ray emission such as RX J0852.0 $-$ 4622, RCW 86, SN 1006 and HESS J1731 $-$ 347, their emissions are also seemed to be leptonic-dominated [Acero et al., 2015]. A direct evidence of the hadronic γ-ray emission was found in the two middle-age SNRs, W44 ($\sim 20\,\mathrm{kyr}$) and IC443 ($\sim 10-20\,\mathrm{kyr}$). The multi-wavelength observations of W44 from the radio, optical, X-ray and γ-ray ($50\,\mathrm{MeV} - 10\,\mathrm{GeV}$ by Fermi [Abdo et al., 2010b] and AGILE [Giuliani et al., 2011] satellites) gave the broadband spectra of the photons. These spectra well fitted to the low-energy cut off, which was the typical feature of the radiations by π_0 decay. Similarly, the spectrum of IC443 had good correspondence only to the hadronic model [Tavani et al., 2010; Abdo et al., 2010c]. These results were the first direct evidence indicating the acceleration of CR protons. This was due to the existence of dense molecular clouds (MCs) nearby the SNRs,

which provided rich thermal protons as targets of the CRs protons. Notice that the estimated maximum energy of the protons was limited around a few hundred GeV, which was much smaller that the knee energy, and the estimated power-law indices in the energy region were steeper than that of GCRs (-2), indicating the less efficient acceleration. It is also noted that such hadronic γ-ray emissions do not necessarily mean the CR protons are "newly" accelerated by the SNR shocks. Uchiyama et al. [2010] suggested that these γ-ray emissions could be explained by the interaction between the "re-accelerated" pre-existing CRs in ISM by the passage of the shocks and the thermal protons in the MCs. Although there are not so conclusive evidences as those in W44 and IC443, the γ-ray from two young SNRs, Tycho's SNR and Cassiopeia A, imply the hadronic processes [Giordano et al., 2012; Morlino and Caprioli, 2012; Blasi, 2014; Abdo et al., 2010a]. For example, the hadronic model where γ-ray photons are mainly emitted by the π_0 decay, is consistent with the γ-ray data from Fermi-LAT and VERITAS in Tycho's SNR, as shown in Figure 1.3. If that is the case, the CR protons are accelerated up to $\sim 500\,\mathrm{TeV}$ at a maximum in Tycho's SNR, which is still smaller than the knee energy ($\sim 3 \times 10^{15}\,\mathrm{eV}$), and $10-15\%$ of the kinetic energy of the shock is converted into CR protons [Morlino and Caprioli, 2012; Slane et al., 2014]. Besides, the predicted CR proton spectrum becomes steeper than the standard value ($N(E) \propto E^{-2}$). Caprioli [2011] summarized the spectral indices of the GeV and TeV γ-ray photons in the other γ-ray-bright SNRs. If the γ-rays are assumed to be the hadronic (π_0 decay) origin, most SNRs also showed the steeper spectra.

The observations of SNRs also revealed some typical structure in the upstream region. Figure 1.5 shows the X-ray photons counts across the rim of RCW 86 [Bamba et al., 2005]. We can see the decay of photon counts towards the upstream (left) from the peak. These photon counts are due to the synchrotron emission of the non-thermal electrons. If these photon counts simply reflect the number density of emitting electrons, this profile indirectly shows the decaying profiles of the CR electrons density. Such decay profiles in photon counts have been reported in other SNRs [Bamba et al., 2003, 2005]. These decay structures from the shock towards the upstream are called "precursor", and these structures are reflects on the acceleration mechanism of CRs.

Precursor is not typical structure only for SNR shocks. In heliosphere, we can obtained the

direct data of the densities of the accelerated particles by the in-situ observations of interplanetary shocks (IPSs) [Shimada et al., 1999; Terasawa et al., 2005, 2006]. Figure 1.6 shows the profiles of the density of the protons measured by GEOTAIL spacecraft in the passage of an IPS formed by coronal mass ejection (CME) [Shimada et al., 1999]. The precursor was seen for energetic protons in every energy band. In addition, the width of the precursor that depends on the diffusion coefficient became larger for the higher energy protons, which is similar to the Bohm-type diffusion, where the diffusion coefficient is proportional to the particle momenta.

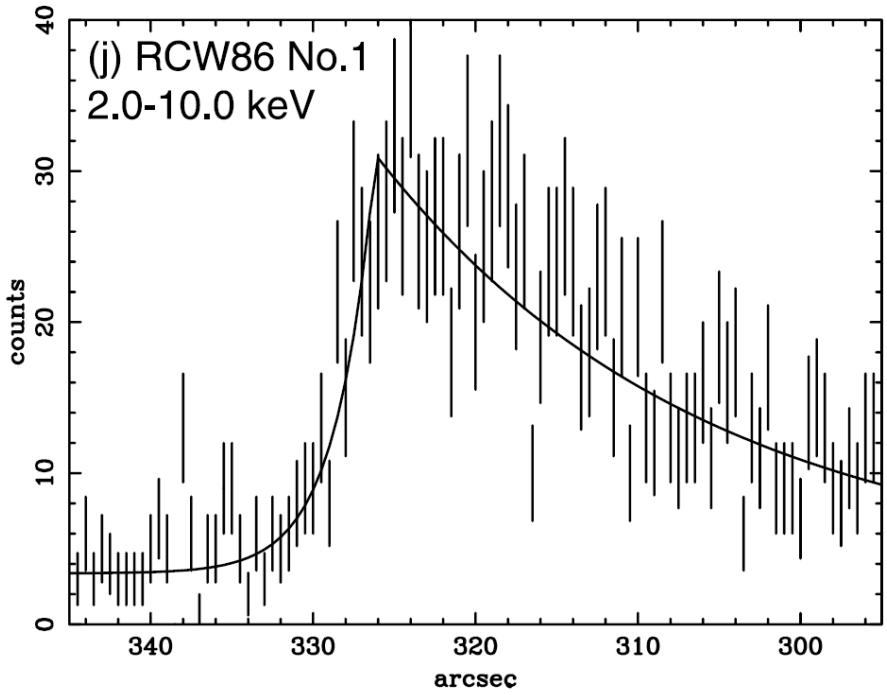

Figure 1.5: Photon counts in the hard X-ray band ($2.0 - 10.0\,\mathrm{keV}$) across the shell of RCW 86 from upstream (left) to downstream (right) (from Bamba et al. [2005]). The vertical dashes mean the photon counts and solid lines shows the best-fit of the exponential-type function to the photon counts.

1.2 Theory of Diffusive Shock Acceleration (DSA)

Observations of SNR shocks have revealed the evidences of GCR acceleration, as described in the previous section. In this section, we briefly review the acceleration mechanism of particles. Classical acceleration theory of non-thermal particles in astrophysics is known as "Fermi

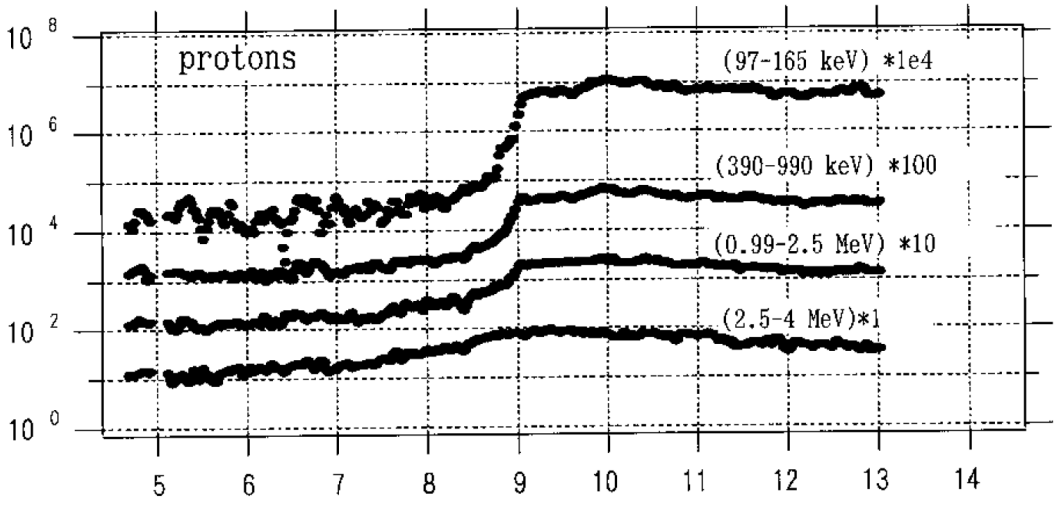

Figure 1.6: Counts of protons for the different four energy channels ($97-165\,\mathrm{keV}$, $390-990\,\mathrm{keV}$, $0.99-2.5\,\mathrm{MeV}$ and $2.5-4\,\mathrm{MeV}$), of the interplanetary shock on 21 February 1994 (from Shimada et al. [1999]). Left side is upstream and right is downstream.

acceleration", which was proposed by Fermi in 1949 [Fermi, 1949]. In his theory, particles reflect off interstellar clouds, which have stronger magnetic field than interstellar magnetic field through magnetic mirroring. Particles gain energy in "head-on collisions" with the clouds, and lose energy in "trailing collisions". When the probabilities of these collisions are considered, the probabilities of head-on collisions is slightly higher than the other. Therefore, after the many collisions, energy gains slightly exceeds energy losses, then particles are accelerated to non-thermal energy. This theory suggested the rate of the energy gain of a particle dE/dt:

$$\frac{dE}{dt} = \frac{4}{3}\left(\frac{V}{v}\right)^2 \frac{1}{t_{coll}} E, \tag{1.9}$$

where V is the velocity of interstellar clouds, v and E are the velocities and energies of each particles, respectively, and t_{coll} is the average collision time. This formula gives

$$E = E(t=0)\exp\left(\frac{t}{t_{acc}}\right), \tag{1.10}$$

where t_{acc} is the acceleration time defined as

$$t_{acc} = \frac{3}{4}\left(\frac{v}{V}\right)^2 t_{coll}. \tag{1.11}$$

Typically, $V \sim 10\,\mathrm{km/s}$ and $t_{coll} \sim 10^9\,\mathrm{s}$ in the ISM and v is almost equal to the speed of light c for the CR particles. Then the acceleration time $t_{acc} \sim 10^{18}\,\mathrm{s}$, which is too longer than the age of our universe ($\sim 10^{17}$). Today, Fermi's acceleration theory is called "second order Fermi acceleration" because the rate of the energy increase is proportional to $(V/c)^2$.

In late 1970's, a more effective statistical particle acceleration theory was proposed [Bell, 1978; Blandford and Ostriker, 1978; Axford et al., 1977], where the method of original Fermi acceleration was applied to the shock waves. This theory was called "Diffusive Shock Acceleration (DSA)". The mechanism of DSA is described as follows. Figure 1.7 shows a schematic view

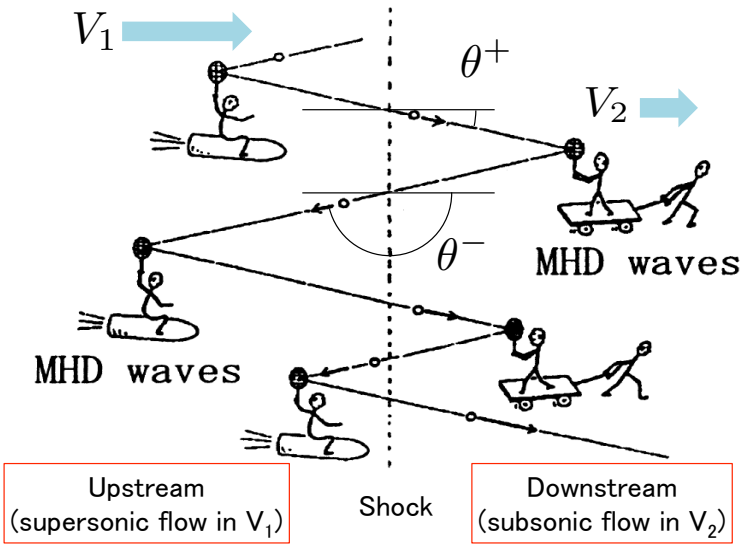

Figure 1.7: A cartoon of DSA (based on Scholer). Left side of the shock surface is upstream region and right is downstream.

of the DSA. V_1 and V_2 are the upstream and downstream flow velocities in the shock rest frame ($V_1 > V_2$). Around the shock, the magnetic irregularities such as Alfvén waves are excited by some plasma instabilities between the CRs and the background plasma. When CRs "collide" with these waves, they are elastically reflected and turn their directions of motion. This scattering process is known as "pitch angle scattering". The velocities of the reflected particles decrease

(increase) when the particles collide with the waves that moving the same (opposite) direction because of the conservation of momentum. In the upstream region, particles gain energies by "head-on collisions" with the waves moving in V_1 (co-moving with the background plasma flow) and lose energies by "trailing collisions" with the waves moving in V_2 in the downstream. At the one reflection, the direction of particle's motion change randomly and a certain ratio of particles can be reflected back to the shock surface.

Here is the derivation of the energy gain and the spectrum of accelerated particles in DSA. Through one cycle (starts from the upstream region and returns to the upstream by the scattering in the downstream), the energy of a particle changes from E to E'. The ratio of E' and E is described following,

$$\frac{E'}{E} = \frac{1-\frac{V_1 v}{c^2}\cos\theta^-}{1-\frac{V_2 v}{c^2}\cos\theta^-}\frac{1-\frac{V_2 v}{c^2}\cos\theta^+}{1-\frac{V_1 v}{c^2}\cos\theta^+} \tag{1.12}$$

where the θ^+ and θ^- is the angles between the particle velocity and the shock normal; a superscript +(-) means the particle goes into (out from) the downstream region, which are shown in Figure 1.7. If the particles are assumed to be isotropic, the expectation of Equation (1.12) become,

$$\left\langle \frac{E'}{E} \right\rangle = 1 + \frac{4}{3}\frac{(V_1 - V_2)v}{c^2} \sim 1 + \frac{4}{3}\frac{(V_1 - V_2)}{c}. \tag{1.13}$$

Note that $V_1, V_2 << c(\sim v)$ in the above final transformation. Only a small fraction of particles can experiences above stochastic reflection many times and accelerated to the relativistic energy. The energy gain in one cycle in DSA is proportional to $\sim (V/c)$, where V is the velocity of the shock wave, DSA is also called "first order Fermi acceleration" compered with the original Fermi's mechanism.

After the n cycles, the energy of the particle becomes,

$$E_n = E(t=0)\left(1 + \frac{4}{3}\frac{(V_1 - V_2)}{c}\right)^n \sim E(t=0)\exp\left(\frac{4n}{3}\frac{(V_1 - V_2)}{c}\right). \tag{1.14}$$

In the acceleration, some particles which are not reflected to the upstream region escape from the shock region. A possibility of such a escape per one cycle P_{esc} is evaluated by the ratio of the flux of particles which flow away from the shock in the downstream, to the inflow flux into the shock from the upstream:

$$P_{esc} = \frac{N_0 V_2}{\frac{N_0}{2}\frac{v}{2}} \sim \frac{4V_2}{c}. \tag{1.15}$$

N_0 is the number of particles at the upstream region. The inflow flux is the product of the number of particles heading to shock ($N_0/2$) and the mean velocity of them ($v/2$). Considering the escape, the possibility that particles can exist around the shock after n cycles is,

$$P_n = (1 - P_{esc})^n = \left(1 - \frac{4V_2}{c}\right)^n \sim \exp\left(-n\frac{4V_2}{c}\right). \tag{1.16}$$

Substitution of Equation (1.14) into Equation (1.16) gives

$$P_n \simeq \left(\frac{E_n}{E(t=0)}\right)^{-3V_2/(V_1-V_2)}. \tag{1.17}$$

P_n can be expressed by the $N(E)$ that is the number of particles whose energies are between E and $E + dE$:

$$P_n = \int_{E_n}^{\infty} N(E)dE. \tag{1.18}$$

From Equations (1.17) and (1.18), $N(E)$ is solved as follows,

$$N(E) \propto E^{-s}, \tag{1.19}$$

where s is expressed by the compression ratio of the shock $r = \frac{V_1}{V_2}$:

$$s = \frac{3V_2}{V_1 - V_2} + 1 = \frac{V_1/V_2 + 2}{V_1/V_2 - 1} = \frac{r+2}{r-1}. \tag{1.20}$$

This means that the index s of the power-law energy spectrum in DSA depends only on the compression ratio of shocks. The compression ratio r approaches to 4 at strong shocks such as SNRs, then the asymptotic spectrum index is 2. This value has a good correspondence with the observational value of GCRs (2.7), when the softening effects due to the decay in propagating the interstellar medium are taken into account.

Above discussion about DSA is based on the particles' motions, which was proposed by Bell [1978]. On the other hand, DSA theory can be understood by the transport equations of CRs' distribution function $F(\boldsymbol{x},\boldsymbol{p},t)$. These equations have been proposed by many authors in the long history [Parker, 1965; Gleeson and Axford, 1967; Jokipii, 1971; Skilling, 1975a]. Among them, most simplest formula is:

$$\frac{\partial f}{\partial t} + \boldsymbol{u}\cdot\nabla f - \nabla(\boldsymbol{\kappa}\nabla f) = \frac{1}{3}(\nabla\cdot\boldsymbol{u})p\frac{\partial f}{\partial p}, \tag{1.21}$$

which is so-called "diffusion-convection equation" of CRs. $\boldsymbol{u}$ is the velocity of the background plasma flow. CRs are assumed to be scattered efficiently by the scattering center fixed in the flow, and to be almost isotropic. $f = f(\boldsymbol{x},p,t)$ is an isotropic part of F. The second terms of the left and the one in the right hand side mean the convection and the adiabatic heating with the change of volume, respectively. The terms excluding the third diffusion term in the left hand side that means spatially diffusion are essentially derived from the conservation of the phase space density. The diffusion term is due to the random particle scattering by the perturbed magnetic fields. For the simplicity, a most optimistic diffusion coefficient is often used (where discussed in Drury [1983]), i.e. the Bohm diffusion coefficient $\kappa_B = \frac{1}{3}r_g v$, where r_g is the gyro radius of a particle. The Bohm diffusion is the fastest diffusion across the magnetic fields, then it gives the maximum values of the diffusion coefficient.

DSA can be described by the diffusion-convection equation as follows. When the one dimensional parallel shocks (located at $x = 0$), where the background magnetic fields are parallel to

the normal of the shock surface, are considered, Equation (1.21) is simplified to

$$\frac{\partial f(x,p)}{\partial t} + u(x)\frac{\partial f(x,p)}{\partial x} - \frac{\partial}{\partial x}\left(\kappa(x,p)\frac{\partial f(x,p)}{\partial x}\right) = \frac{1}{3}\frac{\partial u(x)}{\partial x}p\frac{\partial f(x,p)}{\partial p}. \tag{1.22}$$

In the time-asymptotic state, the time-derivative term is neglected as follows,

$$u(x)\frac{\partial f(x,p)}{\partial x} - \frac{\partial}{\partial x}\left(\kappa(x,p)\frac{\partial f(x,p)}{\partial x}\right) = \frac{1}{3}\frac{\partial u(x)}{\partial x}p\frac{\partial f(x,p)}{\partial p}. \tag{1.23}$$

For the simplicity, the flow velocity of the background plasma $u(x)$ and the diffusion coefficient $\kappa(x,p)$ are assumed to be spatially constant in the upstream and downstream, i.e.

$$u(x) = \begin{cases} V_1 & (x<0), \quad (1.24) \\ V_2 & (x>0), \quad (1.25) \end{cases}$$

where $V_1 > V_2 (> 0)$, and

$$\kappa(x,p) = \begin{cases} \kappa_1'(p) & (x<0), \quad (1.26) \\ \kappa_2'(p) & (x>0). \quad (1.27) \end{cases}$$

Off the shock, the steady-states obey the following simple diffusion equation because the compression term of Equation (1.23) is neglected,

$$V_{1,2}\frac{\partial f(x,p)}{\partial x} - \frac{\partial}{\partial x}\left(\kappa_{1,2}'(p)\frac{\partial f(x,p)}{\partial x}\right) = 0. \tag{1.28}$$

From this equation, we can obtained following asymptotic profiles of the upstream and downstream, assuming the finite (nonzero) values at the far upstream and downstream:

$$f(x,p) = \begin{cases} f_1(p)\exp\left(\dfrac{V_1}{\kappa_1'(p)}x\right) + f_0(p) & (x<0) \quad (1.29) \\ f_2(p) & (x>0), \quad (1.30) \end{cases}$$

where $f_0(p)$, $f_1(p)$ and $f_2(p)$ are the values at the far upstream, the shock and the far upstream,

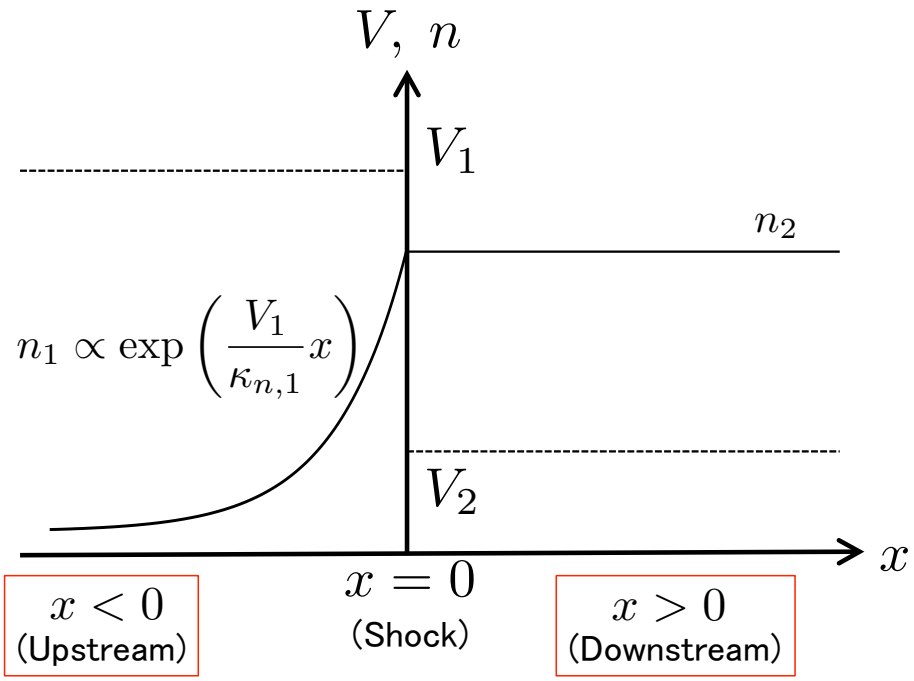

Figure 1.8: Typical time-asymptotic structures of the number density of CRs n (solid line) and the velocity of the background plasma V (dashed line) in DSA. Subscripts 1 and 2 means the values at the upstream ($x < 0$) and the downstream ($x > 0$).

respectively. The profiles of the number density n of CRs are also written by

$$\begin{cases} n(x) \propto \exp\left(\dfrac{V_1}{\kappa_{n,1}} x\right) & (x < 0) \qquad (1.31) \\ n(x) \sim n_2 & (x > 0). \qquad (1.32) \end{cases}$$

$\kappa_{n,1}$ and n_2 are the average diffusion coefficient at the upstream and the number density at the downstream. The profiles of above solutions are illustrated in Figure 1.8 with the solid line. The exponentially decaying upstream profiles should correspond to the precursor, which is observed in SNR shocks or IP shocks.

At the shock ($x = 0$), CRs are assumed to be distributed continuously across the shock because of the large mean free path of CR compared with the width of the shock, i.e.

$$[f(x,p)]_{0-}^{0+} = 0. \qquad (1.33)$$

Hence, the integral of Equation (1.22) from $x = 0-$ to $x = 0+$ becomes

$$-\left[\kappa\frac{\partial f}{\partial x}\right]_{0-}^{0+} = \frac{1}{3}p\frac{\partial f_1}{\partial p}[u]_{0-}^{0+}, \tag{1.34}$$

then Equations (1.29) and (1.32) give

$$p\frac{\partial f_1}{\partial p} = \frac{3}{V_1 - V_2}\left[\kappa\frac{\partial f}{\partial x}\right]_{0-}^{0+} = -\frac{3}{V_1 - V_2}\kappa_1'\left.\frac{\partial f}{\partial x}\right|_{x=0+} = -\frac{3V_1}{V_1 - V_2}f_1(p) = -\frac{3r}{r-1}, \tag{1.35}$$

where $r = V_1/V_2$ is the compression ratio of the shock. The spectrum at the shock is given as follows,

$$f_1(p) \propto p^{-3r/(r-1)}. \tag{1.36}$$

Notice that the number of particles per unit energy $N(E)$ (equivalently, the number of particles per unit relativistic momentum $N(p)$) is connected with the distribution function $f(p)$ through the relation $N(E)dE = N(p)dp = 4\pi p^2 f(p)dp$. $N(E)$ follows,

$$N(E) \propto E^{-3r/(r-1)+2} \propto E^{-(r+2)/(r-1)}, \tag{1.37}$$

where the spectral index corresponds to Equation (1.20). Again, as for the strong shocks ($r \sim 4$), the asymptotic spectra become

$$\begin{cases} N(E) \propto E^{-2}, & (1.38) \\ f(p) \propto p^{-4}. & (1.39) \end{cases}$$

From the above two different approaches, i.e. approaches by the CR particles' motions and the diffusion-convection equation of the CRs, the equivalent results show the good correspondence between theoretical predictions of DSA and observations of GCRs. That is why DSA is widely accepted as a standard acceleration theory of CRs.

1.3 Nonlinear Diffusive Shock Acceleration (NLDSA)

Although the DSA theory basically gives good explanations about observations, there are many issues we have to work on in the acceleration theory. One of them is the acceleration efficiency of the CRs. From the energetic relation between the GCR energy and the kinetic energy of supernova explosions, the efficiency is roughly estimated as $\sim 10\%$. However, this value is not the definite one, and varies largely depending on observations.

Helder et al. [2009] observed RCW 86 and estimated downstream thermal proton temperature at about $2.3\,\mathrm{keV}$ from Hα spectrum. This temperature was about one-twentieth of the theoretical temperature calculated by RH relation, $42\,\mathrm{keV}$. Cold downstream thermal plasma means that the kinetic energy of upstream plasma is distributed to other than downstream thermal plasma, to acceleration of CRs. In this case, the ratio of the energy density of CRs to the total energy density at downstream region is about 50%. Similar observations have also been reported [Hughes et al., 2000; Decourchelle et al., 2000; Helder et al., 2010; Warren et al., 2005; Cassam-Chenaï et al., 2008]. In contrast to these observations suggesting efficient production of CRs, Fukui [2013] estimated, using observations of γ-rays and interstellar molecular clouds, that the CR proton energy is only $\sim 0.1\%$ of the total kinetic energy in young SNRs RX J1713.7-3946 and RX J0852.0-4622.

In the heliosphere, the energy densities of particles accelerated by IP shocks driven by CMEs were estimated using in-situ observations. The results indicated that the energetic particles accounted for at most $10-20\%$ of the CME kinetic energy [Mewaldt et al., 2005; Mewaldt, 2006]. Other observations of IP shocks also referred to the negligible energy of non-thermal particles [Terasawa et al., 1999; Terasawa et al., 2006].

Although the CR production efficiency in the SNRs shocks is still controversial, some fraction of the kinetic energies are actually more or less converted into CRs. The number of CRs is extremely low but each particles' energy is tremendous compared with the background plasma. Therefore, the energy density of CRs is not necessarily negligible in comparison with that of the background plasma. In order to evaluate the energy density of CRs, we consider the CR pressure p_c and the CR internal energy density E_c by the moments of the isotropic CR distribution

function defined as,

$$p_c(x) = \frac{4\pi}{3}\int_0^\infty p^3 v f(x,p) dp, \tag{1.40}$$

$$E_c(x) = 4\pi\int_0^\infty p^2 T(p) f(x,p) dp, \tag{1.41}$$

where p and v are the momenta and velocities of the CR particles. $T(p)$ is the relativistic kinetic energy of the particles with momentum p. When the contribution of p_c to the total pressure, i.e. the pressure ratio N:

$$N = \frac{p_c}{p_g + p_c}, \tag{1.42}$$

is not small, p_c can exert an additional pressure to the shock structure, which is known as "back-reaction" to the shocks. The back-reaction occurs in the nonlinear regime of the particle acceleration when the population of CRs increases. In contrast with the test-particle limit where CRs behave passively as mentioned in Section 1.2, this mechanism is called "Nonlinear DSA (NLDSA)" that was firstly proposed in the 1980's. [Drury and Völk, 1981; Drury, 1983; Axford et al., 1982]. Shocks affected by the back-reaction of CRs are typically called "cosmic ray modified shocks" or "cosmic ray mediated shocks" (CRMSs).

1.3.1 Theory of NLDSA

The back-reaction was first studied by Drury and Völk [1981] in the "two-fluid" model, where both of the background plasma and CRs are treated as fluids and the back-reaction is explained by the force by the CR pressure gradient. They showed the following hydrodynamical equations modified the additional CR pressure:

$$\frac{\partial \rho}{\partial t} + \frac{\partial}{\partial x}(\rho u) = 0, \tag{1.43}$$

$$\frac{\partial}{\partial t}(\rho u) + \frac{\partial}{\partial x}(\rho u^2 + p_g + p_c) = 0, \tag{1.44}$$

$$\frac{\partial}{\partial t}\left(\frac{1}{2}\rho u^2 + \frac{p_g}{\gamma_g - 1} + \frac{p_c}{\gamma_c - 1}\right) + \frac{\partial}{\partial x}\left[\left(\frac{1}{2}\rho u^2 + \frac{\gamma_g}{\gamma_g - 1}p_g + \frac{\gamma_c}{\gamma_c - 1}p_c\right)u - \frac{\bar{\kappa}(x)}{\gamma_c - 1}\frac{\partial p_c(x)}{\partial x}\right] = 0. \tag{1.45}$$

ρ, u, p_g and γ_g are the density, velocity of the flow, pressure and the specific heat ratio of the background plasma, respectively. γ_c is the specific heat ratio of CRs defined as $\gamma_c = p_c/E_c + 1$. Notice that the mass density of CRs ρ_c is neglected compared to ρ in above equations. The density of CRs ρ_c is

$$\rho_c \sim 4\pi \int_0^\infty p^2 \left(\frac{T(p)}{c^2}\right) f(x,p) dp \sim \frac{E_c}{c^2}. \tag{1.46}$$

If E_c is comparable with the energy density of the background plasma $E_g(p_g/(\gamma_g - 1))$:

$$E_c \sim E_g \sim \frac{p_g}{\gamma_g - 1} \sim \frac{1}{\gamma_g - 1}\frac{k_B T}{m}\rho, \tag{1.47}$$

where k_B, T and m are Boltzmann constant, temperature of the background plasma and the mass of the particles. $T \sim 100 - 10000\,\mathrm{K}$, typically for upstream plasma (i.e. ambient ISM plasma) and the proton mass is assumed for m, then $\frac{k_B T}{m} \sim (1-100) \times 10^{10}\,(\mathrm{cm/s})^2$. From Equations (1.46) and (1.47), ρ_c is

$$\rho_c \sim \frac{(1-100) \times 10^{10}\,(\mathrm{cm/s})^2}{c^2}\rho \sim 10^{-10}\rho, \tag{1.48}$$

which is much smaller than the density of the background plasma ρ.

The hydrodynamical energy equation for E_c is given by the energy moment of the diffusion-convection equation (1.22):

$$\frac{\partial E_C}{\partial t} + u\frac{\partial E_c}{\partial x} - \frac{\partial}{\partial x}\left(\quad \bar{\kappa}(x)\frac{\partial E_c}{\partial x}\right) = 0. \tag{1.49}$$

The diffusion coefficient $\bar{\kappa}(x)$ are defined following:

$$\bar{\kappa}(x) = \frac{\int_0^\infty \kappa(x,p) p^2 T(p)(\partial f/\partial x) dp}{\int_0^\infty p^2 T(p)(\partial f/\partial x) dp}. \tag{1.50}$$

From basic hydrodynamical equations, the "modified" RH conditions in the two-fluid model are

obtained:

$$\rho(x)u(x) = A(=\text{constant}), \tag{1.51}$$

$$Au(x) + p_g(x) + p_c(x) = B(=\text{constant}), \tag{1.52}$$

$$\frac{1}{2}Au(x)^2 + \frac{\gamma_g p_g(x)}{\gamma_g - 1}u(x) + \frac{\gamma_c p_c(x)}{\gamma_c - 1}u(x) - \frac{\bar{\kappa}(x)}{\gamma_c - 1}\frac{\partial p_c}{\partial x} = C(=\text{constant}). \tag{1.53}$$

In the precursor, the background plasma is compressed adiabatically:

$$p_g(x)u(x)^{\gamma_g} = D(=\text{constant}). \tag{1.54}$$

Equations (1.51), (1.52), (1.53) and (1.54) determine the profiles of $\rho(x)$, $u(x)$, $p_g(x)$ and $p_c(x)$ in the precursor. Figures 1.9 show the typical spatial profiles of the flow velocity $u(x)$ (upper panel) and the CR pressure p_c (lower panel). In the precursor, p_c decreases exponentially towards the upstream, this CR pressure gradient forces the flow of the background plasma to decelerate. As the result, the flow velocity of the back ground plasma u declines smoothly in the precursor and connects to the discontinuity. The discontinuity that is left at the original location of the shocks is called "subshock". Thus the structures of shocks are apparently modified to those including precursor and subshock by the back-reaction of CRs.

Across the subshock, the continuous condition for the distribution function of CRs (1.33) gives the similar continuous condition for the CR pressure:

$$[p_c] = 0, \tag{1.55}$$

which is illustrated in the lower profile of Figures 1.9. Angled brackets mean the difference across the subshock ($[X] \equiv X_{downstream} - X_{upstream}$). By the integral of Equation (1.49) (without a time-derivative term) across the subshock, it follows,

$$\int \frac{\partial}{\partial x}(uE_c) + \int p_c \frac{\partial u}{\partial x} - \int \frac{\partial}{\partial x}\left(\bar{\kappa}(x)\frac{\partial E_c}{\partial x} \right) = 0, \tag{1.56}$$

$$\Rightarrow [uE_c] + [p_c u] - \int u\frac{\partial p_c}{\partial x} - [\bar{\kappa}(x)\frac{\partial E_c}{\partial x}] = 0, \tag{1.57}$$

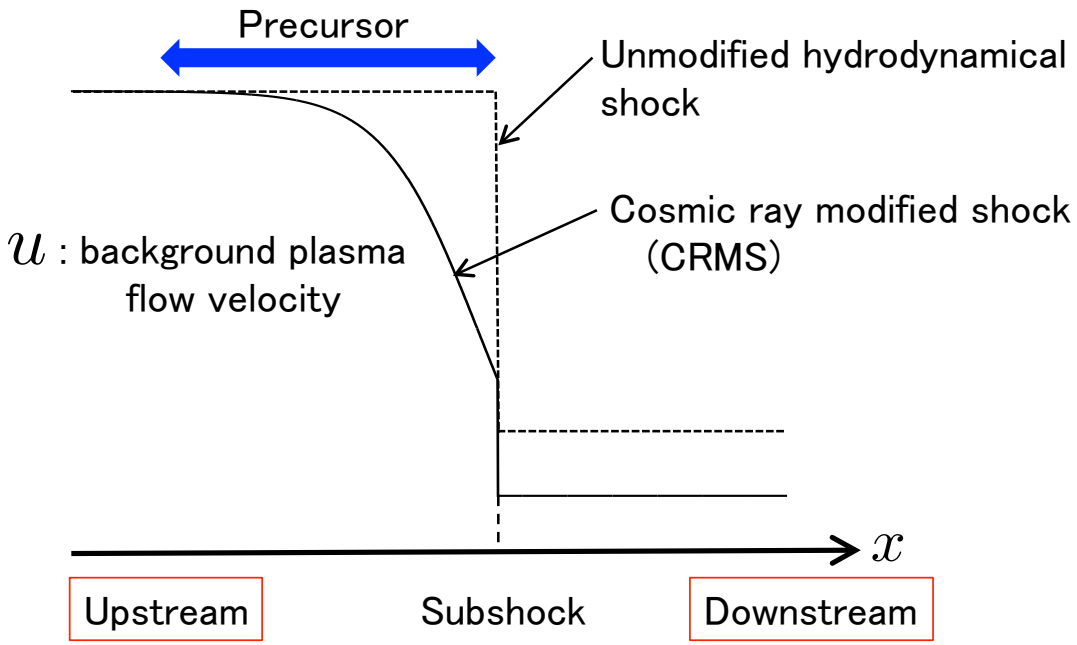

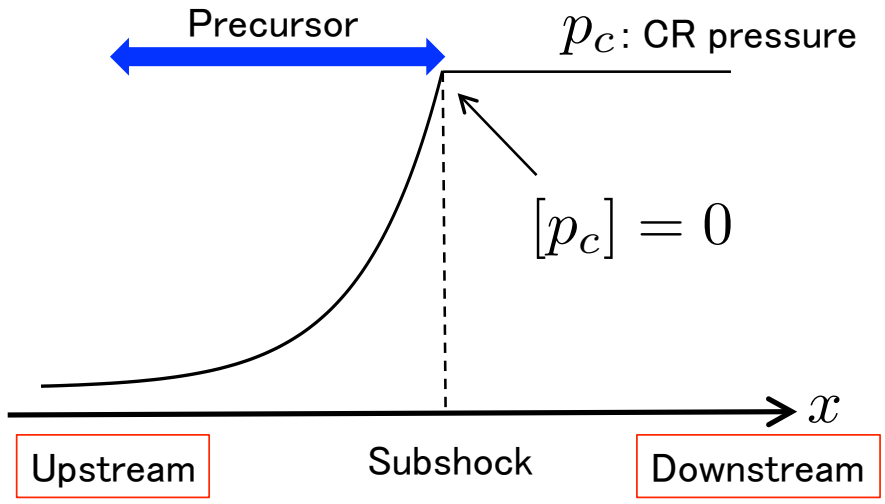

Figure 1.9: Typical structure under the modification by CRs. The upper profiles show the flow velocities of the background plasma in the cosmic ray modified shock (solid line) and the unmodified hydrodynamical shock (dashed line). The lower shows the CR pressure.

$$\Rightarrow [u\frac{\gamma_c p_c}{\gamma_c - 1} - \frac{\bar{\kappa}}{\gamma_c - 1}\frac{\partial p_c}{\partial x}] = 0. \tag{1.58}$$

In the transformation from Equation (1.57) to (1.58), we use the continuous condition for p_c (Equation (1.55)). By using Equation (1.55) and (1.58), we can derive the following jump condition at the subshock:

$$[\rho u] = 0, \tag{1.59}$$

$$[Au + p_g] = 0, \tag{1.60}$$

$$[p_c] = 0, \tag{1.55}$$

$$[\frac{1}{2}Au^2 + \frac{\gamma_g p_g}{\gamma_g - 1}u] = 0, \tag{1.61}$$

$$[u\frac{\gamma_c p_c}{\gamma_c - 1} - \frac{\bar{\kappa}}{\gamma_c - 1}\frac{\partial p_c}{\partial x}] = 0. \tag{1.57}$$

The above jump conditions mean the subshock can be seen as a one-fluid hydrodynamical shock. Drury and Völk [1981] first obtained the analytical steady-state solutions from the above modified RH conditions with spatially constant $\bar{\kappa}$.

Two-fluid model is a good approximation of CRMS because the nonlinear feedback of CRs can be treated easily in the global temporal and spatial scales. However, in the fluid approximation, we can not understand the momentum dependent behaviors of CRs. A more general approximation of CRs by the diffusion-convection equation was coupled by the hydrodynamical equations by some authors [Malkov, 1997a, b; Blasi, 2002]. Their model was called "CR-kinetic" model, where CRs are distributed not only in the spatial spaces but also in the momentum spaces. CR-kinetic model revealed the effect of the CRs' momentum dependent behaviors on the CR spectrum in NLDSA. In NLDSA, the additional (adiabatic) compression precedent to the subshock increases the total compression ratio from the typical value 4 in the test-particle limit. This increase makes the energy spectrum harder since the index s is determined by the shock compression ratio as described in Section 1.2. Additionally, there are the differences in the compression ratio that each CR particle "feels", due to the broad structure of CRMSs. High-energy CRs that have large mean free paths swim from the downstream of the subshock to

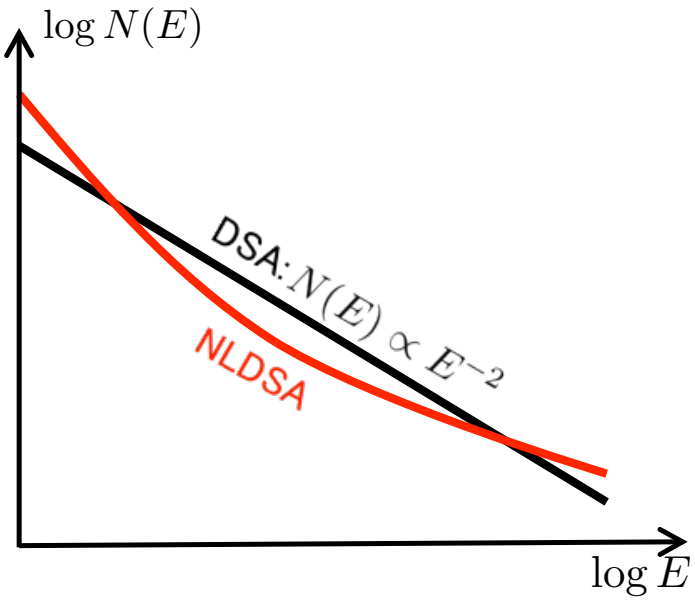

Figure 1.10: Typical energy spectra of CRs in DSA and NLDSA. The black line is the power-law spectrum of CRs in DSA ($N(E) \propto E^{-2}$), and the red line is the concave spectrum in NLDSA.

the far upstream. They feel the total compression ratio larger than 4. Therefore, the hardening effect is significant in higher energy regime. On the other hand, relatively low-energy CRs with smaller mean free paths diffuse around the subshock and see a smaller compression ratio than 4, leading to a softer spectrum in this energy range. Consequently, the energy spectrum in the whole energy range may become concave as shown in Figure 1.10. This spectral characteristic may explain recent X-ray and γ-ray observations of young SNRs [Vink et al., 2006; Morlino and Caprioli, 2012].

It is the well-known that the steady-state CRMSs generally have the multiples solutions on the same upstream parameter. Figure 1.11 shows the steady-state solutions of CRMSs in the two-fluid model [Drury and Völk, 1981]. It shows the normalized downstream CR pressure $p_c/(\rho u^2 + p_g + p_c)$ as a function of the upstream CR pressure fraction $N = p_c/(p_g + p_c)$ for the upstream Mach number $M = u/\sqrt{(p_g + p_c)/\rho} = 6.0$. Compared with the test-particle limit (dashed-dotted line) that shows the linear behavior, the time-asymptotic states have up to three solutions for a given upstream state when $N \lesssim 0.07$. Differences in the downstream CR pressure fractions mean that the CR production efficiencies in the steady-states are different among these three solutions. Therefore, these solutions may be called "efficient", "intermediate", and

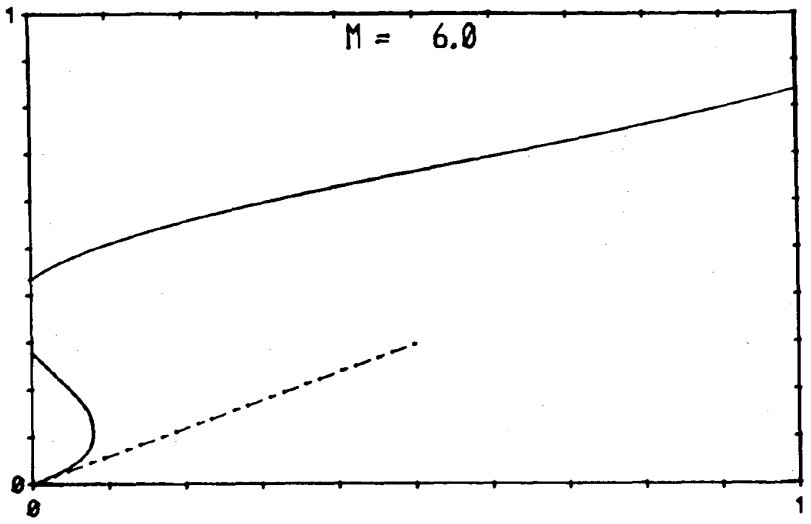

Figure 1.11: Downstream CR pressure fraction (of the total momentum flux) as a function of the upstream CR pressure fraction N (from Drury and Völk [1981]). The solid line and dashed-dotted lines show the solutions for $M = u/\sqrt{(p_g + p_c)/\rho} = 6.0$ and for the test-particle limit.

"inefficient" solutions from the top to bottom. Although the CR production rate in inefficient solutions are more or less similar to the test-particle limit, over 50% or more fraction of CRs are produced in efficient solutions. This multiple-valued steady-state solutions of CRMSs are observed not only in the two-fluid model, but also in CR-kinetic model.

Recent major topic concerned with NLDSA is the magnetic field amplification. X-ray observations of young SNRs reveals the magnetic fields amplified to $\sim 100\,\mu$G [Berezhko and Völk, 2004; Ballet, 2006], or up to $\sim 1\,$mG in the most extreme case of RX J1713.7-3946 [Uchiyama et al., 2007]. These values are the a few hundred - one thousand times larger than the typical value of ISM ($\sim 3\,\mu$G). Theoretically, the amplification of the magnetic fields are required for the DSA theory. Lagage and Cesarsky [1983] estimated the maximum attainable energies expected from DSA in the most optimistic case of the Bohm limit:

$$E_{max} \simeq 10^{13} - 10^{14}\, Z \left(\frac{B}{\mu\mathrm{G}}\right) \left(\frac{V_{shock}}{1000\,\mathrm{km/s}}\right)^2 \left(\frac{t}{1000\,\mathrm{yr}}\right). \tag{1.62}$$

Z is the charge of particles and V_{shock} is the velocity of shocks. The predicted value is not enough to explain the knee energy ($\sim 10^{15}\,$eV), then the increase of B is the one of the keys to solve this problem.

As pointed out for a long time, it is possible that the diffusive flow of CRs toward the upstream can drive the various plasma instabilities in the precursor due to the electric current carried by CRs. If the acceleration of CRs is so efficient that their energy density becomes comparable to the background plasma and that there are the well-developed precursor and CR streaming towards the upstream, these instabilities may amplify the ambient magnetic field in the upstream more than 100 times [e.g. Bell, 2004].

1.4 Motivation

Historically, the concept of CRMSs was proposed about 30 years ago [Drury and Völk, 1981; Axford et al., 1982], many numerical and theoretical approaches were devoted to this topic until now. At the beginning, CRMS was investigated theoretically based on the two-fluid model, where the background plasma and CRs are treated as fluids interacting through the pressure [Drury and Völk, 1981]. Two-fluid model was a first successive model in discussing CRMS, so many derivations of two-fluid model have been proposed until recently Zank et al. [1993]; Webb et al. [1986]. Numerical calculations in the two-fluid model were also conducted by the hydrodynamical simulations [Jones and Kang, 1990] and Monte Calro simulations [Ellison and Eichler, 1984]. Malkov [1997a, b] proposed the model where the hydrodynamical equations and the diffusion-convection equation of CRs were coupled. This model was so-called CR-kinetic model compared to the two-fluid model. They analyzed the steady-state of this model and investigate the behavior of the solutions. Numerically, these equations are solved in two ways, the one is the fully time-dependent simulation [Kang and Jones, 1997; Kang et al., 2002; Kang and Jones, 2005] and another is the semi-analytical method [Blasi, 2002; Amato and Blasi, 2005; Reville et al., 2009; Caprioli et al., 2010]. The latter is the combined method of the analytical formulation of the time-steady solutions of the diffusion-convection equation. Caprioli et al. [2010] qualitatively and quantitatively compared the three different approaches of the fully time-dependent [Kang and Jones, 2007], Monte Calro [Vladimirov et al., 2006] and semi-analytical calculations [Caprioli et al., 2010]. Even though there are differences in these method, they concluded that these methods gave the consistent results in the spectra of CRs and the behaviors of the background

plasma.

In the previous studies, much attentions have been focused on the efficient nature of CRMSs. By the feedback effect of the CRs, the shock compression ratio become larger than that of test-particle limit, this lead to the hardening of the spectrum and enhancement of CRs pressure around the shock. The efficient CRs acceleration in CRMSs can be realized by such a positive feedback effect. In the efficient solutions of CRMSs, above positive feedback effect play a dominant role and the CR production rate is exclusively high. However, in the nature of physics, such a excessive enhancement of high energy particle is not natural. Some regulation mechanism should necessarily depress such a enhancement due to the conservation of energies.

The wave generation in NLDSA may be a good candidate. Actually, some authors recently suggested that we can not dismiss the dynamical feedback of the amplified waves which may have the comparable energy to that of the background plasma, and the dissipation of wave energies [Caprioli et al., 2009; Caprioli, 2012]. In this thesis, we will investigate the general nature of NLDSA and confirm our speculation about how efficiently the NLDSA can produce the CRs.

This thesis is structured as follows. In Chapter 2, we investigate the stabilities of the multiple solutions in the two-fluid model and show which solutions are possibly realized in the nonlinear time evolutions. In Chapter 3, we investigate the more general NLDSA including the wave generation and dissipation in the CR-kinetic model and reveal how the CR production efficiency changes with the effect of waves. In Chapter 4, we show the conclusions of this thesis and the implication for the observations.

Chapter 2

STABILITY OF COSMIC RAY MODIFIED SHOCKS IN THE TWO-FLUID MODEL

2.1 Introduction

The CRMS was firstly studied by using a two-fluid model proposed by Drury and Völk [1981]. In two-fluid model, both the background thermal plasma and CRs are approximated as fluids coupled with each other. The advantage of the two-fluid model is its simplicity making it possible to investigate the property of the system analytically. From the proposal, two-fluid model has been extended by many authors, e.g. the model with the particle injection [Zank et al., 1993], magnetic fields [Webb et al., 1986], radiation [Wagner et al., 2006], and a model with the effect of an acoustic instability [Wagner et al., 2007, 2009] were also proposed.

A peculiar feature of a CRMS is that it possibly has multiple steady-state solutions, i.e., the downstream state cannot be uniquely determined from given upstream parameters. This fact was first pointed out by Drury and Völk [1981] by using a two-fluid model in which CRs are approximated to a massless fluid that interacts with the background plasma through their pressure. Becker and Kazanas [2001] investigated the exact analytical conditions for the exis-

tence of these multiple solutions depending on the Mach number, the specific heat ratio of the background plasma and CRs in the two-fluid model. This model was extended to include the effect of injection [Zank et al., 1993], magnetic fields [Webb et al., 1986], and to a fully kinetic treatment in which the diffusion-convection equation for CRs and the hydrodynamic equations for the background plasma are coupled with each other [Malkov, 1997a, b; Malkov and Völk, 1996; Malkov and Drury, 2001; Blasi et al., 2005; Amato et al., 2008; Reville et al., 2009]. Although the detailed structure of solutions depends on the model, they all possess up to three distinct solutions in some regions in parameter space, indicating that this is a generic feature of the nonlinear shock. A question naturally arises as to which of these solutions indeed exist in nature as the time-asymptotic state of a nonlinear particle-accelerating shock. It is particularly important because the problem is intimately linked to the maximum energy attainable through the acceleration process in the efficient branch as well as the CR scenario of magnetic field amplification. Understanding the stability of these multiple solutions is thus crucial for modeling broadband spectra of astrophysical shocks, from which physical parameters of the acceleration sites can be deduced.

In the original paper of Drury and Völk [1981], they suggested the possibility of intermediate branch being unstable and these three branches may have a "bistable" feature. They conjectured that when the downstream CRs increases (decreases) from the intermediate branch, a self-induced increase (decrease) may bring the solution toward the efficient (inefficient) branch. We note that the intermediate branch was previously shown to be "corrugative" unstable against perturbations transverse to the shock [Mond and Drury, 1998]. Donohue et al. [1994] conducted time-dependent numerical simulations adopting the two-fluid model, and confirmed that the inefficient and the efficient branches exist at least as the time-asymptotic states. Particularly for the efficient branch, it is known that the acoustic instability occur in the precursor region, and analytical as well as numerical studies on this instability have been given so far [Drury and Falle, 1986; Ryu et al., 1993; Drury and Downes, 2012]. Nevertheless, to the authors knowledge, a comprehensive investigation of the stability of these multiple solutions has not been given even within the framework of the two-fluid model. In this chapter, we study the stability of the

global CRMS structure in various parameter regimes by means of one-dimensional (1D) direct time-dependent numerical simulations of the two-fluid equations.

2.2 Basic Equations of Two-Fluid Model

The basic equations of the two-fluid model are

$$\frac{\partial \rho}{\partial t} + \nabla \cdot (\rho \boldsymbol{u}) = 0, \tag{2.1}$$

$$\frac{\partial}{\partial t}(\rho \boldsymbol{u}) + \nabla \cdot \left[\rho \boldsymbol{u} u + \left(p_g + p_c + \frac{B^2}{2} \right) \boldsymbol{I} - \frac{\boldsymbol{B}\boldsymbol{B}}{\mu} \right] = 0, \tag{2.2}$$

$$\begin{aligned} &\frac{\partial}{\partial t} \left[\frac{1}{2} \rho u^2 + E_g + E_c + \frac{B^2}{2\mu} \right] \\ &+ \nabla \cdot \left[\left(\frac{1}{2} \rho u^2 + E_g + p_g + E_c + p_c \right) \boldsymbol{u} + \frac{1}{\mu} - \boldsymbol{E} \times \boldsymbol{B} - \kappa \nabla E_c \right] = 0, \end{aligned} \tag{2.3}$$

$$\frac{\partial E_c}{\partial t} + \nabla \cdot (\boldsymbol{u} E_c) + p_c (\nabla \cdot \boldsymbol{u}) - \kappa \nabla^2 E_c = -\alpha \nabla \cdot \boldsymbol{u}, \tag{2.4}$$

$$\frac{\partial \boldsymbol{B}}{\partial t} = \nabla \times (\boldsymbol{u} \times \boldsymbol{B}), \tag{2.5}$$

$$\boldsymbol{E} = -\boldsymbol{u} \times \boldsymbol{B}, \tag{2.6}$$

$$E_g = \frac{p_g}{\gamma_g - 1}, \tag{2.7}$$

$$E_c = \frac{p_c}{\gamma_c - 1} \tag{2.8}$$

where ρ, u, p_g and μ denote the density, flow velocity, and pressure of the thermal component and the magnetic permeability, $\boldsymbol{I}$, $\boldsymbol{E}$ and $\boldsymbol{B}$ are the unit tensor and the electric and magnetic fields. Throughout this study, $\gamma_g = 5/3$ and $\gamma_c = 4/3$ are assumed for the specific heat ratios of the background plasma and CRs, respectively.

For the simplicity, arbitrary spatial and energy dependences of the diffusion coefficient κ is eliminated ($\kappa = \text{constant}$) and we assume that the diffusion of CRs are isotropic to the magnetic fields because the gyro radius of CRs are quite large.

The most crucial difference of the two-fluid model from kinetic models is probably the absence of the maximum CR energy, which introduces differences in the steady-state solutions. However, we believe that it will not affect the stability property of the system (see discussion in Section

2.4 for details).

2.2.1 Thermal leakage injection model

We adopt the injection model proposed by Zank et al. [1993] based on the idea of thermal leakage. It defines the momentum boundary p_0 above which particles are considered to be CRs and their transport obeys the diffusion-convection equation (1.22). Namely, heating of the gas component injects a fraction of thermal particles into CRs. Under the assumption, the CR pressure p_c and the CR internal energy density E_c are defined as follows,

$$p_c(x) = \frac{4\pi}{3}\int_{p_0}^{\infty} p^3 v f(x,p) dp, \tag{2.9}$$

$$E_c(x) = 4\pi\int_{p_0}^{\infty} p^2 T(p) f(x,p) dp, \tag{2.10}$$

Integrating the diffusion convection equation (1.22) above p_0 in momentum space leads to Equation (2.4). The particle injection term appears in the right hand side because of this lower limit of integration. The injection parameter α defined as

$$\alpha = \frac{4\pi}{3} E(p_0) p_0^3 f(p_0), \tag{2.11}$$

represents the energy density of the injected particle flux. Since the particle injection term is written as a product of α and the spatial gradient of the flow,

$$S = \alpha \frac{\partial u}{\partial x}, \tag{2.12}$$

the injection at the subshock is dominant over the precursor. Notice that the parameter α must be a function of both space and time because it is a quantity determined by local density and temperature of the thermal plasma. Zank et al. [1993] and Donohue et al. [1994], however, assumed that it is constant to make the problem analytically tractable.

In numerical simulations, we can easily calculate α more rigorously for a given momentum boundary p_0 by assuming a distribution function of the background plasma $f_{th}(p)$. For this

purpose, we adopt the (non-relativistic) Maxwellian distribution

$$f_{th}(p) = n\left(\frac{1}{2\pi m k_B T}\right)^{3/2} \exp\left[-\frac{p^2}{2mk_B T}\right], \tag{2.13}$$

where m, n, T are the proton mass, density and temperature of the background plasma and k_B denotes the Boltzmann constant, respectively. The parameter α can then be written as follows,

$$\alpha(p_0) = \frac{4\pi}{3} E(p_0) p_0^3 f_{th}(p_0). \tag{2.14}$$

The particle kinetic energy is given in the relativistic form $E(p) = \sqrt{1+(p/mc)^2} - 1$, where c is the speed of light. In this thesis, the injection model given by the equation (2.14) is referred to as self-consistent.

Note that the injection momentum p_0 is typically chosen to be a few times the downstream thermal momentum $p_{th} = 2\sqrt{mk_B T_{down}}$. This choice is motivated by the fact that suprathermal particles in the downstream region leaking out toward the upstream can be a seed population to the acceleration process. The most important feature of the self-consistent injection model is that the injection efficiency is regulated in response to the downstream temperature changes due to the dynamical shock modification. One can expect that the increase in CR pressure tends to reduce the subshock strength and thus the injection efficiency and vice versa. Despite a simplified manner, a self-consistent regulation of the injection takes into account the feedback effect at least qualitatively.

In this study, we investigate both cases; the constant-α injection (Section 2.3.3) and the self-consistent injection (Section 2.3.4) to clarify the role of injection on the stability of CRMSs.

2.2.2 Analytical solutions of cosmic ray modified shocks in the two-fluid model

Analytical steady-state CRMS solutions to the equations (2.1)-(2.8) were obtained by some authors. When the parallel shock is assumed, we can simplify the basic equations to one-dimensional hydrodynamical equations by neglecting the term involving the magnetic fields. In such a hydrodynamical treatment, the steady-state solutions were obtained for non-injection

case ($\alpha = 0$) [Drury and Völk, 1981] and injection case with a constant α [Zank et al., 1993], which are the extension of the non-injection case. When the oblique shock is taken into account, the steady solutions without the particle injection were obtained by Webb [1983], and investigated closely by Webb et al. [1986]. We here briefly review the basic characteristics of these solutions.

The solution in the non-injection case of the parallel shocks, in which acceleration of pre-existing CRs is considered, is characterized by the Mach number M and the fraction of CRs N in the far upstream

$$M = \frac{u}{C_s}, \tag{2.15}$$

$$N = \frac{p_c}{p_g + p_c}, \tag{2.16}$$

where $C_s = \sqrt{\gamma_g p_g / \rho}$ is the sound speed of the background plasma. The solid line in Figure 2.1 shows the relation between N and the downstream CR pressure $p_{c,down}$ for an upstream Mach number of $M = 6.5$. One immediately finds that, for $N \lesssim 0.07$, multiple solutions exist for a given upstream state. This is a distinct feature for the system absent in the hydrodynamic shock. For convenience, we shall call these solutions, "efficient", "intermediate", and "inefficient" from the top to bottom as shown in Figure 2.1, as they are characterized by CR production efficiencies. The inefficient branch essentially corresponds to the test particle limit and the modification is of only minor importance. On the other hand, CRs absorb most of the kinetic energy in the efficient branch. The substantial difference in the CR production efficiency, more than one order of magnitude between the two in this particular case, motivates us to investigate the stability of the multiple solutions.

Note that the subshock appears only in a relatively low CR fraction N and Mach number M in the two-fluid model. For sufficiently large values of N and/or M, the subshock eventually disappears and the smooth transition connects quantities between the upstream and downstream. The absence of the subshock may be, however, an artifact of the two-fluid model. It has been shown that the subshock always exists in a fully kinetic treatment [Malkov and Drury, 2001].

We thus concentrate our discussion on the solution involving the subshock.

The basic feature does not change even when the injection is taken into account. The dashed line of Figure 2.1 shows the same diagram for the injection case with a constant $\alpha/p_{g,up} = 0.1$ for a modified upstream Mach number $M^* = 6.5$. The modified Mach number $M^* = u/C_s^*$ is defined in terms of the sound speed

$$C_s^* = \sqrt{\frac{\gamma_g p_g}{\rho}\left(1 - \frac{\gamma_g - 1}{\gamma_g}\frac{\alpha}{p_g}\right)}, \tag{2.17}$$

modified by the effect of injection. The structure of the solution is essentially the same as the non-injection case. It may be seen that the range of parameter N where multiple solutions exist is somewhat narrower in the injection case, which reflects the role of injection; i.e., it effectively increases the CR pressure. According to Zank et al. [1993], there are solutions involving not only a precursor, but also a *postcursor* behind the subshock which is not seen in the non-injection case. However, we do not consider such solutions in this chapter for simplicity and focus on the stability of multiple solutions.

Furthermore, by adopting the CR pressure to MHD equations, the characteristic velocities; the velocities of the fast and slow mode are modified,

$$\left(V_{f,s}^*\right)^2 = \frac{1}{2}\left[V_A^2 + C_{sc}^2 \pm \left(\left(V_A^2 + C_{sc}^2\right) - 4V_A^2 C_{sc}^2\right)^{1/2}\right], \tag{2.18}$$

where V_A and $C_{sc} = \sqrt{(\gamma_g p_g + \gamma_c p_c)/\rho}$ are Alfvén and the modified sound velocities. For MHD shocks, it is known that there are 3-types shocks: fast, intermediate and slow shocks. In our research, we treat only the first mode shocks, because we assume the first-mode blast waves of SNRs. The solution is characterized by the fast-mode Mach number M_f, the fraction of CRs N, plasma beta β and shock angle θ in the far upstream

$$M_f = \frac{u}{V_f^*}, \tag{2.19}$$

$$\beta = \frac{p_g}{B^2/2\mu}. \tag{2.20}$$

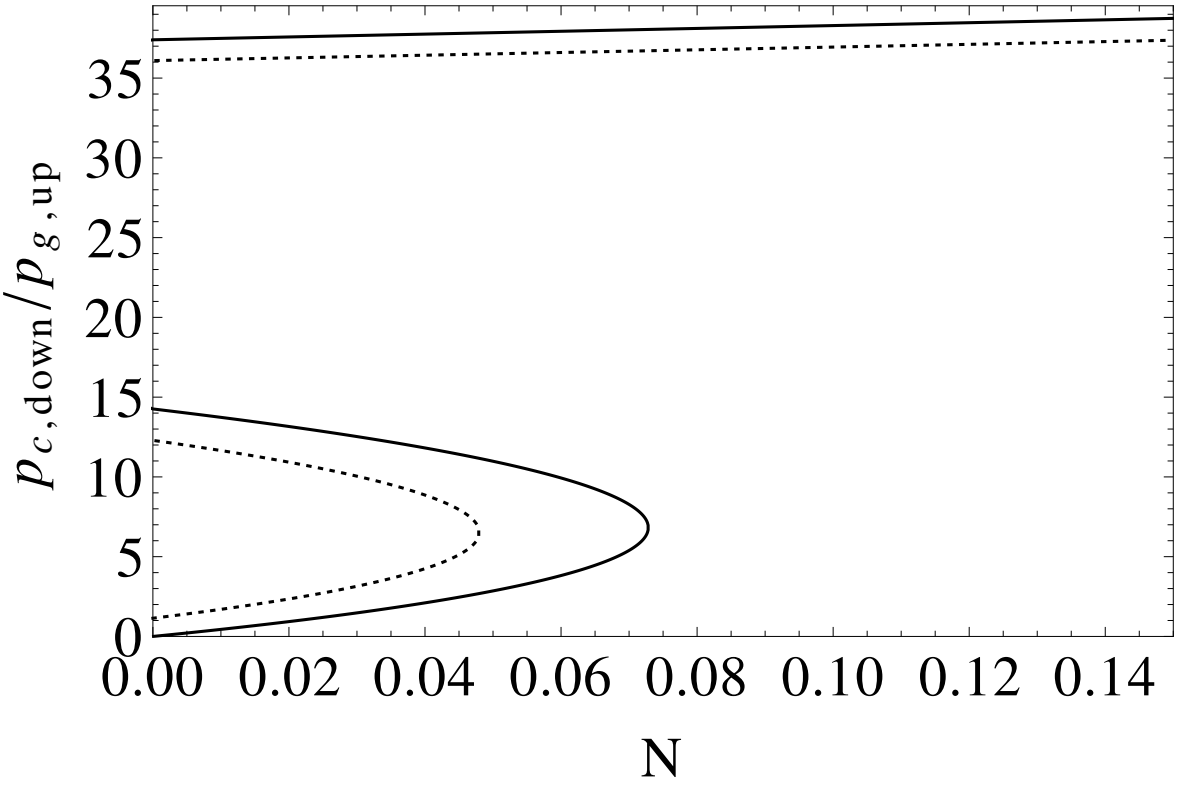

Figure 2.1: Downstream CR pressure p_c as a function of the upstream CR fraction N. The solid and dashed lines show solutions for $M = 6.5$, $\alpha = 0$, and $M^* = 6.5$, $\alpha/p_{g,up} = 0.1$, respectively.

The dash-dotted line in Figure 2.1 shows the relation between N and the downstream CR pressure $p_{c,down}$ for $M_f = 6.5$, $\beta = 5$ and $\theta = 30^\circ$. The effects of magnetic fields also do not influence the whole structure of steady-state solutions compared with the parallel (hydrodynamical) shocks.

2.3 Stability of Global Shock Structure

The stability of the global structure of the steady-state solutions of CRMS is investigated by direct time-dependent numerical simulations of the two-fluid equations (2.1)-(2.8). As for the numerical method, we adopt a splitting method [Dahlburg et al., 1987] in solving the equations (2.1)-(2.4). Namely, we split the time step into a diffusion phase and a non-diffusion phase. In the diffusion phase, the following equation is solved (here a constant diffusion coefficient κ is assumed),

$$\frac{\partial p_c}{\partial t} = \kappa \frac{\partial^2 p_c}{\partial x^2}, \tag{2.21}$$

in an implicit manner using the Bi-CGSTAB method [van der Vorst, 1992] to update the CR pressure to p_c^*. In the non-diffusion phase, we solve the equations (2.1)-(2.4) without the diffusion term by the modified Lax-Wendroff method [Rubin and Burstein, 1967], which has the second-order accuracy both in time and space, using p_c^* updated in the diffusion phase. For the CFL condition, we adopt a variable time step such that $\Delta t = 0.1\Delta x/\max(u + C_{sc})$ for hydrodynamical calculations and $\Delta t = 0.1\Delta x/\max(u + V_f^*)$ for magnetohydrodynamical calculations, where Δx is the grid spacing, and $\max()$ indicates the maximum value in the simulation box.

The number of grids is set to be $N_x = 5000$, which we believe is sufficient for the following reasons. Frank et al. [1994, 1995] concluded that their numerical solutions of MHD-CRMSs well converge to analytical ones when sufficiently high resolution is used $n_r \gtrsim 10 - 20$, where n_r is defined as $n_r = \kappa/(u_s \Delta x)$ (where u_s is the shock speed). In the present calculations, the parameter is always chosen to be $n_r > 100$, sufficient to give numerical solutions with reasonable accuracy and discuss the stability of the analytical solutions. We employ the fixed boundary at the left-hand (upstream) side and the free boundary ($\partial/\partial x = 0$) at the right-hand (downstream) side of the box. We have checked that the boundary conditions do not influence our numerical results by enlarging the simulation domain by five times. Space and time are respectively normalized to the diffusion length κ/u_{up} and the diffusion time κ/u_{up}^2. Note that our simulations are conducted in the shock-frame, so $u_{up} \sim u_s$.

2.3.1 Parallel shock calculations without injection ($\alpha = 0$)

We choose an analytical steady-state solution as an initial condition for the time-dependent simulation to investigate the stability. While we do not put any perturbations into the simulation, it evolves from those caused by numerical errors mainly at the subshock inherent in any finite difference schemes.

In this section, we study the non-injection case $\alpha = 0$ of the parallel shocks corresponding to Drury and Völk [1981]. Figures 2.2(a)-(d) show the results for $N = 0.1$ and $M = 6.5$ in which only one solution involving a subshock exists. In these kind of simulations, we have found that a numerical solution always evolves into a steady state from which no appreciable changes are

observed, which is then regarded as the final state. One finds that the final state (solid line) is almost unchanged from the initial condition (dashed line), suggesting that the solution is stable.

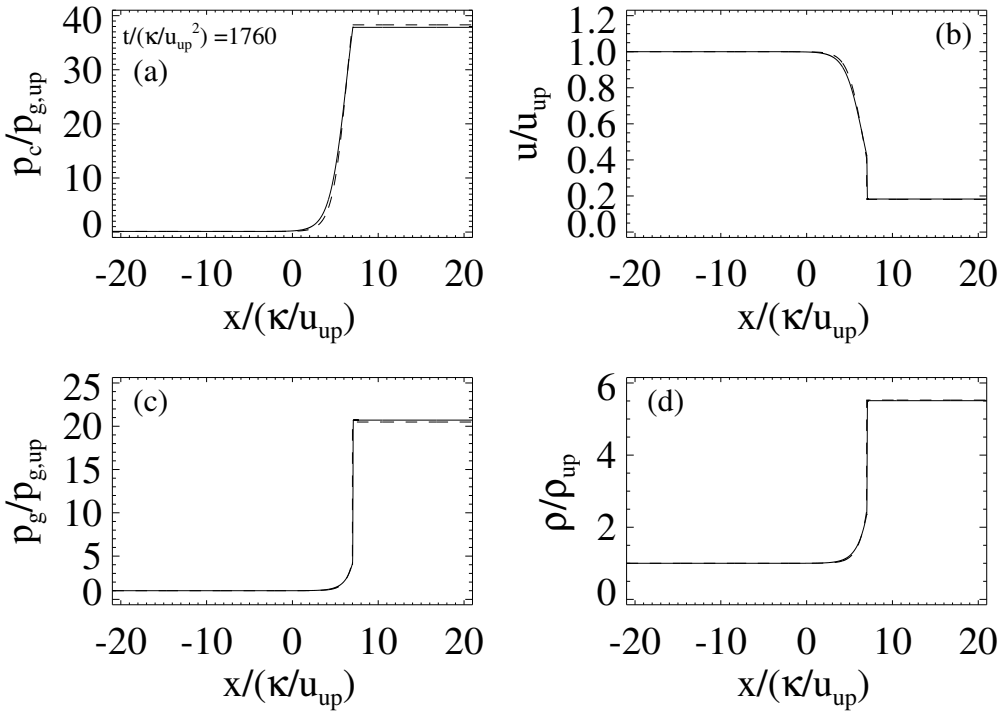

Figure 2.2: Numerical solution for a CRMS with $M = 6.5$ and $N = 0.1$ where only one solution exists. Normalized profiles of (a) the CR pressure, (b) background plasma flow velocity, (c) background plasma pressure, and (d) background plasma density are shown. $p_{g,up}$, u_{up}, and ρ_{up} are the upstream background plasma pressure, flow velocity, and density, respectively. The initial and final states ($t/(\kappa/u_{up}^2) = 1760$) are shown in dashed and solid lines respectively.

Figures 2.3 - 2.5 compare the results of three analytical solutions corresponding to the efficient, intermediate, inefficient branches found for $N = 0.05$, respectively. We see that the downstream CR pressures of the efficient and inefficient branches appear to be almost unchanged (Figures 2.3(a)-(d) and 2.5(a)-(d)), while that of the intermediate branch decreases significantly (Figures 2.4(a)-(d)). This result indicates that the intermediate branch is unstable while the others are stable. Note that the difference between the background plasma parameters of the initial and final states is relatively minor compared to the CR pressure for the simulation started from the intermediate branch. We find that the final state in this case corresponds to the inefficient solution. The reason for the minor difference in the background plasma parameters is that the shocks of both the initial and final states are intrinsically weakly modified ones. Strictly speaking, the downstream CR pressure of the inefficient branch shows a slight decrease, which

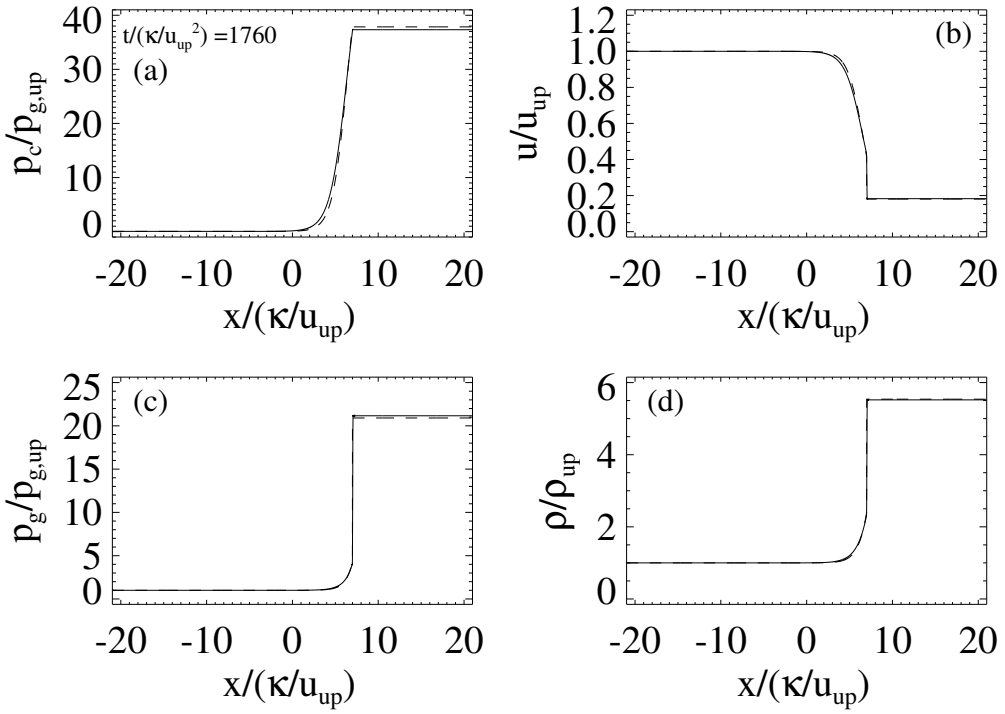

Figure 2.3: Numerical solution for the efficient branch at $t/(\kappa/u_{up}^2) = 1760$ ($M = 6.5$ and $N = 0.05$). The format is the same as Figure 2.2.

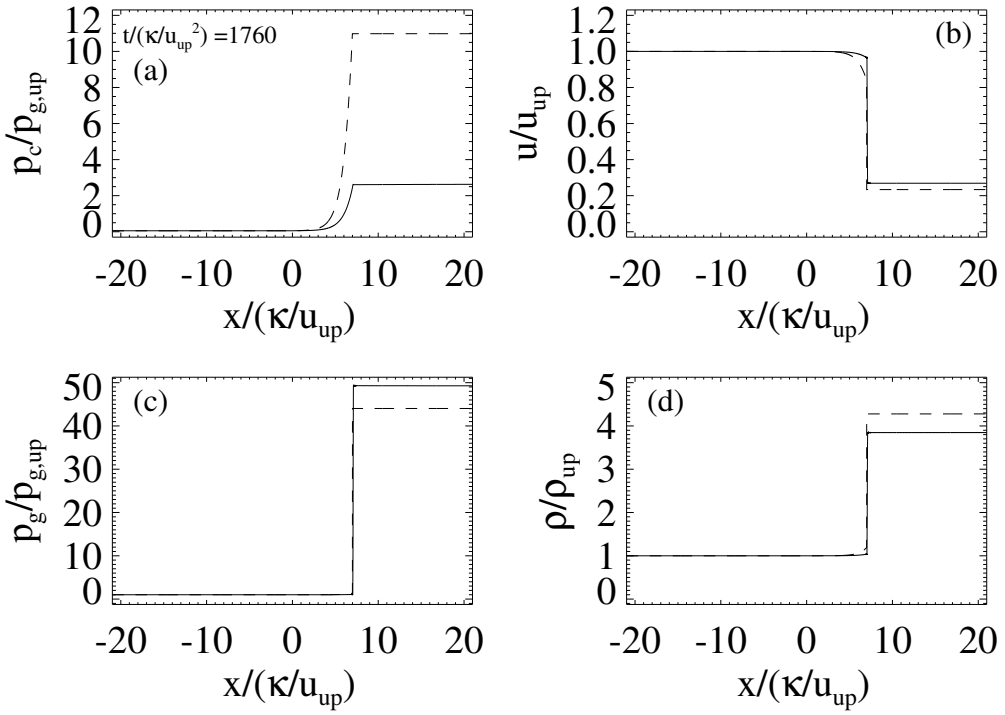

Figure 2.4: Numerical solution for the intermediate branch at $t/(\kappa/u_{up}^2) = 1760$ ($M = 6.5$ and $N = 0.05$). The format is the same as Figure 2.2.

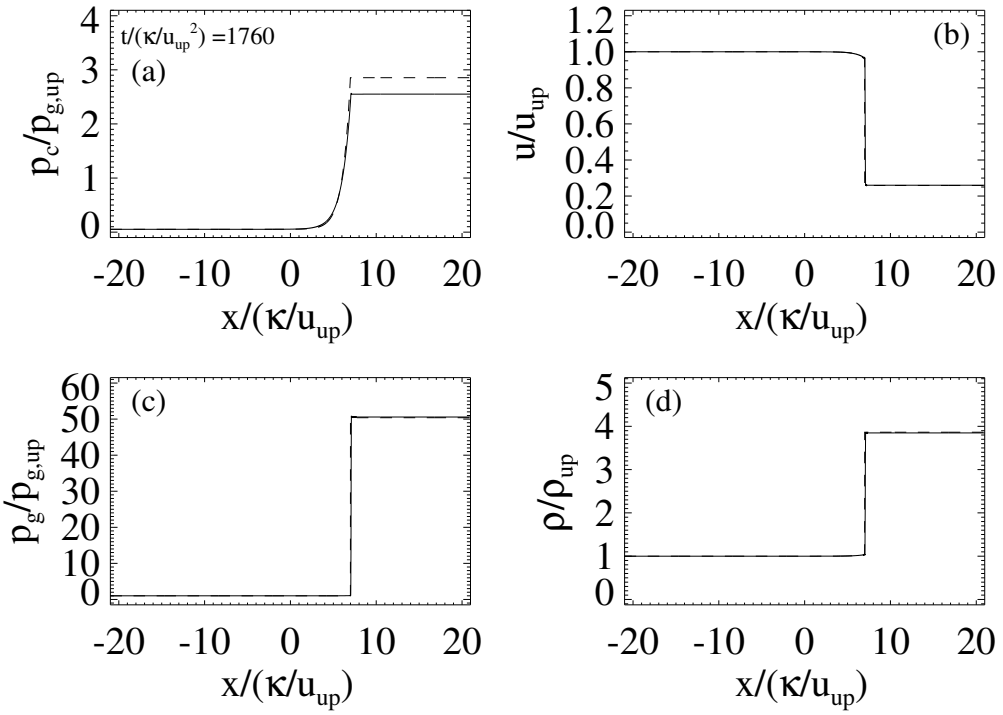

Figure 2.5: Numerical solution for the inefficient branch at $t/(\kappa/u_{up}^2) = 1760$ ($M = 6.5$ and $N = 0.05$). The format is the same as Figure 2.2.

we think is numerical. As we mentioned earlier, we have checked the convergence of numerical solutions to the analytical ones by increasing the resolution.

Figure 2.6 summarizes the results for various initial conditions. Each symbol represents a simulation run for a given upstream CR fraction N. The downstream CR pressure, averaged over 250 grid points near the right-hand side boundary, is shown in the vertical axis. In cases where there exists multiple solutions for a given N, we investigate all the possibilities. The initial conditions are indicated in (a), while the final states $t/(\kappa/u_{up}^2) = 1760$ are shown in (b). As was found in the case of $N = 0.05$, the efficient and inefficient branches exhibit only slight changes from the initial conditions due to numerical errors as mentioned above. On the other hand, the intermediate branch always shows the transition to the inefficient branch. This has been confirmed in the range $5 \leq M \leq 15$, $0.01 \leq N \leq 0.13$, whenever multiple solutions exist. The sampling intervals for M and N are 0.5 and 0.02, respectively. Note that, for higher Mach numbers, there exists only one solution (corresponding to the efficient state) in the range $N \geq 0.01$.

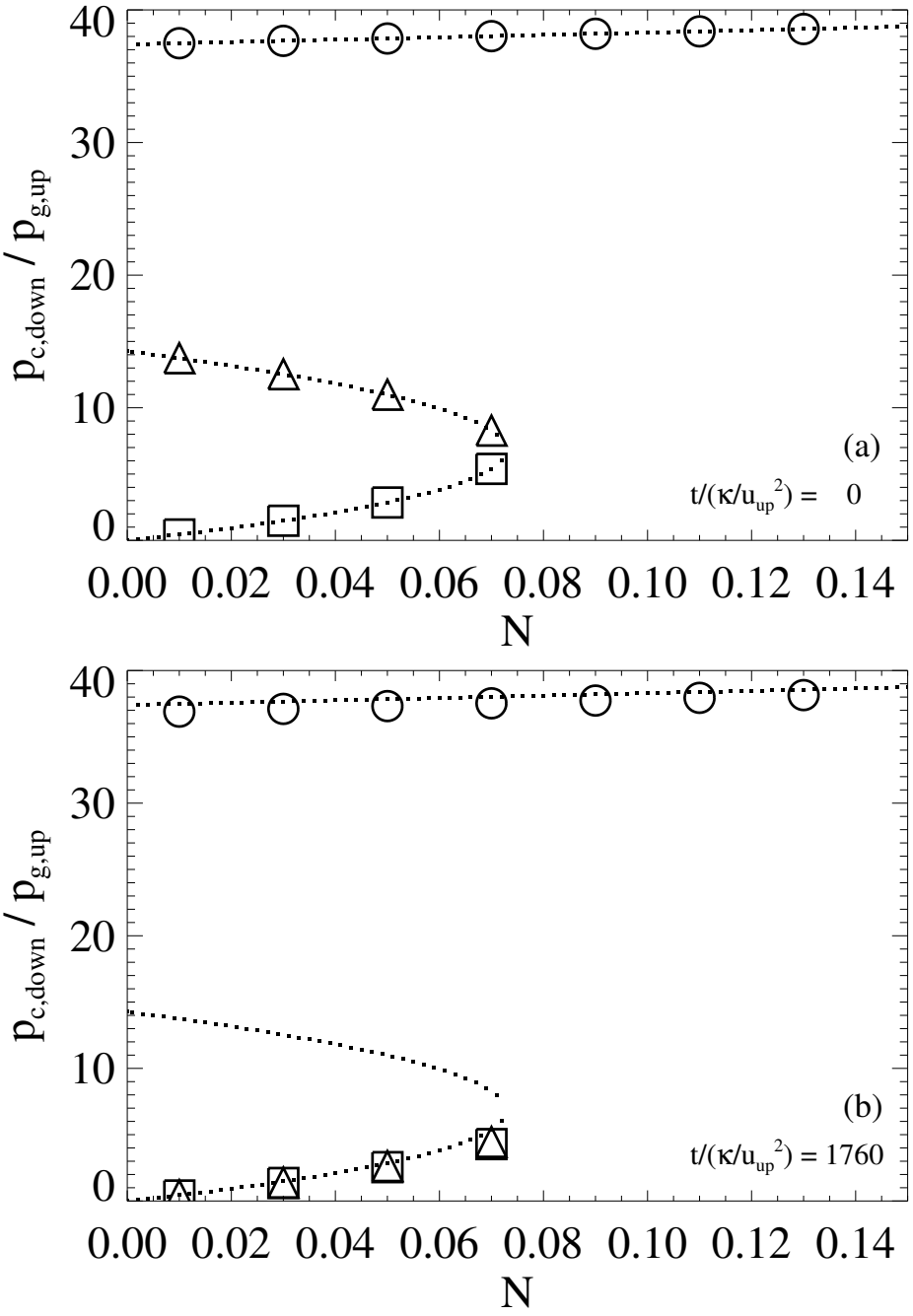

Figure 2.6: Summary of simulation results, for the parallel shocks without injection, $M = 6.5$ and $\alpha/p_{g,up} = 0$ (constant) at (a) the initial state and (b) the final state. The dotted line indicates the analytical steady-state solution. Open circle, open triangle and open square show the results for the efficient, intermediate and inefficient branches respectively. Simulations were conducted at $N = 0.01$, 0.03, 0.05, 0.07, 0.09 0.11, and 0.13.

2.3.2 Oblique shock calculations without injection ($\alpha = 0$)

In the calculations of oblique shocks, magnetohydrodynamical equations (2.1)-(2.8) are solved. Figures 2.7(a)-(f) show the results for $N = 0.11$, $M_f = 6.5$, $\theta = 30^\circ$ and $\beta = 5$ in which only one

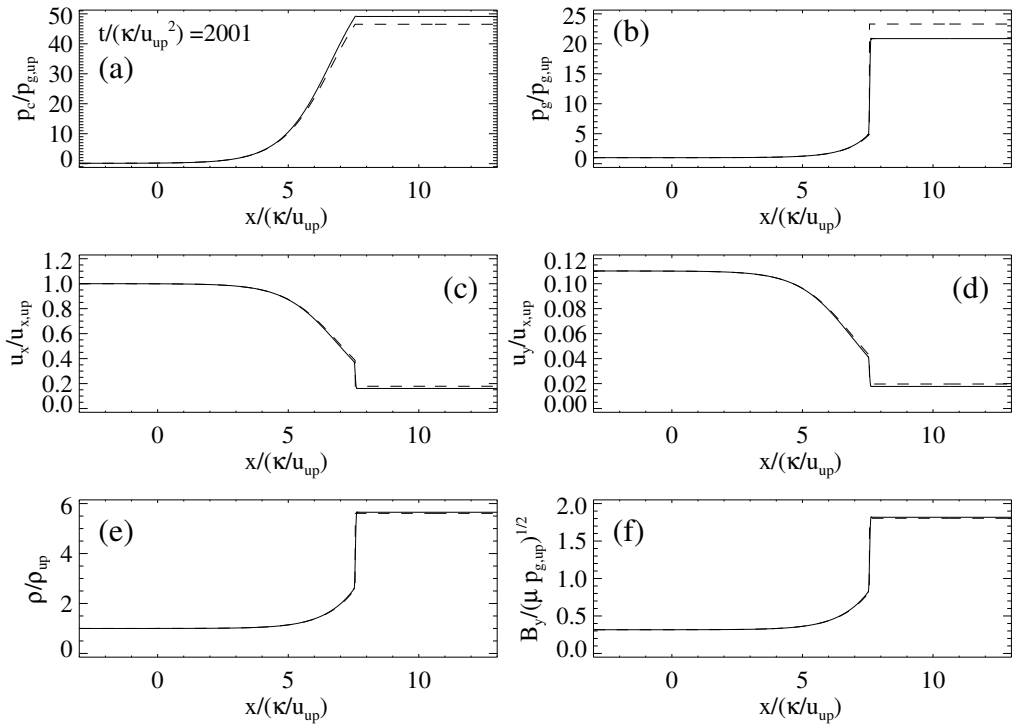

Figure 2.7: Numerical solutions for a MHD-CRMS with $M_f = 6.5$, $N = 0.11$, $\theta = 30^\circ$ and $\beta = 5$, where only one solution exists. Normalized profiles of (a) the CR pressure, (b) background plasma pressure (c) x-component of background plasma flow velocity, (d) y-component of background plasma flow velocity, (e) background plasma density, and (f) y-component of magnetic field are shown. $p_{g,up}$, $u_{x,up}$, and ρ_{up} are the pressure, x-component of flow velocity, and density of the upstream background plasma, respectively. The initial and final states ($t/(\kappa/u_{up}^2) = 2001$) are shown in dashed and solid lines respectively.

solution involving a subshock exists.

Figure 2.8 summarize the results for various initial conditions with the same format as Figure 2.6 for $M_f = 6.5$, $\theta = 30^\circ$ and $\beta = 5$. Similarly to parallel shock calculations, the efficient and inefficient branches are stable and the intermediate branch is unstable. We also conduct same calculations for $5 \leq M_f \leq 10$, $\theta = 30^\circ, 60^\circ, 90^\circ$ and $\beta = 1, 5$. These stability features do not change in all calculations.

2.3.3 Parallel shock calculations with injection ($\alpha \neq 0$)

We now study the effect of injection with a constant injection parameter α. As in the non-injection case, we can use the analytical solutions of Zank et al. [1993] presented in Section 2.2.2 as the initial conditions.

Figure 2.9 shows the results with the same format as Figure 2.6 for $M^* = 6.5$ and $\alpha/p_{g,up} = 0.1$.

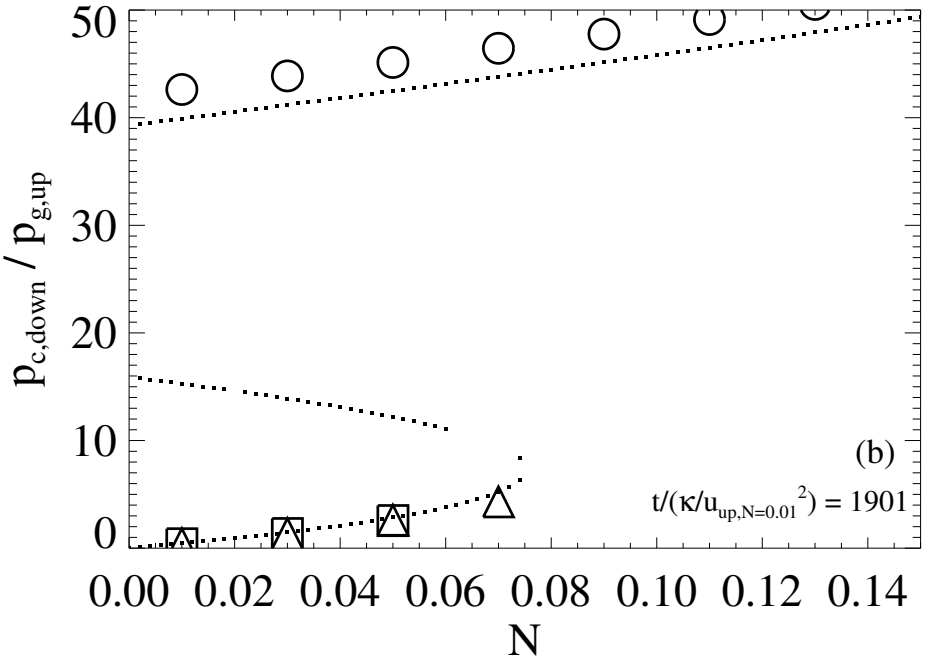

Figure 2.8: Summary of simulation results with $M_f = 6.5$, $\theta = 30^\circ$ and $\beta = 5$ at the final state ($t/\kappa/u^2_{up,N=0.01} = 1901$). The format is the same as Figure 2.6.

Note that the reason why the efficient branch in the injection case is less efficient than that in the non-injection case (which may easily be seen in Figure 2.1) is due to the definition of M^* which is a function of parameter α. One immediately sees that the basic stability property is essentially unchanged, i.e., the efficient and inefficient branches are stable while the intermediate branch is always unstable and evolves into the inefficient one. Extensive parameter survey in the range $0.001 \leq \alpha \leq 1$, $5 \leq M^* \leq 15$ and $0.01 \leq N \leq 0.13$ again confirms that the property does not change, although the use of different parameters modifies the structure of analytical solutions itself (the sampling intervals are the same as previous ones for M^* and N, and 0.001, 0.01, 0.1, 1 for α). One might naively expect that the introduction of injection tends to make the acceleration more efficient, but this is not the case.

2.3.4 Parallel shock calculations with self-consistent injection

Unlike the case with a constant α (including non-injection case), no analytical solution is known for the self-consistent injection case. However, since the injection is the strongest at the subshock where the downstream α plays an essential role, we initialize the simulation in the following way.

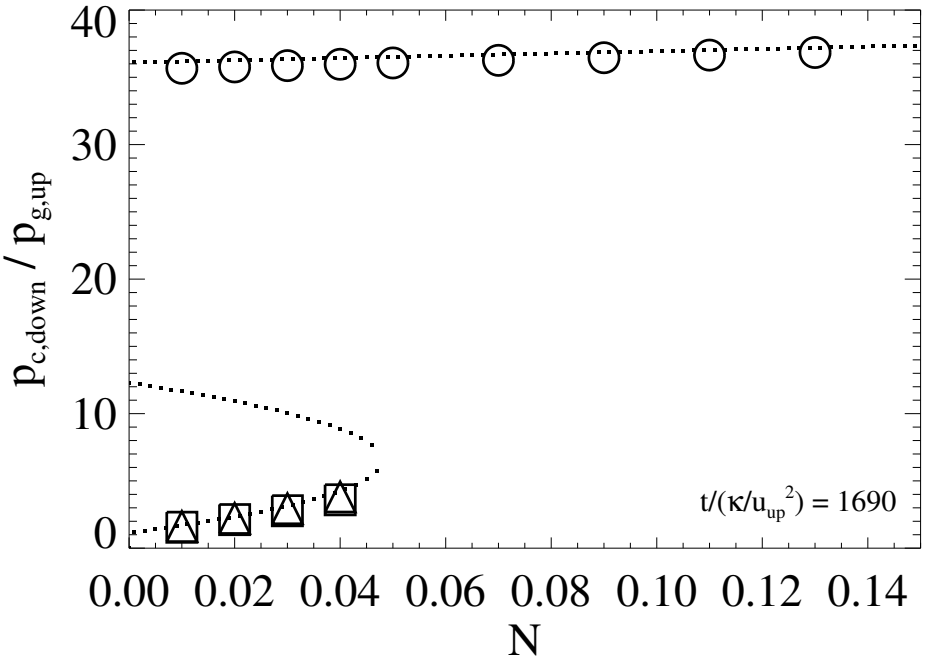

Figure 2.9: Summary of simulation results for the injection case $M^* = 6.5$ and $\alpha/p_{g,up} = 0.1$ (constant) at the final state. The format is the same as Figure 2.6.

First, we set up an initial condition for the background plasma parameters and CR pressure using an analytical solution for a constant α. We then calculate p_0 using the equation (2.14) and the downstream density and temperature T. This p_0 is kept constant during the entire simulation. The parameter α can now be calculated by using the local density and temperature, and thus becomes a function of both space and time. Notice that the parameter α so calculated in the precursor and upstream differs from the original value even at the initial condition. The inconsistency due to this is, however, relatively minor as the injection primarily occurs at the subshock, which is indeed confirmed by simulation results discussed below.

Figure 2.10 shows the results with the self-consistent injection with the same format shown in Figure 2.9. The initial condition is set up by an analytical solution for a constant $\alpha/p_{g,up} = 0.1$. In each calculation, the momentum boundary p_0 differs slightly because we set initial downstream α in all calculations to satisfy $\alpha/p_{g,up} = 0.1$ considering each different downstream state (e.g., $p_0/p_{th} \simeq 2.65$ for $N = 0.13$ and $p_0/p_{th} \simeq 2.75$ for $N = 0.01$ of the inefficient branch). We see that the stability property is essentially not affected by the different injection model. The only difference we can find from Figure 2.10 is that the solutions as a whole slightly shift to lower CR

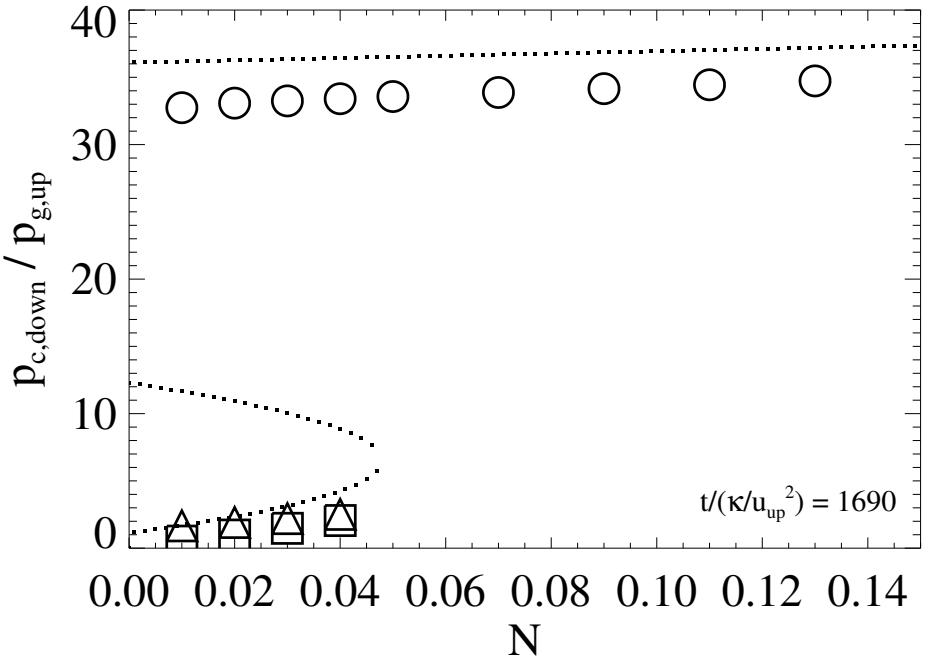

Figure 2.10: Summary of simulation results for the self-consistent injection case $M^* = 6.5$ at the final state. The dotted line indicates the analytical steady-state solution for $\alpha/p_{g,up} = 0.1$ (constant) for reference. The format is the same as Figure 2.6.

pressure states from the initial condition constructed for a constant α. This may be explained by considering a finite subshock width. Namely, since the injection flux is expressed by a product of α and the flow divergence, the strongest injection occurs at the subshock which is resolved by a finite number of grid points. The α parameter calculated by density and temperature in the subshock structure thus gives an intermediate value between the upstream and downstream at which the flow divergence is largest. This means that an effective α is somewhat smaller than the downstream value. We have confirmed that the numerical solutions agree very well with analytical solutions calculated using the effective α parameters evaluated from simulation results (assumed to be constant). Therefore, the differences between the initial and final states are injection model dependent. Such an issue is obviously beyond the scope of the present study, and it should not be taken too seriously. It is rather important to emphasize that the self-consistent injection does not introduce appreciable differences to the stability of the CRMS solutions.

2.3.5 Parallel shock calculations with large-amplitude perturbations

So far we have investigated the stability against relatively small perturbations caused by numerical errors, where the intermediate branch is always unstable and evolves into a less efficient state. For application to realistic astrophysical situations where the shock parameters may change in time (e.g., slowing down of SNR shocks, inhomogeneous upstream media), it may also be important to understand the stability property against large-amplitude perturbations.

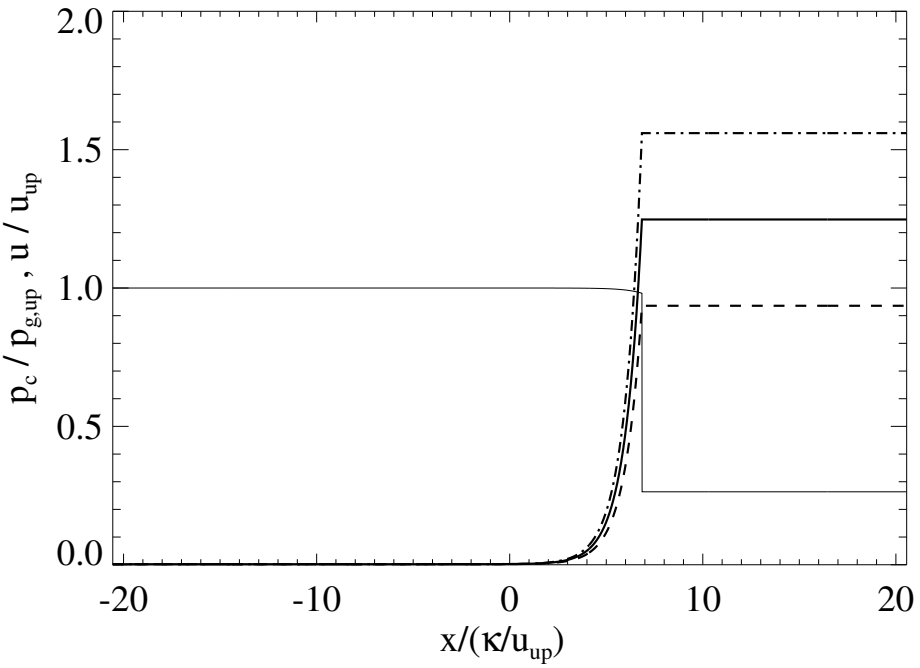

Figure 2.11: Initial profiles of perturbed CR pressure p_c for the inefficient solution with $M^* = 6.5$, $N = 0.002$, and $\alpha/p_{g,up} = 0.1$. The thin and thick solid lines show respectively the flow velocity and the CR pressure for the analytical solution. Perturbed CR pressure profiles by amount $\pm 25\%$ are shown in the dashed and dashed-dotted lines respectively.

We investigate the response of the system against large-amplitude perturbations. Specifically, we change the downstream CR pressure $p_{c,down}$ at the initial condition to investigate the behaviors in the $N - p_c$ diagram. Figure 2.11 shows an example of perturbed and unperturbed profiles of the CR pressure. In order to obtain an initial perturbed profile $p_c^{'}(x)$, we multiply the analytical solution $p_c(x)$ by a constant factor corresponding to the amplitude of perturbation. On the other hand, hydrodynamic quantities u, p_g and ρ are remain unchanged. Figures 2.12 and 2.13 show the response of the system obtained by numerical simulations for (a) the

inefficient, and (b) the efficient branches, respectively. We choose an analytical steady-state solution for $M^* = 6.5$, $N = 0.002$, and a constant $\alpha/p_{g,up} = 0.1$ on which initial large-amplitude perturbations are imposed. The results with perturbations up to $\pm 25\%$ of the unperturbed state are shown in these figures. The ratios of the momentum boundary to the downstream thermal momentum for this case are $p_0/p_{th} \simeq 2.35$ and $p_0/p_{th} \simeq 2.47$ for the inefficient and the efficient branches respectively. The CR pressure in the downstream as well as the α parameter shown in Figures 2.12 and 2.13 are calculated by taking the average over the values, respectively in all cells between the downstream boundary and $\sim 10\%$ inside the uniform region downstream. We can see that the injection parameter α immediately increases (decreases) in response to the decrease (increase) in the CR pressure. This confirms the feedback effect of injection due to dynamical modification of the shock. Nevertheless, the simulation results show that the numerical solutions quickly converge into the solution obtained without perturbations, suggesting that these solutions are stable even against large-amplitude perturbations and the injection does not play a role for modifying the stability.

We finally discuss numerical simulation results of time evolution from a hydrodynamic shock with injection. This is particularly important in that it would be more or less similar to the situation realized in a realistic astrophysical scenario. Figure 2.14 summarizes the results for shocks with a Mach number of $M^* = 6.5$ without pre-existing CRs ($N = 0$), with (a) constant-α injection, and (b) self-consistent injection.

For the constant α injection case shown in Figure 2.14(a), we find that the final states of numerical simulations with $0.05 \leq \alpha/p_{g,up} \leq 0.25$ settle into the inefficient branch of the analytical solutions shown by dotted lines at $t/(\kappa/u^2_{up,\alpha=0.05}) = 1760$, where $u_{up,\alpha=0.05}$ is the upstream flow velocity of the background plasma at $\alpha/p_{g,up} = 0.05$. As seen in the equation (2.17), the upstream sound velocity decreases with increase in the parameter α by a factor of $\sqrt{1-(2/5)(\alpha/p_{g,up})}$. Since the upstream flow velocity (u_{up}) depends on α, we choose $u_{up,\alpha=0.05}$ as a representative value for the unit of time. We have also checked the development beyond this time but found no evidence for any further evolution, consistent with the fact that the inefficient branch is stable against large-amplitude perturbations. We also conduct simulations with $\alpha/p_{g,up} = 0.3$ or even

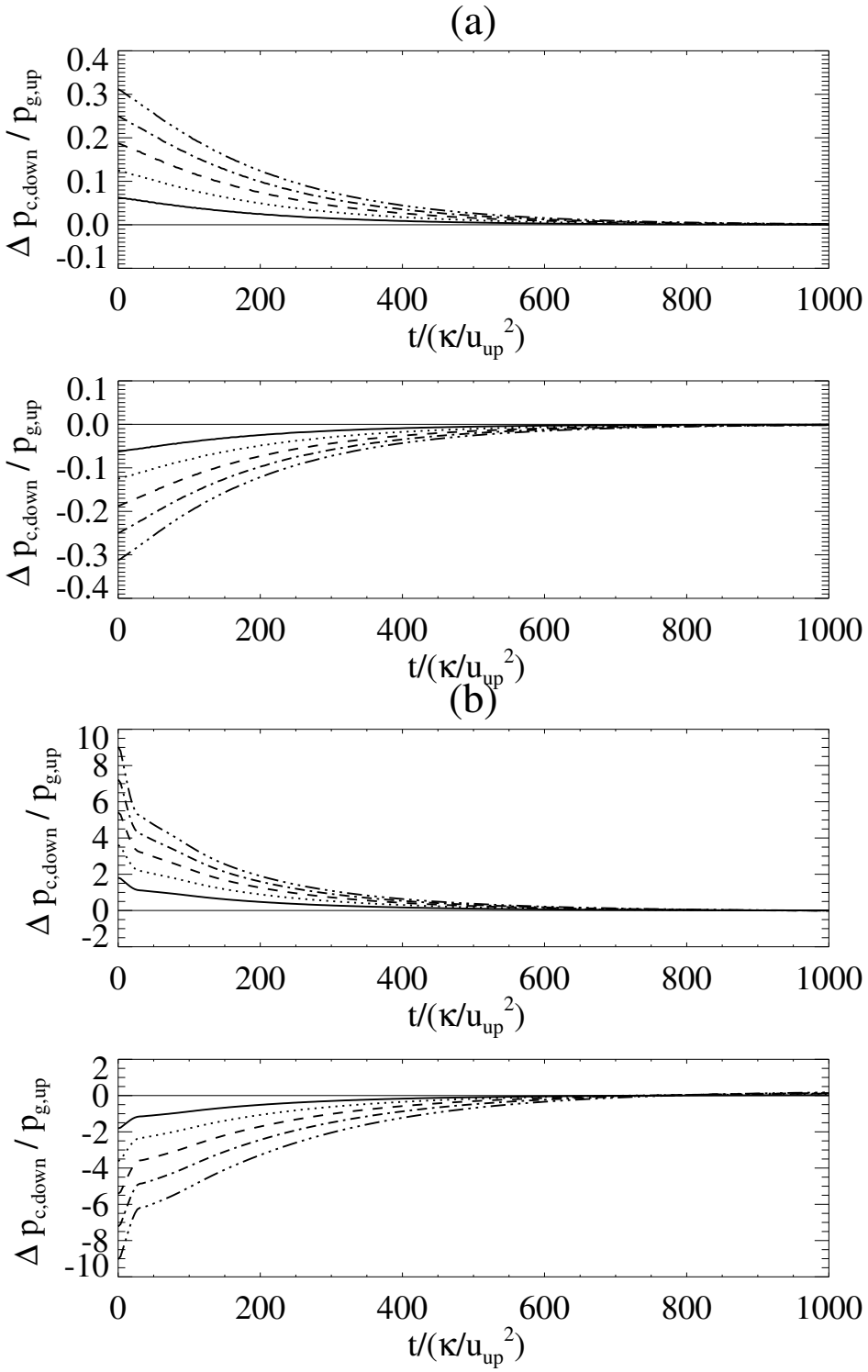

Figure 2.12: Time evolution of the deviation of downstream CR pressure from the unperturbed case for $M^* = 6.5$, $N = 0.002$ and $\alpha/p_{g,up} = 0.1$. The panels (a) and (b) show the inefficient and efficient branches respectively. In each case, positive and negative perturbation runs are shown in the top and bottom. The absolute amplitude of perturbation is shown with different line types (solid: 5%, dotted: 10%, dashed: 15%, dashed-dotted: 20%, dashed double-dotted: 25%).

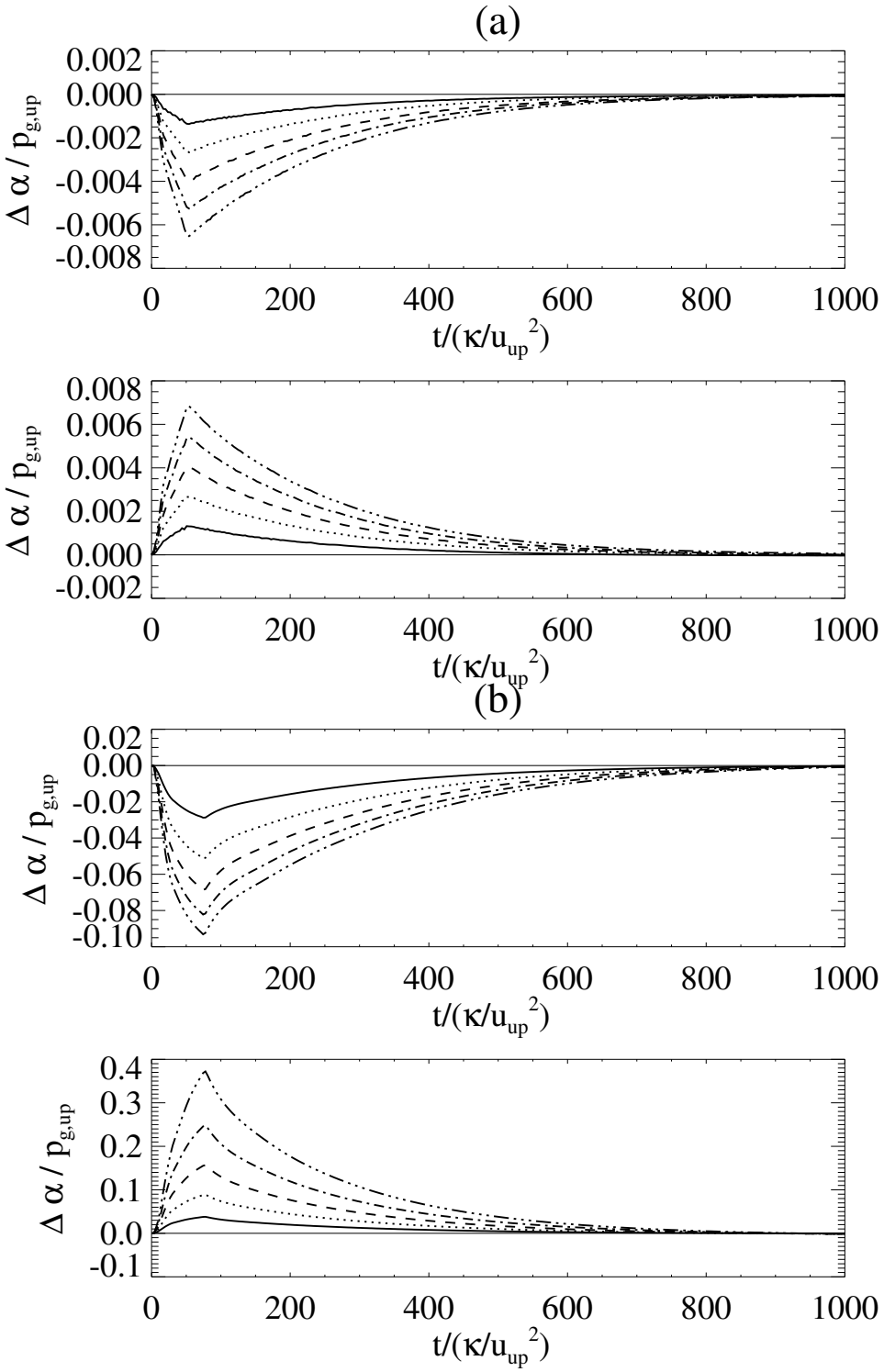

Figure 2.13: The same as Figure 2.12 but for the downstream α.

larger, where only the efficient branch of solution exists. In these cases, the pressure balance across the shock is broken because of strong modification of the shock. As a result, the shock propagates toward upstream and the solution settles into the efficient branch but with a different

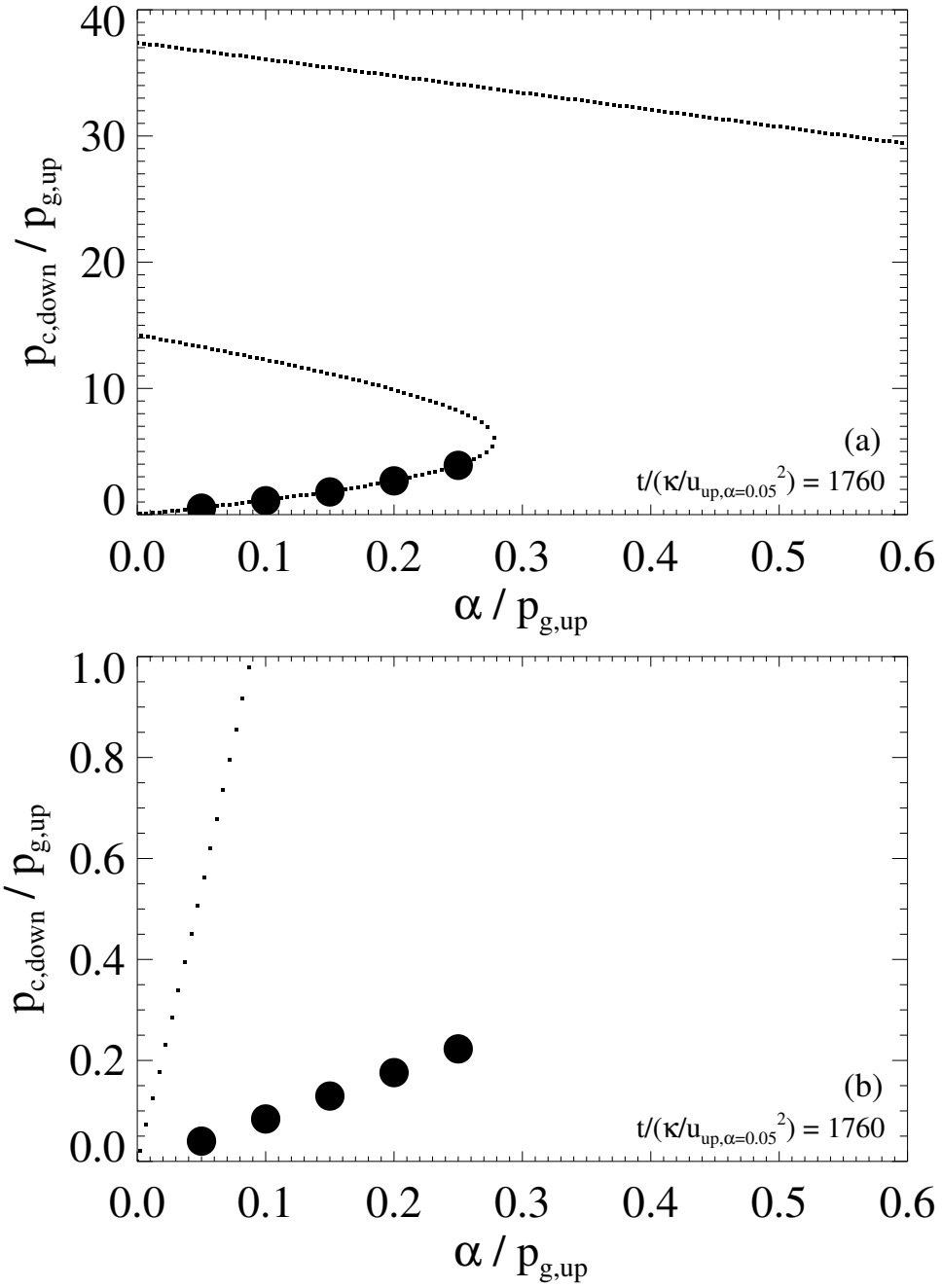

Figure 2.14: Asymptotic states of simulations started from hydrodynamic shocks of $M = 6.5$ with (a) constant α injection, (b) self-consistent α injection. The dotted lines indicate the analytical solution for $M^* = 6.5$ with constant α for reference.

Mach number. Although we are not able to plot the simulation result on Figure 2.14(a) for this reason, it is certainly true that the time asymptotic state is on the efficient branch. One might notice that the CR pressure of the analytical solution on the efficient branch decreases as the injection parameter α increases. This is because the plot is made for a fixed M^* which is a

function of α and is therefore not surprising.

Figure 2.14(b) shows the final states of simulations with the self-consistent injection (notice the different vertical scale). We choose p_0 in such a way that an initial α determined by the downstream background plasma density and pressure corresponds to $0.05 \leq \alpha/p_{g,up} \leq 0.25$. The analytical solution for a constant α is also shown for reference. The simulation results always converge to solutions below the reference solution. The reason for this is the same as that given in Section 2.3.4 (i.e., due to a smaller effective α), and is not important.

All these results indicate that the solutions on the efficient and inefficient branches are stable even against large-amplitude perturbations, independent of the assumption of the injection model. It is also worth mentioning the case with a finite upstream CR fractions ($N > 0$) at the initial state, which is more realistic for the astrophysical applications. In such cases, we have confirmed that the time asymptotic states are also on the inefficient branch if N is relatively low so that the inefficient branch exists. Therefore, if one considers realistic time evolution of an astrophysical shock, the asymptotic state realized in nature will very likely to be the least efficient state in terms of particle acceleration for given upstream parameters.

2.4 Summary and Discussion

In this chapter, we have investigated the stability of the global structure of the CRMS by using the two-fluid model with the effect of injection and magnetic fields. The system is known to have up to three distinct solutions in some regions in parameter space, which are respectively referred to as "efficient", "intermediate", and "inefficient" in terms of corresponding CR production efficiencies. Understanding the stability of these solutions is crucial for the application of non-linear shock acceleration theory to astrophysical shocks. By performing direct time-dependent numerical simulations, we have studied the stability for the multiple solutions in a wide range of parameters space by changing the Mach number $M(M_f, M^*)$, the fraction of upstream pre-existing CRs N, the shock angle θ and the injection parameter α. Our simulation results can be summarized as follows.

Firstly, numerical simulations with three initial states given by the analytical solutions of

CRMSs demonstrate that the efficient and inefficient branches are stable, while the intermediate solution always shifts toward the inefficient branch. This features do not depend on the shock angle, in other words, the magnetic fields do not play a so much role in the stability of CRMSs. We have also confirmed this downward transition even if large-amplitude perturbations are imposed on the intermediate solution independent of the "direction" of perturbation. This result is consistent with the earlier conjecture of the bistable feature suggested by Drury and Völk [1981] even without invoking the so-called corrugation mode known to be unstable in a multi-dimensional system [Mond and Drury, 1998].

Secondly, the stability property does not depend on the injection model and efficiency. We have investigated both the constant-α injection, as well as the self-consistent injection in which α is determined by the instantaneous density and temperature of the background plasma. In particular, the self-consistent injection model implements the feedback effect due to dynamical shock modification. Whereas the structure of steady-state solution certainly depends on the injection, the stability is hardly affected even in the case of self-consistent injection.

Thirdly, the efficient and inefficient branches are shown to be stable even against large-amplitude perturbations, again regardless of the injection model. The feedback effect of the self-consistent injection in response to large-amplitude perturbations to the downstream state does not play a role in regulating the stability. Consequently, a hydrodynamic shock with injection evolves into the inefficient branch whenever it exists as a result of self-consistent time development. For the injection parameter above a critical value in which only one solution corresponding to the efficient branch exists, the shock structure drastically develops into the strongly modified one. This suggests that the time asymptotic solution of the nonlinear shock is likely to be the least efficient state for given parameters of the shock.

Our conclusions on the stability of the CRMS are based on the framework of the two-fluid model. However, judging from the insusceptibility of the stability property to otherwise important shock parameters ($M(M^*)$, N, θ, α and the injection model), we believe that it will remain the same even in a fully kinetic treatment. The limit of the two-fluid model has been discussed in the literature [Kang and Jones, 1990; Jones and Ellison, 1991; Malkov and Drury, 2001]. It

has been suggested that the model gives essentially the correct description of the CRMS provided that the adiabatic index of CRs γ_c is adequately chosen in the range $1 < \gamma_c < \gamma_g$. In the two-fluid model, increase of γ_c results in the shrinkage of the region of multiple solutions and vice versa [e.g., Becker and Kazanas, 2001]. The effective γ_c in a kinetic model is determined by solving self-consistently the modified shock structure. The crucial assumption in doing so is the maximum energy of CRs. Since the CRs absorb the available kinetic energy through the positive feedback of shock modification, the CR production rate tends to diverge and no steady-state solution would be obtained unless one imposes a cut-off energy above which CRs escape from the system. This makes the shock virtually *radiative* in the sense that the effective γ_c approaches unity, which thus enlarges the region of multiple solutions. We have also conducted simulations with different γ_c, and confirmed that the bistable feature is insensitive to this parameter. In any case, solutions of the CRMS based on the kinetic model have been obtained and confirmed the existence of multiple solutions [Malkov, 1997a, b; Malkov et al., 2000; Blasi, 2004; Blasi et al., 2005; Amato et al., 2008; Reville et al., 2009]. Rigorous proof of the stability in the kinetic regime is however left for the future investigation. Note that, in a kinetic model, multiple solutions exist for much higher Mach numbers, e.g., $M > 100 - 1000$, which is not the case in the two-fluid model, probably due to the existence of the cut-off energy. The disappearance of the subshock in the two-fluid model can also be explained similarly.

The fact that both the efficient and inefficient branches are stable even against a large-amplitude perturbation makes it even more important to understand the detailed structure of the CRMS solutions. More specifically, understanding the critical parameters which distinguish the regions of single and multiple solutions needs to be clarified for astrophysical applications. For instance, considering realistic time evolution of a SNR shock propagating in the interstellar medium, it may settle either on the inefficient or efficient branches depending on the Mach number, upstream CR fraction, and injection rate. The physics of injection is still a controversial issue and certainly beyond the scope of this chapter. The injection is indeed determined as a result of thermalization involving complicated physics of collisionless shocks. There exist plenty of theoretical and numerical studies of injection processes, which indicates that the injection

processes and/or its efficiencies depend on the orientation of magnetic fields, plasma β, and Mach numbers [e.g., Malkov and Völk, 1995; Sugiyama et al., 2001; Scholer, 1990; Amano and Hoshino, 2010]. The injection not only controls the number of particles accelerated by the shock but also the total energy converted into CRs through nonlinear shock modification, possibly leads to an abrupt "phase transition". This kind of discontinuous transition may occur even for a fixed injection rate because of intrinsic nonlinearity of the modified shock as suggested previously by Malkov and Drury [2001]. Note that the CR production rate at SNR shocks is still uncertain [Helder et al., 2009; Hughes et al., 2000; Fukui, 2013], but both the efficient and the inefficient solutions may in principle applicable at present. Although our limited knowledge of the physics of injection and the maximum energy makes it difficult to state anything conclusive in predicting observational consequences of astrophysical shocks, our results suggest that an actual SNR shock may reside in the inefficient state, so that the CR production rate is lower than previously discussed based on the strongly modified solutions.

Chapter 3

WAVE GENERATION AND DISSIPATION EFFECTS ON THE COSMIC RAY MODIFIED SHOCKS IN THE KINETIC MODEL

3.1 Introduction

In two-fluid model, the behavior of CRs is determined by the energy equation of CRs as typically shown in the previous section:

$$\frac{\partial E_c}{\partial t} + \nabla \cdot (\boldsymbol{u} E_c) + p_c(\nabla \cdot \boldsymbol{u}) - \kappa \nabla^2 E_c = -\alpha \nabla \cdot \boldsymbol{u}, \tag{2.4}$$

in the form of the energy density E_c and the pressure of CRs p_c. In this two-fluid model, we cannot discuss the energy spectrum, which can be compared with observations. The next better approximation of the CRs transport equation is the diffusion-convection equation described as

$$\frac{\partial f}{\partial t} + \boldsymbol{u} \cdot \nabla f - \nabla(\kappa \nabla f) = \frac{1}{3}(\nabla \cdot \boldsymbol{u}) p \frac{\partial f}{\partial p} + Q, \tag{3.1}$$

where the source term Q in the last term in the right hand side means the injected particle from background plasma. For the simplicity, we consider the parallel plane shock in the one-dimension (along x coordinate) and assume f is isotropic. Equation (3.1) reduces to

$$\frac{\partial f(x,p)}{\partial t} + u(x)\frac{\partial f(x,p)}{\partial x} - \frac{\partial}{\partial x}\left(\kappa(x,p)\frac{\partial f(x,p)}{\partial x}\right) = \frac{1}{3}\frac{\partial u(x)}{\partial x}p\frac{\partial f(x,p)}{\partial p} + Q(x,p). \tag{3.2}$$

Note that the hydrodynamical values E_c and p_c for CRs are given by taking the averages of $f(x,p)$ over the momentum space:

$$E_c(x) = 4\pi\int_{p_0}^{p_{max}} p^2 T(p) f(x,p)dp = 4\pi mc^2\int_{p_0}^{p_{max}} p^2\left(\sqrt{1+(p/(mc))^2}-1\right)f(x,p)dp, \tag{3.3}$$

$$p_c(x) = \frac{4\pi}{3}\int_{p_0}^{p_{max}} vp^3 f(x,p)dp = \frac{4\pi}{3}mc^2\int_{p_0}^{p_{max}}\left(c\frac{p/(mc)}{\sqrt{1+(p/(mc))^2}}\right)p^3 f(x,p)dp. \tag{3.4}$$

$T(p)$ is the kinetic energy of a particle with momentum p. p_0, p_{max}, m and c are the minimum and maximum momenta of CRs, the mass of the proton and the speed of light, respectively.

As the extension of the two-fluid model, we can consider a system where the kinetic diffusion-convection fir CRs is coupled with the hydrodynamical equations for the background thermal plasma. Such a system can be called as "CR-kinetic" model, because the kinetic behavior of CRs depending the momentum is included, which is neglected in the hydrodynamical approximation.

The theoretical investigations of the diffusion-convection equation coupled with NLDSA (Nonlinear Diffusive Shock Accelerations) began from almost the same time of the two-fluid model [Drury and Völk, 1981]. Blandford [1980] and Heavens [1983] investigated the equation with the background plasma which is almost close to ones of the test-particle limit but slightly modified by CRs. The first study including the more strongly modified case is conducted by Malkov [1997a]. He investigated the steady-state diffusion-convection equation with the Bohm diffusion, where the diffusion coefficient κ is only proportional to the particle momentum p:

$$u(x)\frac{\partial f(x,p)}{\partial x} - \frac{\partial}{\partial x}\left(\kappa(p)\frac{\partial f(x,p)}{\partial x}\right) = \frac{1}{3}\frac{\partial u(x)}{\partial x}p\frac{\partial f(x,p)}{\partial p}, \tag{3.5}$$

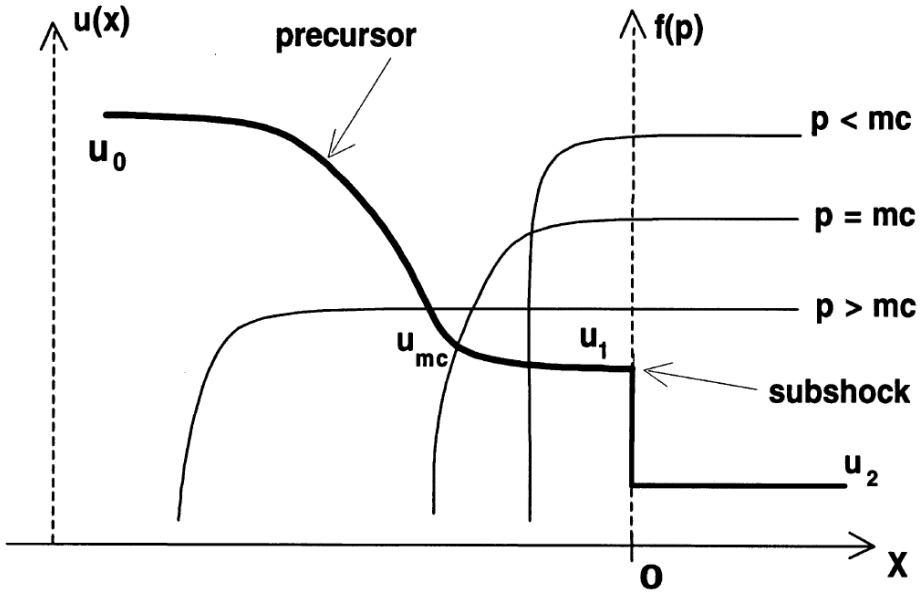

Figure 3.1: A profile of the background plasma flow $u(x)$ and the spatial distribution function of CRs $f(x,p)$ with the different momentum p (from Berezhko and Ellison [1999]). A thick solid line shows $u(x)$ and three thin solid lines show $f(x,p)$ at the low ($p < mc$), middle ($p = mc$) and high ($p > mc$) energy.

where the background plasma flow is smoothly decelerated in the upstream precursor region:

$$u = \begin{cases} u(x), & (x < 0) \quad (3.6) \\ u_2 (= \text{constant}), & (x > 0) \quad (3.7) \end{cases}$$

which is shown in Figure 3.1. The subscripts 0, 1 and 2, each means the value of the far upstream, immediate upstream of subshock and just behind the subshock respectively. In addition, we set the x-coordinate, where subshock is located at $x = 0$ and the region $x < 0$ ($x > 0$) corresponds to the upstream (downstream) region, these settings are used hereafter. Equation (3.5) is coupled with the hydrodynamical mass and momentum flux conservation in the precursor for the (parallel) shock:

$$\rho(x)u(x) = \rho_0 u_0, \quad (3.8)$$

$$\rho(x)u(x)^2 + p_c(x) + p_{g,0}\left(\frac{u_0}{u(x)}\right)^{\gamma_g} = \rho_0 u_0^2 + p_{g,0}. \quad (3.9)$$

The third term of the right hand side of Equation (3.9) means that the background plasma pressure changes adiabatically with the deceleration of the flow. The approximate steady-state solution in the precursor is given following,

$$f(x,p) = f_{sub}(p)\exp\left[\frac{q(p)}{3\kappa(p)}\int_x^0 u(x')dx'\right]. \quad (x<0) \tag{3.10}$$

$f_{sub}(p)$ is the distribution function of CRs at the subshock and $q(p) = \mathrm{d}\ln f_{sub}(p)/\mathrm{d}\ln p$ is the spectrum index of CRs at the subshock. It is noted that in the test-particle limit of NLDSA where there is no background thermal plasma modification by the action of CRs, i.e. $u(x) = V_1(=\text{constant})$ at $x<0$ and $V_2(=\text{constant})$ at $x>0$, the spectrum index $q=4$ ($f_{sub}(p)\propto p^{-4}$), Equation (3.10) reduces to

$$f(x,p) = f_{sub}(p)\exp\left[-\frac{4V_1}{3\kappa(p)}x\right], \quad (x<0) \tag{3.11}$$

which gives the similar profile of $f(x,p)$ in DSA (c.f. Equation (1.29)).

The spectrum index q is the important values showing the acceleration efficiency, and we will show that the spectrum shape is modified by the action of CRs. This effect is not included in two-fluid model. Let us consider the velocity u_p, which is the fluid velocity that CR particles with momentum p feel in the upstream. By the similar analysis to the DSA in Section 1.2, the particle with momentum p, which goes back and forth across the subshock and is reflected by the waves moving with the speed u_p in the upstream and u_2 in the downstream, shows the spectrum index s' (of the power law $N(E)\propto E^{-s'}(\Leftrightarrow N(p)\propto p^{-s'})$),

$$s'(p) = \frac{3u_2}{u_p(p)-u_2}+1. \tag{3.12}$$

From the relations $N(p)dp = 4\pi p^2 f(p)dp$ and $f(p)\propto p^{-q}$,

$$q(p) = -s'(s)-2 = -\frac{3u_2}{u_p(p)-u_2}-3 = -\frac{3u_p(p)}{u_p(p)-u_2} = -\frac{3}{1-u_2/u_p(p)}. \tag{3.13}$$

As illustrated in Figure 3.1, particles with higher momentum p have longer mean free paths. Therefore CRs with higher energies can exist further from the subshock. In the precursor, the velocity of the background plasma u decreases monotonically towards the subshock. It means the velocity $u_p(p)$ increases monotonically with increase of the particle momentum p. Equation (3.13) suggests the index $q(p)$ also increases with p monotonically. In the test-particle limit, $u_p = 4u_2$ for shocks with high Mach and then $q(p) = -4(\text{constant})$. The total compression ratio $R = u_0/u_2$ becomes larger than 4 in NLDSA, so the flatter spectrum than the test-particle limit is seen at high energies. The spectrum index of the low energies CRs, which feel $u_p \sim u_1$ around the subshock, depends on the compression ratio of the subshock $r_s = u_1/u_2$. If the modification of CRs is week and r_s does not change greatly, the q is almost similar to -4. On the other hand, r_s decreases well bellow 4 in the strongly modified regime. In such cases, q is smaller than -4 and the spectrum becomes steeper, leading to the concave spectrum at the whole.

Blasi [2002] derived u_p in the alternative way. He gave the following formula:

$$u_p(p) = u_1 - \frac{1}{f_{sub}(p)} \int_{-\infty}^{0-} f(x,p) \frac{\partial u}{\partial x} dx. \tag{3.14}$$

He also derived the analytical formula of $f_{sub}(p)$:

$$f_{sub}(p) = \frac{3Rr_s}{Rr_sU(p) - 1} \frac{\eta n_0}{4\pi p_0^3} \exp\left[-\int_{p_0}^{p} \frac{dp'}{p'} \frac{3Rr_sU(p')}{Rr_sU(p') - 1} \right]. \tag{3.15}$$

For the derivation of this equation in details, see Appendix B. Equation (3.15) is an analytical solution of the steady-state diffusion-convection equation with the monoenergetic particle injection Q:

$$u\frac{\partial f}{\partial x} - \frac{\partial}{\partial x}\left(\kappa(p) \frac{\partial f}{\partial x} \right) = \frac{1}{3}\left(\frac{\partial u}{\partial x} \right) p \frac{\partial f}{\partial p} + Q(x,p). \tag{3.16}$$

$Q(x,p)$ is given by

$$Q(x,p) = \frac{\eta n_{g1} u_1}{4\pi p_0^2} \delta(p - p_0)\delta(x), \tag{3.17}$$

which means that the mono-energetic particles with the momentum p_0 are injected at the subshock position $x = 0$. η is the parameter determining the ratio of the background plasma injected to the CRs, therefore, $\eta n_{g1} u_1$ means the number flux injected to the CRs across the subshock.

It is noted that the effect of the particle escaping from the shock region plays a key role in the above CR-kinetic system. The maximum momentum p_{max} (or a corresponding to free escaping boundary in the upstream [Caprioli et al., 2010]) which cut-off the higher energies is essentially required to settle the system to the steady-state. As mentioned above, the modification by the CRs flattens the spectra at the higher energies. Without cut-off, such a flattening enhances the population of highest energy CRs, which leads to the increase the CR pressure and consequently drive the stronger modification unlimitedly. The boundary conditions are required to prevent such a positive feedback.

3.2 Nonlinear Diffusive Shock Acceleration with Waves

3.2.1 Basic equations of cosmic ray kinetic model

We consider the one-dimensional cosmic ray modified shock, including the effect of the generation and dissipation of waves. As pointed out for a long time, it is possible that the diffusive flow of CRs toward the upstream can drive the various plasma instabilities in the precursor. Some author suggested the amplitudes of the generated waves are so large compared to the background magnetic fields [e.g. Bell, 2004]. In such situations, we can not dismiss the dynamical feedback of the amplified waves that may have the comparable energy to that of the background plasma, which is suggested by some authors recently [Caprioli et al., 2009; Caprioli, 2012]. When the wave generation and the feedback of them are taken into consideration, we can extend the "classical" model of NLDSA to the one described following basic equations:

$$\frac{\partial \rho}{\partial t} + \frac{\partial}{\partial x}(\rho u) = 0, \tag{3.18}$$

$$\frac{\partial}{\partial t}(\rho u) + \frac{\partial}{\partial x}(\rho u^2 + p_g + p_c + p_w) = 0, \tag{3.19}$$

$$\frac{\partial}{\partial t}\left[\frac{1}{2}\rho u^2 + E_g\right] + \frac{\partial}{\partial x}\left[\frac{1}{2}\rho u^3 + F_g\right] = -u\frac{\partial p_c}{\partial x} - u\frac{\partial p_w}{\partial x} + L - W, \tag{3.20}$$

$$\frac{\partial E_w}{\partial t} + \frac{\partial}{\partial x}\left[(u - v_a)E_w + u p_w\right] = u\frac{\partial p_w}{\partial x} + v_a \frac{\partial p_c}{\partial x} - L, \tag{3.21}$$

$$\frac{\partial f}{\partial t} + (u - v_a)\frac{\partial f}{\partial x} - \frac{\partial}{\partial x}\left(\kappa(x,p)\frac{\partial f}{\partial x}\right) = \frac{1}{3}\left(\frac{\partial}{\partial x}(u - v_a)\right) p \frac{\partial f}{\partial p} + Q(x,p), \tag{3.22}$$

$$Q(x,p) = \frac{\eta n_{g1} u_1}{4\pi p_0^2}\delta(p - p_0)\delta(x), \tag{3.17}$$

$$E_g = \frac{p_g}{\gamma_g - 1}, \tag{3.23}$$

$$E_w = (\delta B)^2/4\pi = p_w/2, \tag{3.24}$$

$$F_g = u(E_g + p_g) = u\frac{\gamma_g p_g}{\gamma_g - 1}, \tag{3.25}$$

ρ, u, p_g, p_c are the density, the velocity of flows and the pressure of the background plasma and CRs, respectively. p_w and v_a are the pressure of waves (magnetic pressure by the perturbation δB) and Alfvén velocity. E_g, E_w and F_g are the energy density of the background plasma and waves and the energy flux of the background plasma, respectively. $Q(x,p)$ is the flux of distribution function injected into CRs from the background plasma, and the corresponding energy loss of the background plasma is expressed by W. L is the energy density by the dissipation of the wave. The specific heat ratio of the background plasma $\gamma_g = 5/3$ and the diffusion is assumed to be Bohm diffusion, where the diffusion coefficient is proportional to the CR momentum p, i.e. $\kappa \propto p$ in this chapter. We note that the momentum p is normalized by mc, which is the product of the proton mass m and the speed of light c. When the particle injection is assumed to be the delta-type injection shown in Equation (3.17), the energy loss term W is calculated,

$$W = \int_{p_0-\varepsilon}^{p_0+\varepsilon} 4\pi p_0^2 T(p_0) Q dp = T(p_0)\eta n_{g1} u_1 \delta(x). \tag{3.26}$$

The convection velocity of the diffusion-convection equation (3.22) is different from the one shown previously,

$$\frac{\partial f}{\partial t} + u\frac{\partial f}{\partial x} - \frac{\partial}{\partial x}\left(\kappa\frac{\partial f}{\partial x}\right) = \frac{1}{3}\frac{\partial u}{\partial x} p \frac{\partial f}{\partial p}, \tag{1.22}$$

which is derived in the approximation where the waves as scattering centers are fixed in the flow. By contrast, the finite velocities of waves are considered in Equation (3.22). The velocity $v_a = B_0/\sqrt{4\pi\rho}$, where B_0 is the strength of the unperturbed magnetic fields, is given because the shear Alfvén waves are assumed as scattering waves. Although, precisely, these scattering waves propagate in two directions ($+x$ and $-x$) relative to the flows [Lerche, 1967; Skilling, 1975a, b], only forward waves (propagating $+x$) are taken into account in this chapter [Dewar, 1970; McKenzie and Völk, 1982].

3.2.2 Wave generation and dissipation

In the precursor region, the diffusive CRs streaming against the background plasma flow may excite some plasma instabilities [Bell, 1978, 2004], because the streaming of CRs can carry the electric current. These instabilities generate the magnetic fields and amplify them to the a few hundred times of the strength of the magnetic fields of ISM in some cases. In the nonlinear stage, these generated magnetic fields possibly grow into turbulence and heat the background plasma by their dissipation. In our model of this chapter, we adopt a simple model of wave generation and transport proposed by McKenzie and Völk [1982]. They derived the equation of the Alfvén waves generated by the resonant instabilities between the background plasma and CRs [Lerche, 1967] with the growth rate $\sigma(k,x)$ (given in Drury [1983]; Amato and Blasi [2006]) :

$$\sigma(k,x) = \frac{4\pi}{3}\frac{v_a(x)}{\varepsilon_w(k,x)}p^4 v\frac{\partial f(x,p)}{\partial x}, \tag{3.27}$$

where $\varepsilon_w(k,x)$ is the energy density of Alfvén waves (resonant with the particles of momentum p) per unit logarithmic bandwidth. The growth of waves is expressed by the above σ,

$$\frac{\partial \varepsilon(k,x)}{\partial t} = 2\sigma(k,x)\varepsilon(k,x). \tag{3.28}$$

The hydrodynamical expression of growth of waves is given by the integral of Equation (3.28) with respect to k as following,

$$\int \frac{\partial \varepsilon(k,x)}{\partial t} dk = 2 \int \sigma(k,x) P(k,x) dk, \tag{3.29}$$

$$\Rightarrow \frac{\partial}{\partial t} \frac{(\delta B)^2}{4\pi} \left(= \frac{\partial E_w}{\partial t} \right) = v_a \frac{\partial p_c}{\partial x}. \tag{3.30}$$

In the transformation from Equation (3.29) to (3.30), we used the relation $(\delta B)^2 = \int \varepsilon dk$ and the definition of p_c (Equation (1.40)). Equation (3.30) means the generation of the energy density occur the precursor region with the gradient of the CR pressure, as illustrated in Section 1.2. The time evolution of the energy density $E_w(x)$ is given by,

$$\frac{\partial E_w}{\partial t} + \frac{\partial}{\partial x}[u_{conv} E_w] = -p_w \frac{\partial u}{\partial x} + v_a \frac{\partial p_c}{\partial x} - L, \tag{3.31}$$

where $u_{conv} = u - v_a$ is the convection velocity of E_w. The fist and third terms of the right hand side mean the work to the background plasma done by the wave pressure and the energy loss, respectively. From Equation (3.31), we can derive Equation (3.21) of the basic equations:

$$\frac{\partial E_w}{\partial t} + \frac{\partial}{\partial x}[(u - v_a) E_w + u p_w] = u \frac{\partial p_w}{\partial x} + v_a \frac{\partial p_c}{\partial x} - L, \tag{3.21}$$

The dissipation term L totally depends on the physical model. In this chapter, we use following simple formula:

$$L = \alpha_h v_a \frac{\partial p_c}{\partial x}, \tag{3.32}$$

which means the ratio α_h $(0 \leq \alpha_h \leq 1)$ of the generated wave energy is converted into heat energy. When $\alpha_h = 0$, there is no dissipation (no heating of the background plasma). Always $p_w = 0$ and all energies generated by the instabilities are converted into the heat flux when $\alpha_h = 1$.

In the limit of $v_a \to 0$, there is no generation of waves according to Equation (3.30). Then, if

$p_w = 0$ at initial, always $p_w = 0$. Therefore, the full set of the basic equations are described by

$$\frac{\partial \rho}{\partial t} + \frac{\partial}{\partial x}(\rho u) = 0, \tag{3.18}$$

$$\frac{\partial}{\partial t}(\rho u) + \frac{\partial}{\partial x}(\rho u^2 + p_g + p_c) = 0, \tag{3.33}$$

$$\frac{\partial}{\partial t}\left[\frac{1}{2}\rho u^2 + E_g\right] + \frac{\partial}{\partial x}\left[\frac{1}{2}\rho u^3 + F_g\right] = -u\frac{\partial p_c}{\partial x} - W, \tag{3.34}$$

$$\frac{\partial f}{\partial t} + u\frac{\partial f}{\partial x} - \frac{\partial}{\partial x}\left(\kappa(x,p)\frac{\partial f}{\partial x}\right) = \frac{1}{3}\frac{\partial u}{\partial x}p\frac{\partial f}{\partial p} + Q(x,p), \tag{3.2}$$

$$Q(x,p) = \frac{\eta n_{g1} u_1}{4\pi p_0^2}\delta(p - p_0)\delta(x), \tag{3.17}$$

$$E_g = \frac{p_g}{\gamma_g - 1}, \tag{3.23}$$

$$F_g = u(E_g + p_g) = u\frac{\gamma_g p_g}{\gamma_g - 1}. \tag{3.25}$$

The above set of equations are well-known formulas in CR-kinetic model used by many authors [e.g. Malkov and Drury, 2001; Blasi, 2002].

3.3 Semi-analytical Method

A direct numerical calculations for the above set of equations is difficult due to two reasons. First, the CR momentum p ranges in the several orders of magnitudes. The diffusion length of CRs defined as $L_{diff} = \kappa/u$ also have the same scales. In order to resolve these diffusion length, we need the numerous spatial grids. Second, the diffusion-convection equation includes the diffusion term which impose a more severe CFL condition, therefore the time needed for the convergence is too large. Some authors who conduct direct simulations avoid these problems by the special techniques saving the number of grids, such as Adoptive mesh refinement (AMR), e.g. Cosmic-Ray Amr SHock (CRASH) code by Kang et al. [2002].

In this study, we focus on the steady-state solutions and use the semi-analytical method proposed by Blasi [2002]; Amato and Blasi [2005]; Reville et al. [2009]. This method is the combination of the analytical steady-state solutions and numerical integrations and repeat the steps until the solutions converge. This procedures finish in the reasonable time, saving the

computational resources. Therefore, we can investigate the behavior of the system easily by the parameter surveys.

3.3.1 Numerical recipe

Our numerical method to obtain the steady-state solutions of the Equations (3.18)-(3.25) is similar to that of Reville et al. [2009] or Caprioli et al. [2009]. Again, the subshock is located at $x = 0$ and the region of $x < 0$ ($x > 0$) is the upstream (downstream) of the subshock and the subscripts 0, 1 and 2 means the value of the far upstream ($x = -\infty$), the upstream of the subshock ($x = 0-$) and the downstream ($x = 0+$). The fixed parameter all through the procedure is far upstream Mach number M_0.

Initial conditions for the calculations

To start iterative procedures, we have to prepare a guess initial conditions. As the guess initial conditions, we set the solutions with $p_w(x) = 0$ in all spatial region. The other parameters $u(x)$, $\rho(x)$, $p_g(x)$ $p_c(x)$ and $f(x,p)$ are determined under the given initial precursor compression ratio $R = u_0/u_1$, which determine the strength of the precursor. It is noted that R changes according to the evolution of the downstream values in the later iterative steps.

The background plasma velocity $u(x)$ is set in order to satisfy the value of $R = u_0/u_1$. In the upstream region, $u(x)$ decrease linearly. The background plasma pressure p_g has the adiabatic profile, $p_g(x) = p_{g,0}(u(x)/u_0)^{-\gamma_g}$. Initial p_c is determined by the conservation of the momentum flux,

$$\rho_0 u_0 u(x) + p_g(x) + p_w(x) + p_c(x) = \rho_0 u_0^2 + p_{g,0}, \tag{3.35}$$

and does not change across the subshock ($p_{c,1} = p_{c,2}$). The other values at downstream of the subshock, ρ_2, u_2, $p_{g,2}$, are determined by the subshock compression ratio $r_s = u_1/u_2$,

$$r_s = \frac{\gamma_g + 1}{\gamma_g - 1 + 2R^{\gamma_g+1} M_0^{-2}}, \tag{3.36}$$

which is derived from the above conservation law (Equation 3.35). r_s depends on the precursor compression ratio R and Mach number at far upstream M_0. The subshock boundary condition $r_s > 1$ gives the limitation to the precursor compression ratio R at an arbitrary Mach number,

$$R < M_0^{\frac{2}{\gamma_g+1}}. \tag{3.37}$$

The CR distribution function $f(x,p)$ has simple power law ($\propto p^4$) at the subshock ($x = 0$), and decrease to the upstream region exponentially. All values at downstream of the subshock are assumed to have the structure with a flat functional behavior, so we focus the structure from far upstream to the just behind of the subshock.

Each iterative step

From given $f(x,p)$ and $u(x)$, we can calculate "modified" $u_p(p)$ by the introduction of waves,

$$u_p(p) = (u_1 - v_{a,1}) - \frac{1}{f_{sub}} \int_{-\infty}^{0-} dx f(x,p) \frac{d}{dx}(u - v_a). \tag{3.38}$$

This $u_p(p)$ enable us to obtain the new f_{sub},

$$f_{sub} = \frac{3R_w r_{s,w}}{R_w r_{s,w} U(p) - 1} \frac{\eta n_0}{4\pi p_0^3} \exp\left[- \int_{p_0}^{p} \frac{dp'}{p'} \frac{3R_w r_{s,w} U(p')}{R_w r_{s,w} U(p') - 1} \right], \tag{3.39}$$

where $U(p) = u_p/u_0$, $R_w = (u_0 - v_{a,0})/(u_1 - v_{a,1})$ and $r_{s,w} = (u_1 - v_{a,1})/(u_2 - v_{a,2})$. For the derivation of Equation (3.39), see Appendix B. The injection parameter η is determined by the following normalization,

$$\frac{4\pi}{3} mc^2 \int_{p_0}^{p_{max}} \frac{p}{\sqrt{1+p^2}} p^3 f_{sub}(p) dp = p_{c,1}. \tag{3.40}$$

$p_{c,1}$ is calculated according to the below set of equations independently,

$$\begin{cases} \rho_0 u_0 u(x) + p_g(x) + p_w(x) + p_c(x) = \rho_0 u_0^2 + p_{g,0}, & (3.35) \\ \dfrac{\partial}{\partial x}\left[(u - v_a)E_w + u p_w\right] = u\dfrac{\partial p_w}{\partial x} + v_a \dfrac{\partial p_c}{\partial x} - \alpha_h v_a \dfrac{\partial p_c}{\partial x}, & (3.41) \\ \dfrac{u\rho^{\gamma_g}}{\gamma_g - 1}\dfrac{\partial}{\partial x}\left(\dfrac{p_g}{\rho^{\gamma_g}}\right) = \alpha_h v_a \dfrac{\partial p_c}{\partial x}. & (3.42) \end{cases}$$

By differentiating the Equation (3.35) and transforming Equation (3.41) and (3.42),

$$\begin{cases} \rho_0 u_0 \dfrac{\partial u}{\partial x} + \dfrac{\partial p_g}{\partial x} + \dfrac{\partial p_w}{\partial x} + \dfrac{\partial p_c}{\partial x} = 0, & (3.43) \\ \dfrac{\partial p_w}{\partial x} = \left[-\left(3\dfrac{\partial u}{\partial x} - 2\dfrac{\partial v_a}{\partial x}\right) p_w + (1 - \alpha_h) v_a \dfrac{\partial p_c}{\partial x} \right] \{2(u - v_a)\}^{-1}, & (3.44) \\ \dfrac{\partial p_g}{\partial x} + \gamma_g \dfrac{p_g}{u}\dfrac{\partial u}{\partial x} = (\gamma_g - 1)\alpha_h \dfrac{v_a}{u}\dfrac{\partial p_c}{\partial x}. & (3.45) \end{cases}$$

Substitution of the Equations (3.44) and (3.45) into the Equation (3.43) and use of the Equation (3.35) lead to

$$A\frac{\partial p_c}{\partial x} + B p_c + C = 0, \tag{3.46}$$

$$A = \left[(\gamma_g - 1)\alpha_h \frac{v_a}{u} + 1 + (1 - \alpha_h)\frac{v_a}{2(u - v_a)} \right], \tag{3.47}$$

$$B = \left[\gamma_g \frac{1}{u}\frac{\partial u}{\partial x} \right], \tag{3.48}$$

$$C = \left[\rho_0 u_0 - \frac{\gamma_g}{u}\left\{ (\rho_0 u_0^2 + p_{g,0}) - \rho_0 u_0 u - p_w \right\} - \frac{3p_w}{2(u - v_a)} \right] \frac{\partial u}{\partial x} + \frac{1}{u - v_a}\frac{\partial v_a}{\partial x} p_w. \tag{3.49}$$

When v_a is constant spatially, Equations (3.46)- (3.49) become

$$A\frac{\partial p_c}{\partial x} + B p_c + C' = 0, \tag{3.50}$$

$$A = \left[(\gamma_g - 1)\alpha_h \frac{v_a}{u} + 1 + (1 - \alpha_h)\frac{v_a}{2(u - v_a)} \right], \tag{3.47}$$

$$B = \left[\gamma_g \frac{1}{u}\frac{\partial u}{\partial x} \right], \tag{3.48}$$

$$C' = \left[\rho_0 u_0 - \frac{\gamma_g}{u}\left\{ (\rho_0 u_0^2 + p_{g,0}) - \rho_0 u_0 u - p_w \right\} - \frac{3p_w}{2(u - v_a)} \right] \frac{\partial u}{\partial x}. \tag{3.51}$$

Above differential equation for $p_c(x)$ depends only on $u(x)$ and $p_w(x)$. $p_{c,1}$ is calculated from the integral of (3.46) from the far upstream to the subshock numerically, from $u(x)$ and $p_w(x)$.

Updated f_{sub} gives the new profile of $f(x,p)$,

$$f(x,p) \simeq f_{sub}(p) \exp\left[\frac{q(p)}{3\kappa(p)}\left(1-\frac{u_2-v_{a,2}}{u_1-v_{a,1}}\right)\int_x^0 (u-v_a)dx'\right]. \tag{3.52}$$

The Equation (3.52) is the approximate solution that is slightly changed by the additional factor from

$$f(x,p) = f_{sub}(p) \exp\left[\frac{q(p)}{3\kappa(p)}\int_x^0 (u-v_a)dx'\right]. \tag{3.53}$$

We can calculate new $p_c(x)$ from updated $f(x,p)$ by the Equation (3.4). p_w is updated by the Equation (3.44) from the new $p_c(x)$ and $u(x)$. The procedure to update $u(x)$ and $p(g)$ is described following. The entropy $p_g\rho^{-\gamma_g}$ is calculated from the numerical iteration according to the Equation (3.42) from p_c. New p_g is solved from this new entropy with fixed ρ. Then, u (and ρ) is updated from the conservation of momentum flux (3.35) from p_g, p_c, p_w. The calculation of $f(x,p)$, p_c, p_w, p_g and u is repeated until the $u(x)$ converges, on each iterative step.

After the profiles of all variables at upstream of subshock is solved, the downstream values are updated. The mechanism of amplification of wave at (sub)shock is controversial matter, so we assume that the p_w is amplified by the factor ξ at subshock. When the compression ratio of p_w is fixed, the other values are determined by the Rankine-Hugoniot relations of the hydrodynamical shock,

$$[\rho u]_{0-}^{0+} = 0, \tag{3.54}$$

$$\left[\rho u^2 + p_g + p_w\right]_{0-}^{0+} = [p_c]_{0-}^{0+} = 0, \tag{3.55}$$

$$\left[\frac{1}{2}\rho u^3 + \frac{\gamma_g p_g}{\gamma_g - 1}u\right]_{0-}^{0+} = -[(3u_2 - 2v_{a,2})\xi p_{w,1} - (3u_1 - 2v_{a,1})p_{w,1}]. \tag{3.56}$$

In the Equation (3.56), the energy flux of particle injection is neglected. From the Equations (3.54) - (3.56), ρ_2, u_2 and $p_{g,2}$ are obtained. These give the new subshock compression ratio r_s

(or $r_{s,w}$), which is needed in the calculation of $f_{sub}(p)$ on the next iterative step. As mentioned above, all variables are updated, then the next steps are repeated in the same way. The steps continues until the injection parameter η converges well. It is noted that in this study the Alfvén velocity v_a is assumed to be spatially uniform, i.e.

$$v_a(x) = \begin{cases} v_{a,0} = v_{a,1} = \sqrt{\dfrac{2}{\beta_0}\dfrac{p_{g,0}}{\rho_0}} & (x < 0), \quad (3.57) \\ v_{a,2} = 0 & (x > 0), \quad (3.58) \end{cases}$$

where β_0 is the far upstream plasma beta. At the precursor region, we only consider the Alfvén waves moving to the upstream (in the direction of the negative x) relative to the background plasma flow. At the subshock, some of these waves are transmitted and others are reflected. All of them are advected to the downstream because we consider the fast shock as the subshock, where both upstream and downstream flow velocities are super-Alfvénic. Therefore, we have to take into account of Alfén waves moving opposite directions (negative and positive x) relative to downstream flow. The reflection ratio of waves at the shocks is the controversial matter, so we treat the effective downstream Alfén velocities $v_{a,2}$ as the zero assuming that the fractions of the opposite propagating waves are roughly equal.

3.4 Steady-state Solutions

3.4.1 Case without wave generation ($v_a = 0$): fiducial case

In the limit of $v_a = 0$, if $p_w = 0$ initially, the basic equations are simplified to the equations excluding the waves, which have been well investigated by many people [Blasi, 2002; Amato and Blasi, 2005; Reville et al., 2009]. Figure 3.2 shows typical steady-state solutions for the parameter of upstream Mach number $M_0 = u_0/C_{s0} = 100$ and the downstream pressure of the background plasma $p_{g,2}/\rho_0 u_0^2 = 0.3$. The energy range of the cosmic rays is assumed to be from $p_0/mc = 1$ to $p_{max}/mc = 1000$. This energy range is fixed throughout this chapter. The minimum momentum p_0 corresponds to the injection energy. The upper three panels are the profiles of

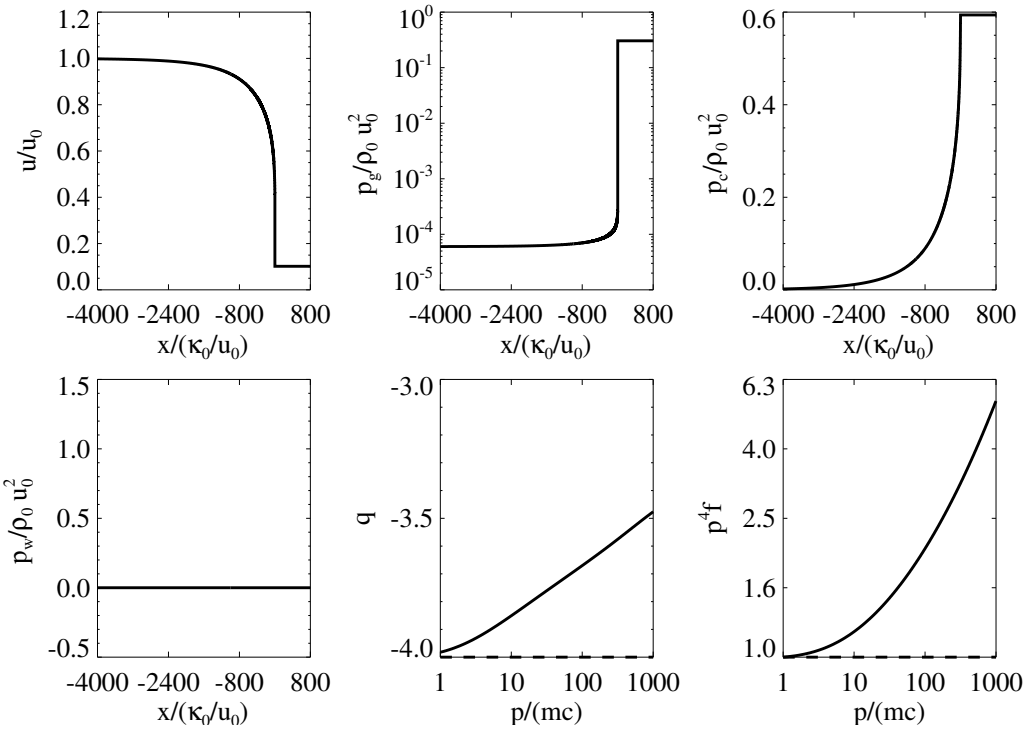

Figure 3.2: Numerical steady-state solutions with $M_0 = 100$, $v_a = 0$ and $p_{g,2}/\rho_0 u_0^2 = 0.3$. Normalized profiles of the background plasma flow velocity, background plasma pressure, CR pressure, (from left in the upper three panels), wave pressure, the spectrum index at the subshock: $q(p) = \mathrm{d}\ln f_{sub}(p)/\mathrm{d}\ln p$, and the profile of $p^4 f_{sub}(p)$ (from left in the lower three panels), respectively. The dashed lines show the theoretical values in the test-particle limit.

the background plasma u, the pressure of the background plasma p_g and the pressure of CRs p_c, which show the similar profiles given in two-fluid model. The precursor compression ratio $R = u_0/u_2 = 2.46$ and the subshock compression ratio $r_s = 3.99$ are obtained. The lower three panels are the profiles of the wave pressure p_w (of course equal to 0), the spectrum index at the subshock $q = \ln f_{sub}(p)/\ln p$ and the normalized spectrum at the subshock $p^4 f_{sub}(p)$ with $p_0^4 f_{sub}(p_0)$. Notice that the normalization unit for the space is the diffusion length κ_0/u_0, where the $\kappa_0 = \kappa(p = p_0)$. In the test-particle limit, the spectrum index is known to be $q = -4(=$ constant) and $p^4 f_{sub}(p) =$ constant. As for the solutions of Figure 3.2, however, the spectrum becomes flatter than the test-particle limit in all momentum range ($q(p) > -4$). The spectrum index q increases monotonically with the momentum p, as mentioned in Section 3.1, from the value of slightly above -4 at the injection momentum p_0 to the maximum value ~ 3.5 at the highest momentum p_{max}, showing the concave spectrum. When there is no wave generation (and dissipation in the precursor region), the entropy of the background plasma is conserved, and

then the pressure of the background plasma changes adiabatically. The compression ratio of the subshock r_s only depends on R and M_0 according to Equation (3.36). The increase of R leads to the decrease of r_s. This means that the stronger modification of CRs causes further deceleration of the background plasma, and the Mach number of the subshock decreases, consequently. Then, the subshock compression ratio becomes weak. In the test-particle limit, i.e. $R = 1$, Equation (3.36) becomes

$$r_s = \frac{\gamma_g + 1}{\gamma_g - 1 + 2M_0^{-2}}, \tag{3.59}$$

which gives the relation between the compression ratio and the Mach number of the hydrodynamical shocks. On the other hand, the increase of M_0 enhances r_s up to the theoretical maximum value of the hydrodynamical shocks ($r_s = 4$). Figure 3.3 shows the spectrum indices $q(p_0)$ and $q(p_{max})$ at the injection momentum p_0 and at the maximum momentum p_{max} as the function of R and the variation of M_0. $q(p_0)$ that represents the acceleration efficiency of the lowest energetic particles can be determined by the subshock compression. Consistent with above qualitative discussion for r_s, $q(p_0)$ are below -4 in the low M_0 or high R, where r_s is smaller than 4. For the case of $M_0 = 10$, $q(p_0) < -4$ almost all R. For $M_0 = 100$, $q(p_0)$ become less than -4 after $R \sim 7$. In the case of $M_0 = 500$, however always $q(p_0) > -4$ regardless of R. The index $q(p_{max})$ at the highest momentum p_{max} reflects the total compression ratio $u_0/u_2 (= Rr_s)$ since the highest energy particles feel the total velocity difference between the far upstream and the downstream of the subshock. The total compression ratio Rr_s is given as follows,

$$Rr_s = \frac{(\gamma_g + 1)R}{\gamma_g - 1 + 2R^{\gamma_g+1}M_0^{-2}}. \tag{3.60}$$

Notice that the above formula can be used only in the case where there is no wave generation (and always $p_w = 0$). Mathematically, above formula has a peak at

$$R^{\gamma_g+1}M_0^{-2} = \frac{2\gamma_g - 1}{\gamma_g} \Leftrightarrow R = \left[\left(\frac{2\gamma_g - 1}{\gamma_g}\right)M_0^2\right]^{\frac{1}{\gamma_g+1}} (\equiv R_c(M_0)). \tag{3.61}$$

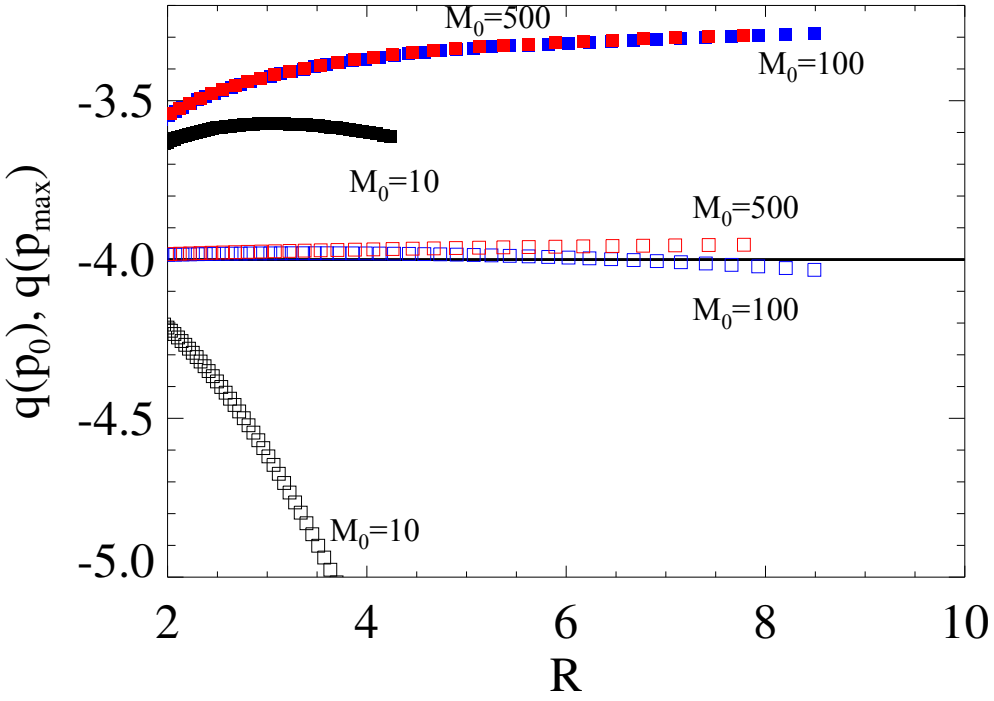

Figure 3.3: The spectrum index $q(p)$ at the injection momentum p_0 and the maximum momentum p_{max} as a function of the precursor compression ratio R. The open squares mean the $q(p_0)$ and filled squares mean $q(p_{max})$. Different colors show the results of different M_0 (black:$M_0 = 10$, blue:$M_0 = 100$ and red:$M_0 = 500$). The horizontal solid line shows the value of the test-particle limit ($q = -4$).

We can predict that p_{max} shows the monotonic increase until around R_c and decrease in $R \gtrsim R_c$. For $M_0 = 10$, 100 and 500, $R_c \sim 3.1$, 17.3 and 57.8, respectively. From the results of $M_0 = 10$ in Figure 3.3, we can see the consistent peak of p_{max} around $R = 3$. This is consistent with the above theory.

Figure 3.4 shows the downstream CR pressure $p_{c,2}$ as a function of the normalized injection parameter ν defined as

$$\nu = \frac{4\pi}{3}\frac{mc^2}{\rho_0 u_0^2} p_0^4 f_{sub}(p_0), \tag{3.62}$$

which was introduced by Malkov et al. [2000]. This parameter means the fraction of the energy density at the injection momentum p_0 given at the subshock, to the total kinetic momentum given at the far upstream. In Figure 3.4, solid line shows the test-particle limit as reference where there is no deceleration of u in the precursor and $r_s = 4$ at the subshock. We can clearly

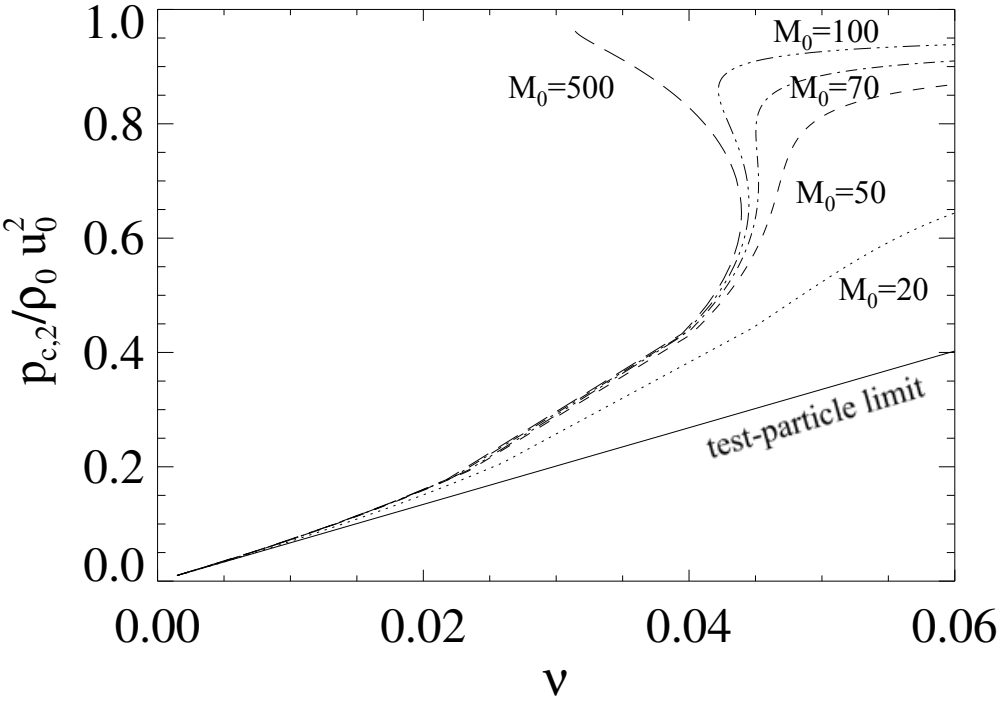

Figure 3.4: Downstream CR pressure p_c as a function of the normalized injection parameter $\nu = (4\pi/3)(mc^2/\rho_0 u_0^2)p_0^4 f_{sub}(p_0)$. Different M_0 is shown with different line types (solid: test-particle limit, dotted: $M_0 = 20$, dashed: $M_0 = 50$, dash-dotted: $M_0 = 70$, dashed triple-dotted: $M_0 = 100$ and long-dashed:$M_0 = 500$).

see the cosmic ray pressures for the nonlinear shocks are strongly modified from the test-particle limit. This figure is qualitatively the same with Figure 2.14(a) of the two-fluid model (Section 2.3) although the definition of the injection parameters in horizontal axes are different each other. It is natural that the CR pressure at the subshock increases with the increasing ν in the steady-states solution, because the particles are injected into the CR component and the population of CRs around the subshock grows. It is noted that there are also three multiple solutions for a given ν, i.e. efficient, intermediate and inefficient solutions in the CR-kinetic model. In the two-fluid model, the multiple solutions disappear and only the single solutions can exist in high Mach regime ($M_0 \gtrsim 10$) [Becker and Kazanas, 2001]. On the other hand, the multiples solutions can be seen over $M_0 \sim 50-70$ and always exist in even higher Mach number [Malkov, 1997b; Malkov et al., 2000]. Notice that in Figure 3.4, the efficient branch of $M_0 = 500$ is partially depicted, because the numerical iterations of our calculation become hard to converge in higher Mach regime where the shock is strongly modified.

3.4.2 Case of wave generation without dissipation ($v_a \neq 0$ & $\alpha_h = 0$)

Without the constraint of $v_a = 0$, the waves are generated in precursor. They exert the wave pressure to the background plasma and heat the background plasma by wave dissipation. In order to distinguish the effect of wave pressure and heating, we consider the most extreme cases where the dissipation is prohibited ($\alpha_h = 0$) and all wave energies are converted into heat ($\alpha_h = 1$). Let us first study $\alpha_h = 0$, where no energy transfer from the generated waves to the heating of the background plasma exists. We only take into account of the modification by the additional wave pressure p_w. Figure 3.5 shows the steady-state solutions with $M_0 = 100$, $v_{a,0}/u_0 = 1.1 \times 10^{-2}$ (plasma beta at far upstream $\beta_0 = 1$), and the compression ratio of the wave pressure across the subshock $\xi = 10$, which is in the same format with Figure 3.2. For the comparison of the different cases, we choose the data that show the almost the same downstream background plasma pressure ($p_{g,2}/\rho_0 u_0^2 \simeq 0.3$). The compression ratios are $R = 2.00$ for the precursor and $r_s = 3.85$ for the subshock, both decrease from those neglecting the wave generation in Figure 3.2. That means the wave pressure weakens the precursor, the subshock, and the total compression of CRMS. The pressures of the generated waves are $p_{w,1}/\rho_0 u_0^2 = 6.8 \times 10^{-3}$ at the upstream of subshock and $p_{w,2}/\rho_0 u_0^2 = \xi\, p_{w,1}/\rho_0 u_0^2 = 6.8 \times 10^{-2}$ at the downstream, which gives $\delta B_2/B_0 = 33.6$. As for the spectrum, the decrease of all of r_s, R and Rr_s leads to the decline of the spectrum index q from that in Figure 3.2. Besides them, $q(p_0)$ is even below -4. As the result, the shape of spectrum becomes steeper in all energies, especially steeper than the test-particle limit in lower energies.

Figure 3.6 shows four energy densities at the upstream of the subshock as the function of the injection parameter ν when $M_0 = 100$. Let us compare this result with the case without waves ($v_a = 0$). Three solid lines show the case of no wave, while four symbols of diamonds are the case of wave generation for the parameters of $v_a/u_0 = 1.1 \times 10^{-2}, \alpha_h = 0, \xi = 10$, for the kinetic $E_{k,1}$ (green), thermal $E_{g,1}$ (orange), CR $E_{c,1}$ (purple) and wave $E_{w,1}$ (brown), respectively. In both cases, CR energy densities (purple lines and diamonds) enter into the strongly modified (efficient) shock regime with the increase of ν, because of the increase of injected energies at the subshock. The higher energies of CRs (equivalently, the higher CR pressure) produce the

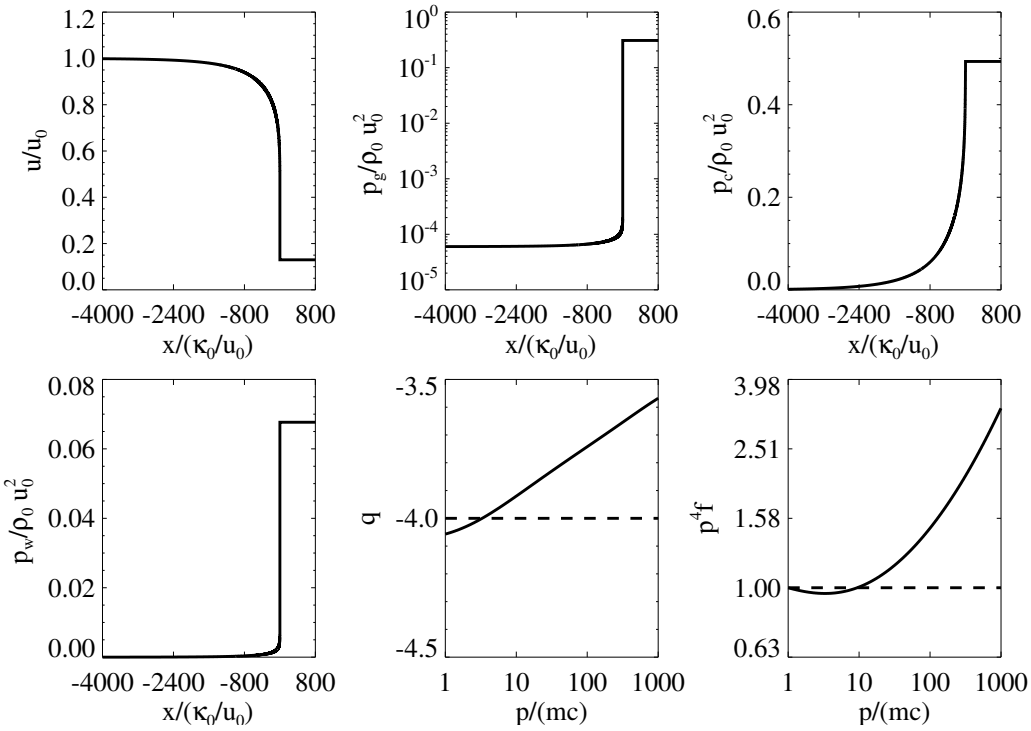

Figure 3.5: Numerical steady-state solutions with $M_0 = 100$, $\alpha_h = 0$ and $p_{g,2}/\rho_0 u_0^2 = 0.3$. The format is the same as Figure 3.2.

steeper pressure gradient structure of CRs in the precursor. By setting $v_a \neq 0$, this possibly leads to stronger generation of waves (brown diamonds) according to the energy equation of waves (3.21). By the excitation of wave pressure, the CR energies (purple diamonds) decrease compared to the case without wave generation (purple solid line). Therefore, the effect of the deceleration of incoming plasma flow is weakened (green diamonds), and leads to the increase of the kinetic energy compared to the case without wave generation (green solid line). Thermal energies (orange diamonds) is smaller than the case without wave (orange solid line). This is simply due to the pressure balance with the generated wave pressure.

The decrease of the CR pressure mentioned above is shown explicitly in Figure 3.7 in the linear scale. The solid line is the results of $M_0 = 100$ in the case without waves, which is also shown in Figure 3.4 as the dashed triple-dotted line. The blue diamonds show the results of the case with waves (the parameters are the same as those of Figure 3.6). The CR pressures with the feedback from the Alfvénic wave appear below the solid line, and the rates of reduction are typically 60% of the efficient branch of the case without waves. More interestingly, the multiple

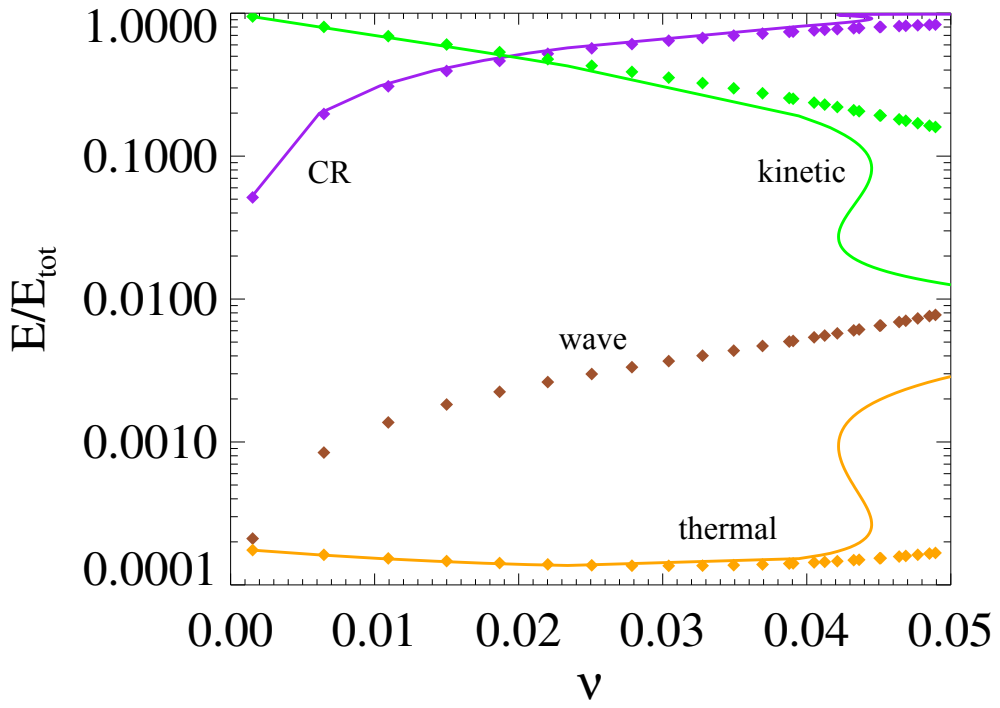

Figure 3.6: Energy density at the upstream of subshock as a function of the normalized injection parameter $\nu = (4\pi/3)(mc^2/\rho_0 u_0^2)p_0^4 f_{sub}(p_0)$ with $M_0 = 100$. The solid lines show the results of $v_a = 0$ and diamonds show the results of $v_{a,0}/u_0 = 1.1 \times 10^{-2}$ ($\beta_0 = 1$), $\alpha_h = 0$ and $\xi = 10$. Each color shows the different kind of energy density (green: kinetic energy of the background plasma $E_{k,1} = \rho_1 u_1^2/2$, orange: thermal energy of background plasma $E_{g,1} = p_{g,1}/(\gamma_g - 1)$, purple: CR energy $E_{c,1} = 4\pi \int_{p_0}^{p_{max}} p^2 T(p_0) f_{sub}(p) dp$, brown: wave energy $E_{w,1} = 2p_{w,1}$).

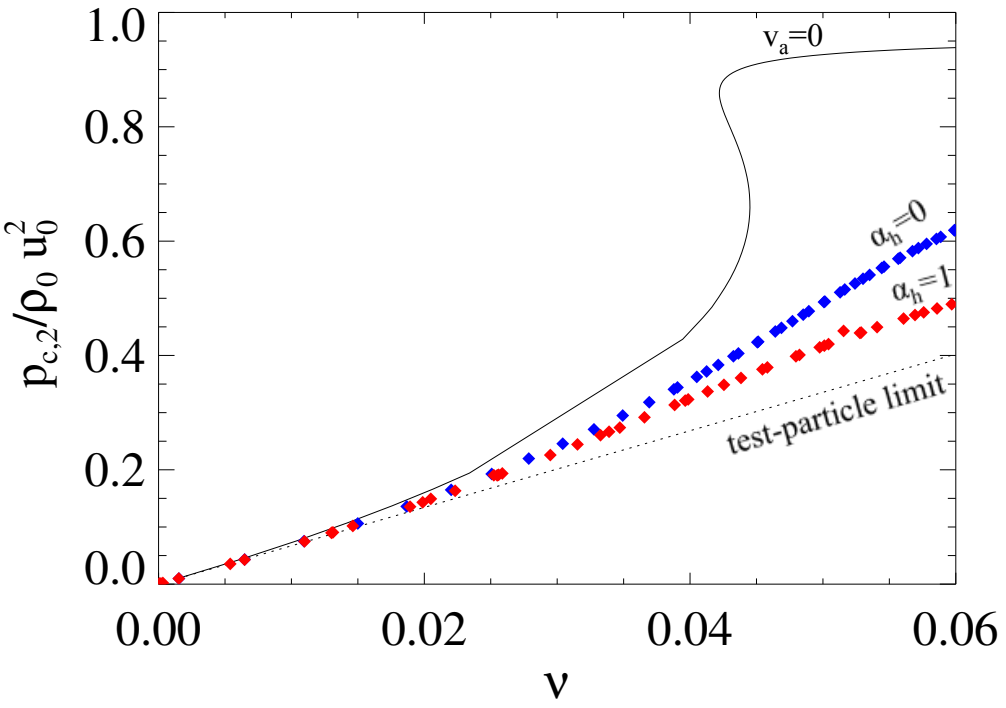

Figure 3.7: Downstream CR pressure p_c as a function of the normalized injection parameter $\nu = (4\pi/3)(mc^2/\rho_0 u_0^2)p_0^4 f_{sub}(p_0)$ with $M_0 = 100$. The solid lines show the results of $v_a = 0$ and dotted line shows test-particle limit. The blue diamonds show the results of $v_{a,0}/u_0 = 1.1 \times 10^{-2}$ ($\beta_0 = 1$), $\alpha_h = 0$ and $\xi = 10$. The red diamonds show the results of $v_{a,0}/u_0 = 1.1 \times 10^{-2}$ ($\beta_0 = 1$), $\alpha_h = 1$.

solutions disappear in $0.042 \lesssim \nu \lesssim 0.045$ and behaviors of the solution for $\alpha_h = 0$ is close to the test-particle limit (dotted line).

When the waves are excited by the CR streaming instability, the CR energies are converted into the wave energies. As the results, the CR pressure in the precursor decreases and the precursor compression ratio becomes weak. This is shown by the blue diamonds in the Figure 3.8, which is the same format with Figure 3.7. Compared with the solid line (the results of the case without waves), the blue diamonds (the results with waves) show the precursor compression ratio $R(= u_0/u_1)$ becomes much lower especially in the efficient branches (in the regime of large ν). The weak precursor compression leads to the increase (decrease) of u_1 (ρ_1), and the decrease of $p_{g,1}$, because the background plasma is compressed adiabatically in the precursor: $p_g(x) = p_{g,0}(u(x)/u_0)^{-\gamma_g}$. The Mach number of the subshock M_1 defied following,

$$M_1 = \frac{u_1}{\sqrt{\gamma_g p_{g,1}/\rho_1}} = \sqrt{\frac{\rho_0 u_0}{\gamma_g}\frac{u_1}{p_{g,1}}}, \tag{3.63}$$

also increases due to the larger u_1 and the smaller $p_{g,1}$ (blue diamonds in Figure 3.9). Figures 3.10 and 3.11 show the subshock compression ratio $r_s(=u_1/u_2)$ and the total compression ratio $Rr_s(=u_0/u_2)$ as the functions of normalized injection parameter ν in the same format with Figure 3.7. Although the magnitude relation of r_s between the solid line ($v_a=0$) and the blue diamonds ($\alpha_h=0$) depends on the injection parameter ν, the range of r_s in the case of $\alpha_h=0$ is limited in $3.5<r_s\leq 4$, and there is a significant increase from the solid line ($v_a=0$) at the large ν. This increase is basically due to the compression of waves at the subshock. By the wave pressure, the hydrodynamical RH relations at the subshock is modified. The increase of the degrees of the freedom f_{deg} reduces the effective specific heat ratio for the background plasma γ_g, because γ_g is connected with f_{deg} in the following relation:

$$\gamma_g=\frac{f_{deg}+2}{f_{deg}}. \tag{3.64}$$

The smaller γ_g enhances the compression ratio of the subshock r_s, which depends on γ_g:

$$r_s\sim\frac{\gamma_g+1}{\gamma_g-1}\sim 1+\frac{2}{\gamma_g-1}. \tag{3.65}$$

The total compression ratio that is given by a product of R and r_s shows the same trend as the precursor compression ratio R, which is indicated by blue diamonds in Figure 3.11. By the suppression of the total compression ratio Rr_s, the spectral indices of the higher energy CRs that reflects the total compression ratio become softer typically in the efficient branches, therefore the feedback effect of CRs becomes weaker than the case without waves.

The decline of the downstream CR pressure can also be understood in the respect of the injection. Figure 3.12 shows the injection energy flux:

$$F_{inj}=\nu\frac{\rho_0 u_0^2 T(p_0)}{mc^2 p_0}(u_1-u_2), \tag{3.66}$$

normalized by the thermal flux of the background plasma $F_{th,2}=\gamma_g p_{g,2}u_2/(\gamma_g-1)$ in the downstream. From the comparison between solid line (case without waves) and blue diamonds (case

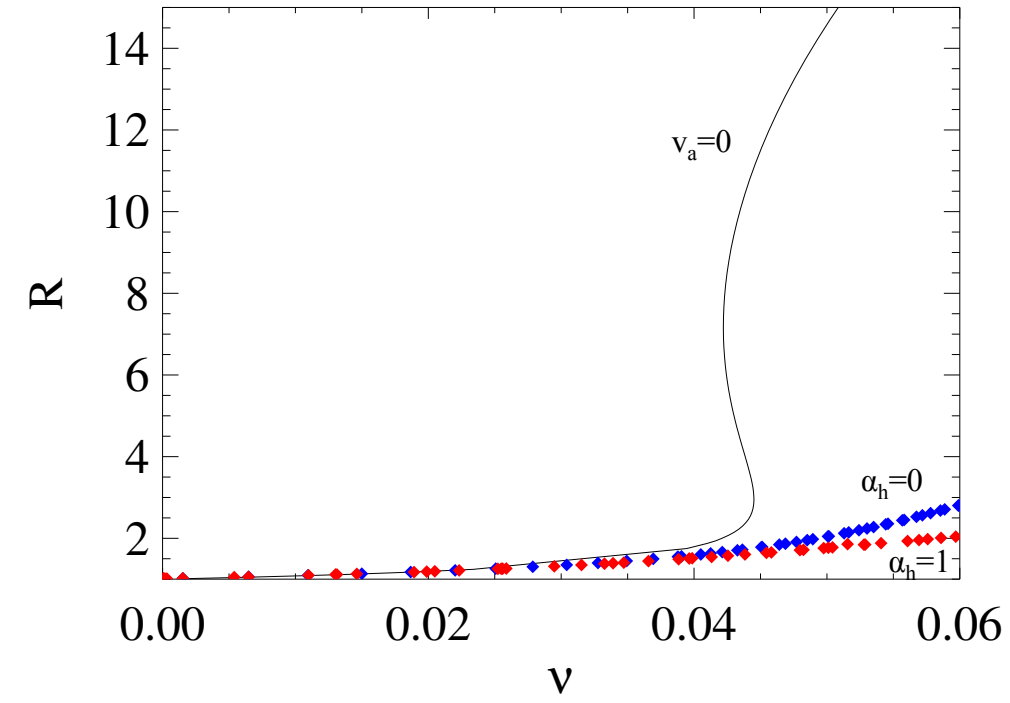

Figure 3.8: Precursor compression ratio $R = u_0/u_1$ as a function of the normalized injection parameter $\nu = (4\pi/3)(mc^2/\rho_0 u_0^2)p_0^4 f_{sub}(p_0)$. The format is the same with Figure 3.7.

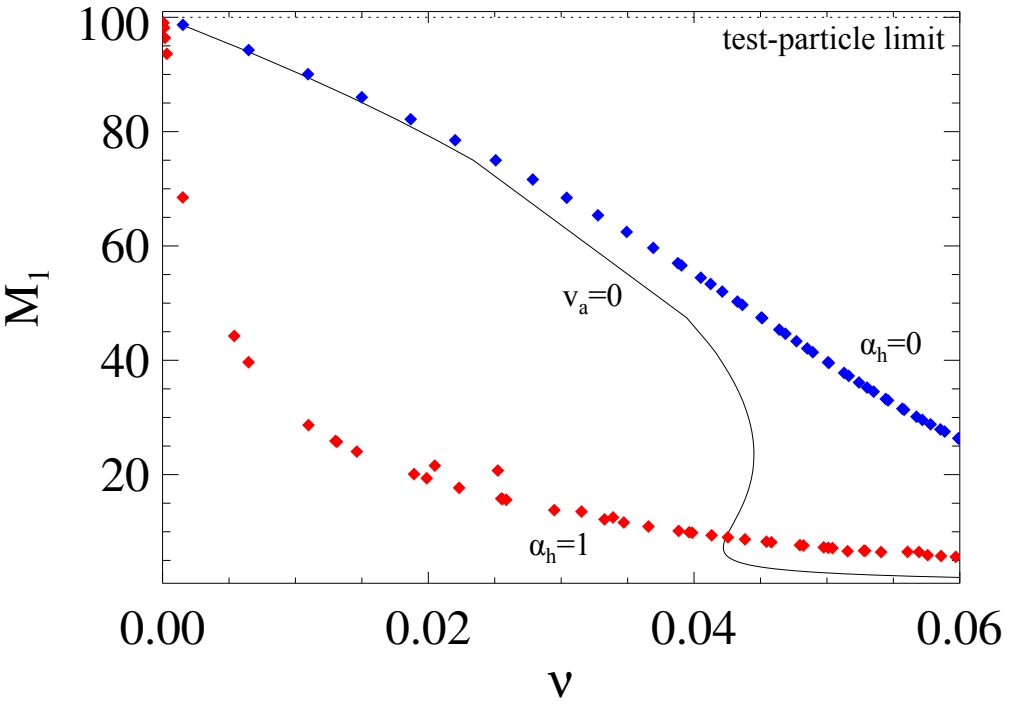

Figure 3.9: Mach number of the subshock M_1 as a function of the normalized injection parameter $\nu = (4\pi/3)(mc^2/\rho_0 u_0^2)p_0^4 f_{sub}(p_0)$. The format is the same with Figure 3.7.

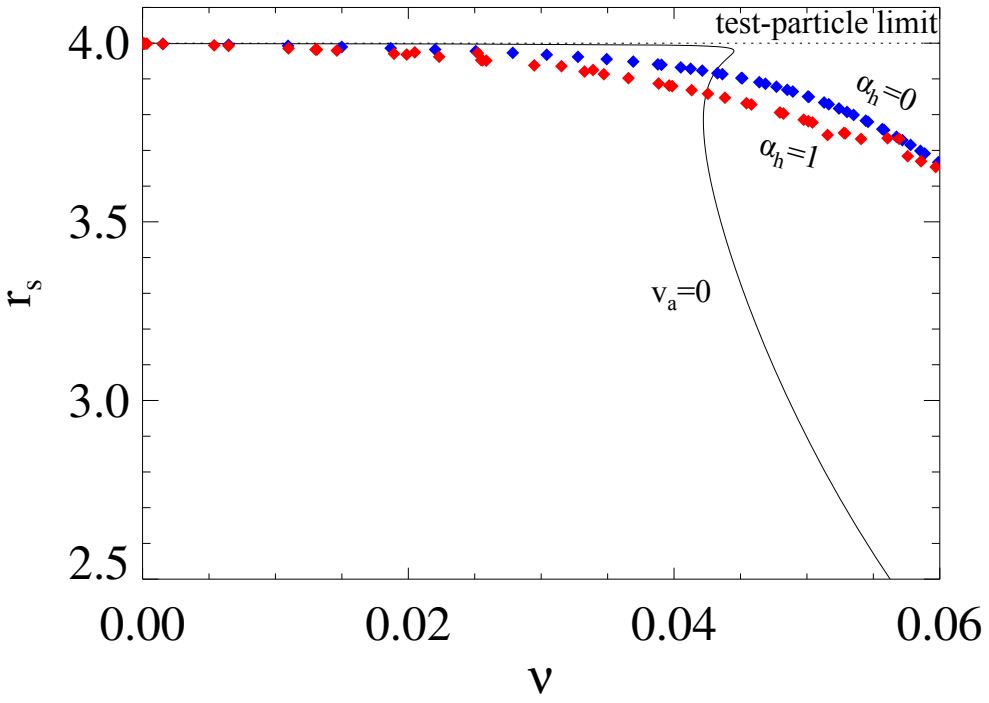

Figure 3.10: Subshock compression ratio $r_s = u_1/u_2$ as a function of the normalized injection parameter $\nu = (4\pi/3)(mc^2/\rho_0 u_0^2)p_0^4 f_{sub}(p_0)$. The format is the same with Figure 3.7.

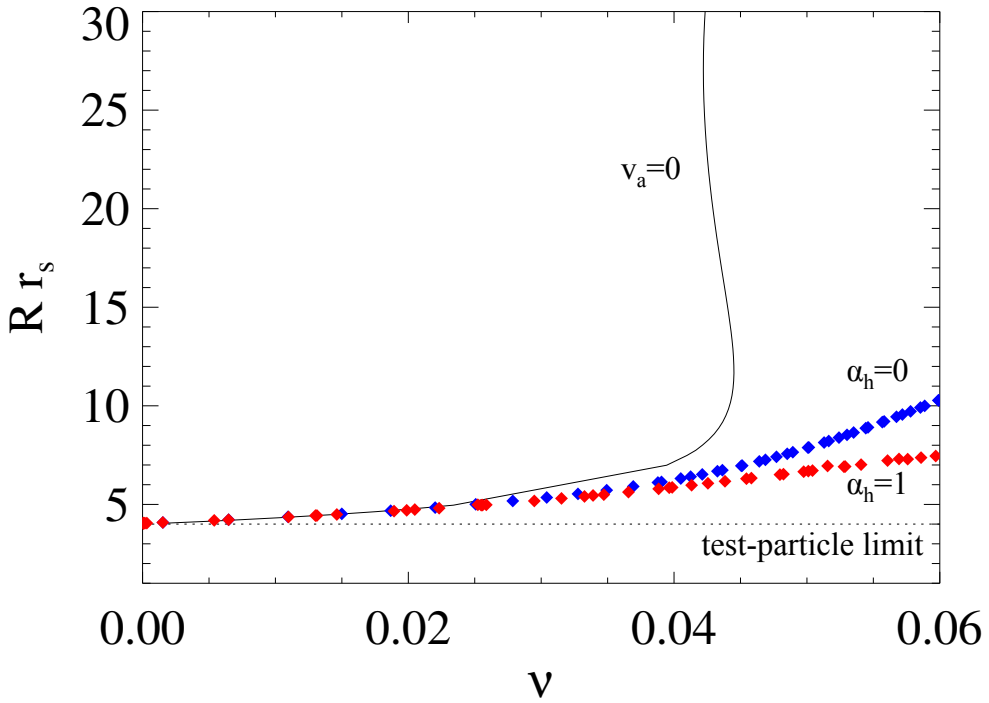

Figure 3.11: Total compression ratio $Rr_s = u_0/u_2$ as a function of the normalized injection parameter $\nu = (4\pi/3)(mc^2/\rho_0 u_0^2)p_0^4 f_{sub}(p_0)$. The format is the same with Figure 3.7.

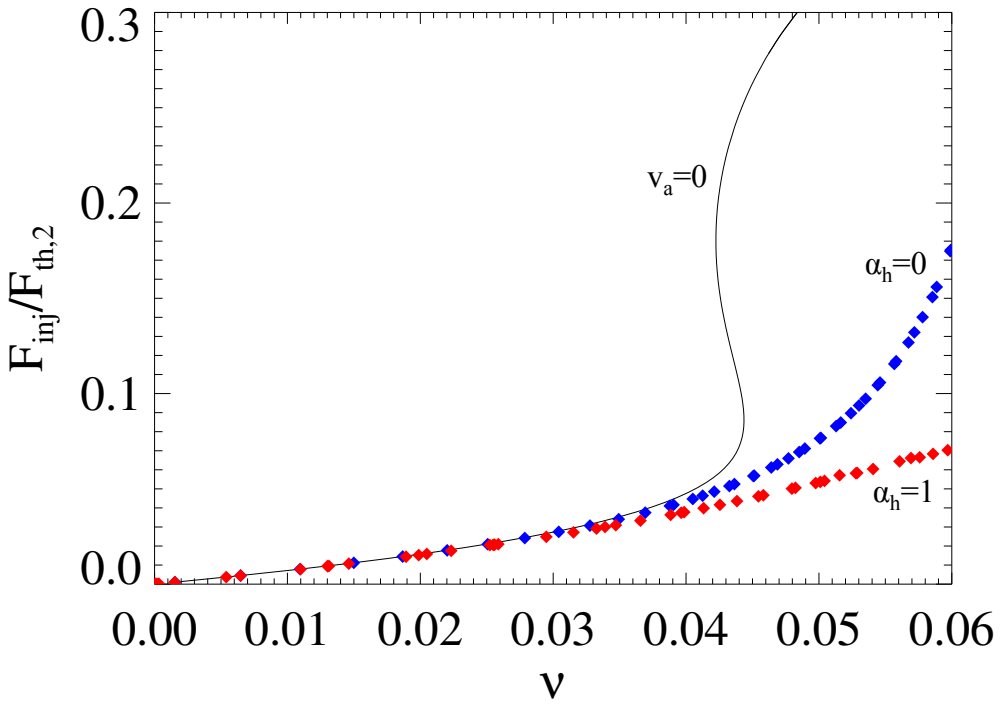

Figure 3.12: The ratio of the energy flux of injected particles $F_{inj} = \nu(\rho_0 u_0^2 T(p_0)/mc^2 p_0)(u_1 - u_2)$ and downstream thermal flux $F_{th,2} = \gamma_g p_{g,2} u_2/(\gamma_g - 1)$, as a function of the normalized injection parameter $\nu = (4\pi/3)(mc^2/\rho_0 u_0^2) p_0^4 f_{sub}(p_0)$ with $M_0 = 100$. The format is the same with Figure 3.7.

with waves), we can see a large suppression of the injection energy flux from the case without wave generation effect of the solid line in the efficient regime. The blue diamonds in Figure 3.13, which indicates the subshock compression ratio r_s as a function of the pressure of the downstream background plasma $p_{g,2}$. Notice that the horizontal axes are different between Figure 3.10 and 3.13. The figure shows the weakening r_s than the solid line when the downstream pressure of the background plasma $p_{g,2}$ is fixed. This weakening of the subshock compression ratio leads to less production of the injection flux from the downstream thermal plasma at the subshock, consequently the CR pressure decreases.

3.4.3 Case of wave energy dissipation ($v_a \neq 0$ & $\alpha_h = 1$)

Let us study the effect if the Alfvénic wave dissipation excited by the cosmic rays. In the case of $\alpha_h = 1$, the energy of the generated waves is totally converted into the heating of the background plasma. As the result, the condition $p_w = 0$ is always satisfied and the modulation by the wave pressure is eliminated. Figure 3.14 shows the shock profiles for $M_0 = 100$, $v_{a,0}/u_0 = 1.1 \times 10^{-2}$

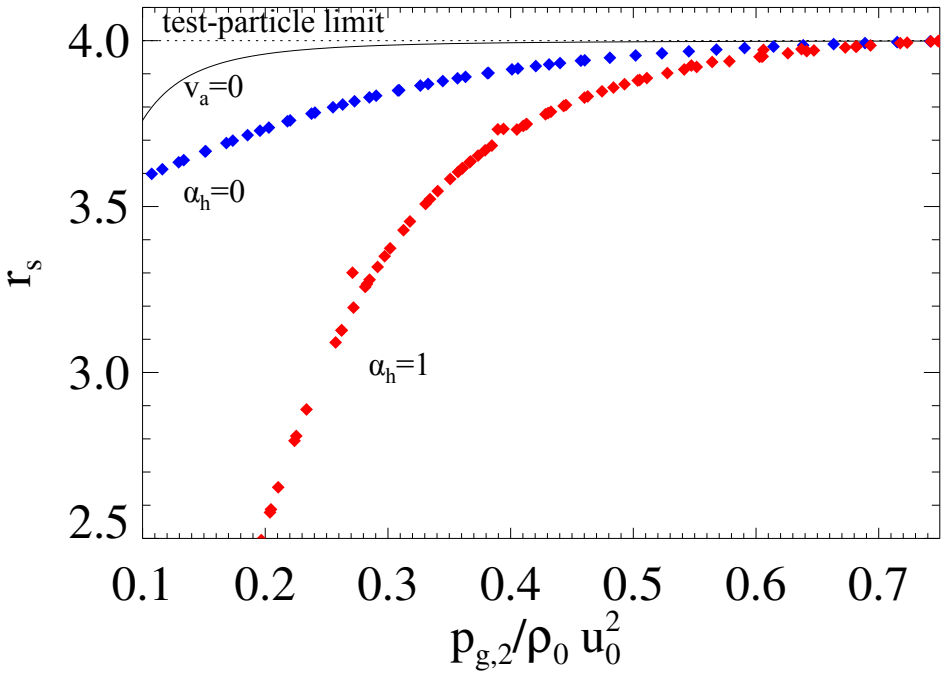

Figure 3.13: The subshock compression ratio r_s as a function of downstream pressure of the background plasma $p_{g,2}$ with $M_0 = 100$. The format is the same with Figure 3.7.

($\beta_0 = 1$) and $p_{g,2}/\rho_0 u_0^2 = 0.3$. The compression ratios for the precursor and the subshock are $R = 2.45$ and $r_s = 3.37$, respectively. The precursor compression ratio R becomes larger than that of $\alpha_h = 0$ ($R = 2.00$) and close to that of $v_a = 0$ ($R = 2.46$). On the other hand, as shown in Figure 3.13, the subshock compression ratio r_s is smaller than both of them ($r_s = 3.85$ in $\alpha_h = 0$ case and $r_s = 3.99$ in $v_a = 0$ case). Therefore the spectrum index at the injection momentum p_0 and the maximum momentum p_{max} become smallest of the three. Then, the spectrum with the wave dissipation effect becomes the softest of the three (but still concave of course).

Figure 3.15 shows the comparison of energy density in the same format as Figure 3.6. The dependence of the injection parameter ν in $M_0 = 100$, is depicted. Most notable behavior is the fact that the thermal energy density of the background plasma increases drastically compared with the $v_a = 0$ case in Figure 3.15. This is the natural consequence because all the generated wave energy (which increase with ν) can be dissipated and the background plasma is simultaneously heated.

As shown by red diamonds in the Figure 3.8, the convert of energies from the CRs to the waves

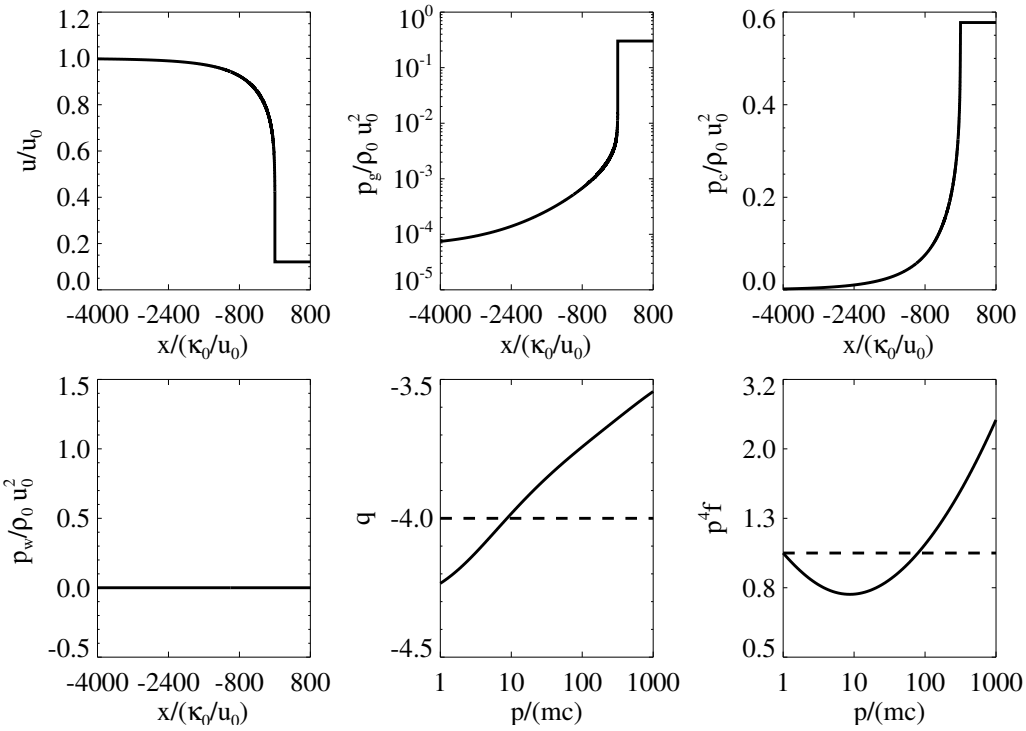

Figure 3.14: Numerical steady-state solutions with $M_0 = 100$, $\alpha_h = 1$ and $p_{g,2}/\rho_0 u_0^2 = 0.3$. The format is the same as Figure 3.2.

(and ultimately, to the background plasma) similarly decreases the precursor compression ratio R. The heating of the background plasma raises up the temperature of it and the sound velocity $C_s = \sqrt{\gamma_g p_g/\rho}$ in the precursor. The larger sound velocity directly leads to the decrease of the Mach number of the subshock M_1, as shown by the red diamonds in Figure 3.9. Although M_1 is almost the same order between the case of $v_a = 0$ and $\alpha_h = 0$ (solid line and blue diamonds), M_1 in the case of $\alpha_h = 0$ (red diamonds) is suppressed by one-fifth at most. From the comparison of r_s between the blue ($\alpha_h = 0$) and red ($\alpha_h = 1$) diamonds in Figure 3.10, the red diamond shows the slight decline from the blue, not only because M_1 becomes smaller, but also because the compression of the waves at the subshock is eliminated. The resulting total compression ratio Rr_s is even lower than that of the case of $\alpha_h = 0$ (as shown in Figure 3.11), and this suppresses the CR production further.

The smaller M_1 is consistent with the larger decrease in the subshock compression ratio r_s (the red diamonds in Figure 3.13, which is the comparison in the fixed downstream gas pressure $p_{g,2}$), ultimately the larger decrease of the injection flux and CR pressure is realized (the red

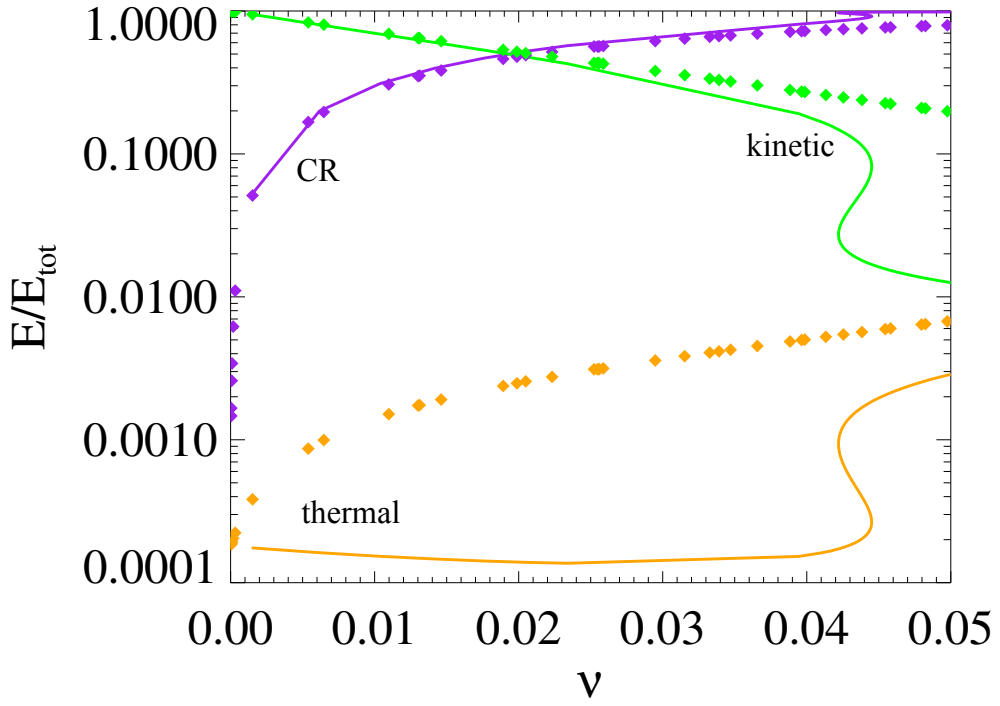

Figure 3.15: Energy density at the upstream of subshock as a function of the normalized injection parameter $\nu = (4\pi/3)(mc^2/\rho_0 u_0^2) p_0^4 f_{sub}(p_0)$ with $M_0 = 100$. The solid lines show the results of $v_a = 0$ and diamonds show the results of $v_{a,0}/u_0 = 1.1 \times 10^{-2}$ ($\beta_0 = 1$), $\alpha_h = 1$ and $\xi = 10$. Each color shows the different kind of energy density (green: kinetic energy of the background plasma $E_{k,1}$, orange: thermal energy of background plasma $E_{g,1}$, purple: CR energy $E_{c,1}$).

diamonds in Figures 3.12 and 3.7). From the studies about two cases of $\alpha_h = 0$ and $\alpha_h = 1$, we can conclude that the excitation of waves reduces the CR production efficiency by the weakening of the total compression ratio. In addition, the heating of the gas by the wave dissipation in the precursor region reduces further the CR production efficiency.

3.4.4 Case with general α_h

In Section 3.4.1 and Section 3.4.2, we consider two special situations where the dissipation does not occur ($\alpha_h = 0$) and all generated wave energies are dissipated ($\alpha_h = 1$) in order to consider separately the effects of the pressure and heating. In this section, we study the effect of the wave energy dissipation as the function of $\alpha_h (0 < \alpha_h < 1)$. Figure 3.16 shows the dependence of four different momentum fluxes at the upstream of the subshock (green: ram pressure $\rho_1 u_1^2$, orange: the background plasma pressure $p_{g,1}$, purple: CR pressure $p_{c,1}$, brown: wave pressure $p_{w,1}$) for the case of the injection parameter $\nu \simeq 0.55$, and $M_0 = 100$, $v_{a,0}/u_0 = 1.1 \times 10^{-2} (\beta_0 = 1)$ and $\xi = 10$, which are the same as the previous parameter survey. As one can see, with increasing α_h, the fraction of the gas pressure increases, while the wave pressure decreases monotonically, and the equipartition is realized at $\alpha_h \simeq 0.4$. The CR pressure shows the monotonic decrease with increasing α_h, while the ram pressure of the background plasma increases. The maximum wave pressure occurs at $\alpha_h = 0$ and the normalized wave pressure becomes $p_{w,1}/\rho_0 u_0^2 \simeq 0.01$ (equal to $\delta B_1/B_0 \simeq 12.4$). Even in the higher Mach number and the larger injection parameter (not shown here), we confirmed that the maximum values of $p_{w,1}/\rho_0 u_0^2$ are in the same order of magnitude, which provide the limit of the generation of wave in our model.

3.4.5 Effect of the variation of ξ and v_a

In our calculations, the compression parameter for the wave pressure ξ is an arbitrary parameter. The downstream wave pressure is assumed to be ξ times of the upstream value, i.e. $p_{w,2} = \xi p_{w,1}$. In our parameter surveys described above, we have adopted $\xi = 10$ for the wave compression at the subshock. Although the compression of the Alfvén wave at the shock is still controversial matter, Caprioli et al. [2009] estimated the compression ratio for the waves

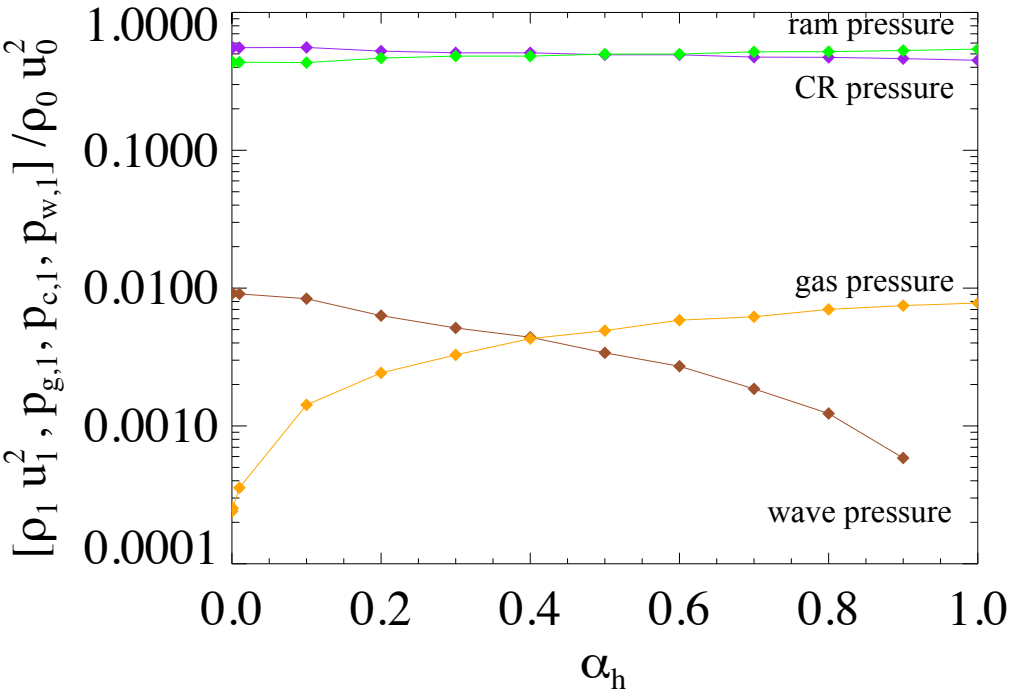

Figure 3.16: Normalized upstream momentum fluxes: $\rho_1 u_1^2$, $p_{g,1}$, $p_{c,1}$ and $p_{w,1}$ as a function of α_h, for the case of $\nu \simeq 0.55$, $M_0 = 100$, $v_{a,0}/u_0 = 1.1 \times 10^{-2} (\beta_0 = 1)$ and $\xi = 10$. Each color shows the different kind of momentum fluxes (green: kinetic momentum of the background plasma $\rho_1 u_1^2$, orange: pressure of the background plasma $p_{g,1}$, purple: CR pressure $p_{c,1}$, brown: wave pressure $p_{w,1}$).

as $p_{w,2} = r_s^2 p_{w,1}$ from the formula derived by McKenzie and Westphal [1969] in the "test-wave" model, where waves injected from the upstream only reflect and transmit at the shocks and the shock structures are not modified by the waves pressure. Their estimation gives the amplification for the wave pressure i.e. $p_{w,2} = 16 p_{w,1}$ in the test particle limit ($r_s = 4$). On the other hand, Vainio and Schlickeiser [1999] calculated the compression ratio at the parallel shocks modified by wave pressure, and estimated the compression ratio as the values less than 10, when the plasma beta is order of unity. Hence, out treatment of the subshock compression ratio for the wave pressure ($\xi = 10$) is more or less reasonable.

Dependence of the wave compression ξ is shown in the upper panel of Figure 3.17. In the upper panel, the dotted and solid lines show the results of the case without waves ($v_a = 0$) and the test-particle limit, respectively. Five colored diamonds show $\xi = 5$ (blue), 10 (red), 15 (green), 20 (orange), 50 (purple), respectively. When ξ is greater than $\xi = 15$, the downstream cosmic rays have the multiple solutions for a given injection parameter ν. When $\xi = 15$ (green

diamonds) that is close to the limit proposed by Caprioli et al. [2009], the solutions close to the solid line (cases without waves). For even larger $\xi(\geq 20)$, the solutions shift leftward in the plot and the region where the multiple solutions exist become wider, although these extreme solutions are unlikely to exist. When $\xi < 10$, the behavior of the multiple solutions disappears. Notice that the upper efficient branches for $\xi > 10$ is not shown, because the numerical convergence is poor.

From the jump condition at the subshock:

$$\left[\rho u^2 + p_g + p_w\right]_{0-}^{0+} = [p_c]_{0-}^{0+} = 0, \tag{3.55}$$

we can derive following relation:

$$\rho_0 u_0 [u]_{0-}^{0+} + [p_g]_{0-}^{0+} + [p_w]_{0-}^{0+} = 0. \tag{3.67}$$

The above relation means that the kinetic energy density is converted to the thermal and wave energy densities at the subshock. The larger ξ (larger $[p_w]_{0-}^{0+}$) weakens the background plasma pressure jump $[p_g]_{0-}^{0+}$. The decrease of the downstream gas pressure $p_{g,2}$ leads to the decline of the downstream gas temperature $T_2(\propto \sqrt{p_{g,2}/\rho_2})$, and the weak gas compression at the shock means the effective adiabatic index of the background plasma γ_g become lower. Since the compression ratio of the hydrodynamical shocks r_s depends on the γ_g as follows,

$$r_s \sim \frac{\gamma_g + 1}{\gamma_g - 1} \sim 1 + \frac{2}{\gamma_g - 1}, \tag{3.65}$$

the lower γ_g enhances the shock compression ratio. As the results, larger ξ increases the subshock compression ratio r_s, and the downstream CR pressure $p_{c,2}$ also increases due to the larger total compression ratio Rr_s.

However, these increases of the CR pressure by the larger ξ is suppressed when the finite dissipation is taken into account ($\alpha_h \neq 0$). The lower panel of Figure 3.17 shows the results of $\alpha_h = 0.9$. We find the dependence of ξ is very weak. This is because the heating of the background

plasma due to the dissipation of the wave energies drastically decreases the Mach number of the subshock M_1, and the subshock compression ratio r_s from those of $\alpha_h = 0$. Furthermore, the wave pressure at the upstream of the subshock $p_{w,1}$ is suppressed approximately by one-tenth because of the dissipation of waves, so the downstream wave pressure $p_{w,2}$ is not enough large to decrease the downstream gas pressure $p_{g,2}$ efficiently. Therefore, the influence of the change of ξ becomes very small.

Another important point may be the effect of the propagation of the Alfvén wave against the background medium. Alfvén velocity v_a determines the convection velocities of CRs and waves, and the growth rate in the generation of waves. For astrophysical high Mach number ($M_0 > 100$) shocks such as SNR shocks, the contribution of the finite Alfvén velocities to the background convection velocity is negligible ($v_a \ll u$). The increase of the growth rate of Alfvén waves, however, leads to the higher wave pressures. Figures 3.18 show the dependence of Alfvén velocities v_a that defined by the far upstream plasma beta β_0. The results in the upper panel are obtained under the condition of $M_0 = 500$, $\alpha_h = 0$ and $\xi = 10$. The solid and dotted lines are the same as Figure 3.17, and the red diamonds for $\beta_0 = 1$ are the same as the red diamonds of the upper panel of Figure 3.17. Note that the typical plasma beta for the ambient ISM that corresponds to the upstream region of shocks is order of unity. For a given parameter ν, the CR pressure increases with increasing β_0. Also in these cases, the dissipation of wave energies decrease the downstream CR pressure as shown in the lower panel of Figure 3.18, where $\alpha_h = 0.9$.

3.5 Summary and Discussion

In this chapter, we have studied the generalized NLDSA where, both the waves generated by the CRs streaming instabilities and the energy density of generated waves are taken into account. In such a case, the dynamical wave pressure in addition to the CR pressure affects the background plasma in precursor and the downstream of the subshock, which leads to the modification of "standard" CRMS without consideration of waves. By our own semi-analytical theory, we can reveal the steady-states of the NLDSA affected by waves with the reasonable computer resources. We conduct parameter surveys and investigate the behaviors of the shocks mediated not only

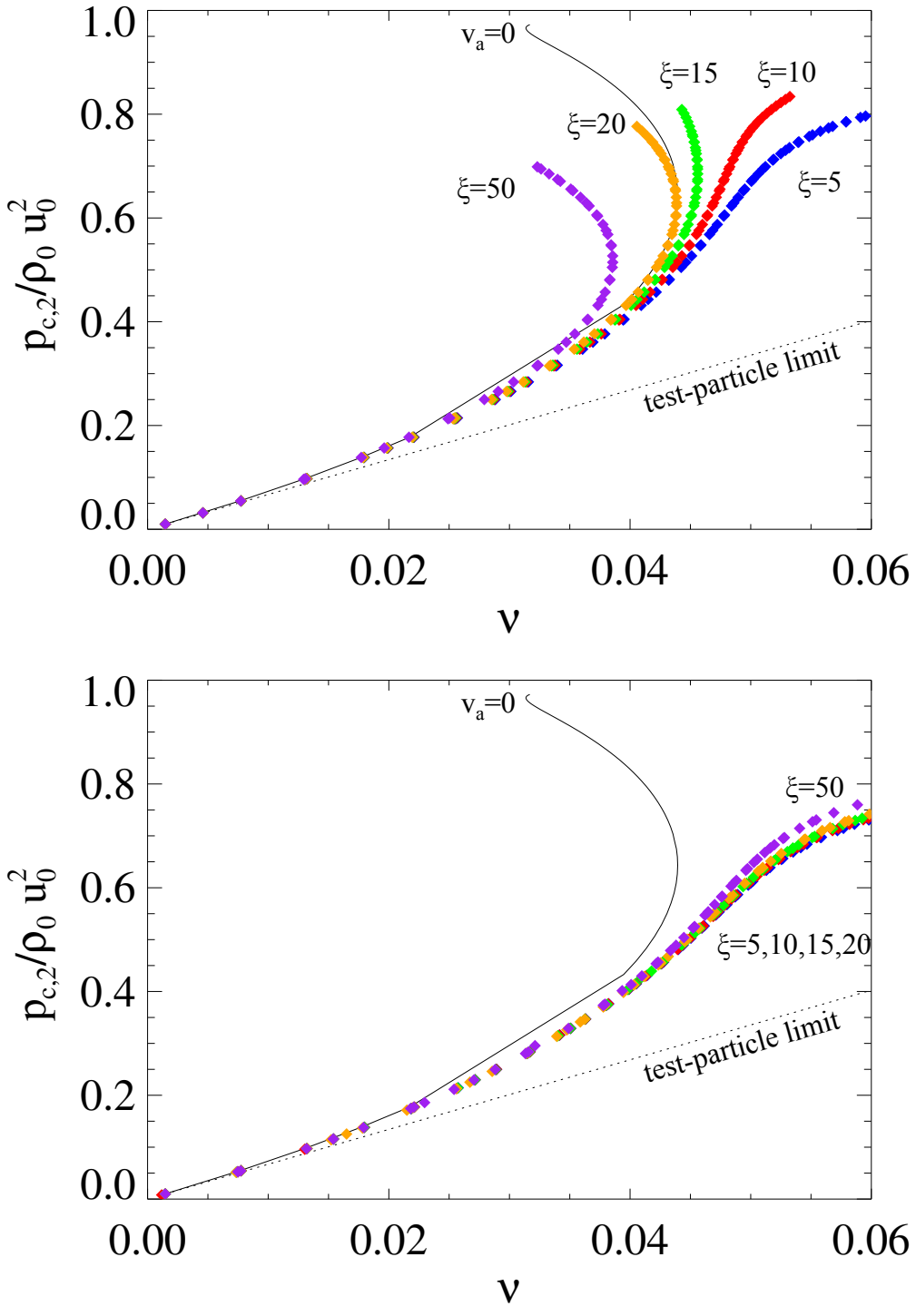

Figure 3.17: Dependence of the wave compression ξ (blue: $\xi = 5$, red:10, green:15, orange:20, purple:50). Upper: downstream CR pressure p_c as a function of the normalized injection parameter $\nu = (4\pi/3)(mc^2/\rho_0 u_0^2) p_0^4 f_{sub}(p_0)$ of $M_0 = 500$, $v_a/u_0 = 2.0 \times 10^{-3} (\beta_0 = 1)$ and $\alpha_h = 0$. The solid line and dotted line indicate the results of the case without waves ($v_a = 0$) and the test-particle limit. Lower: the same format and the same parameters other than $\alpha_h = 0.9$.

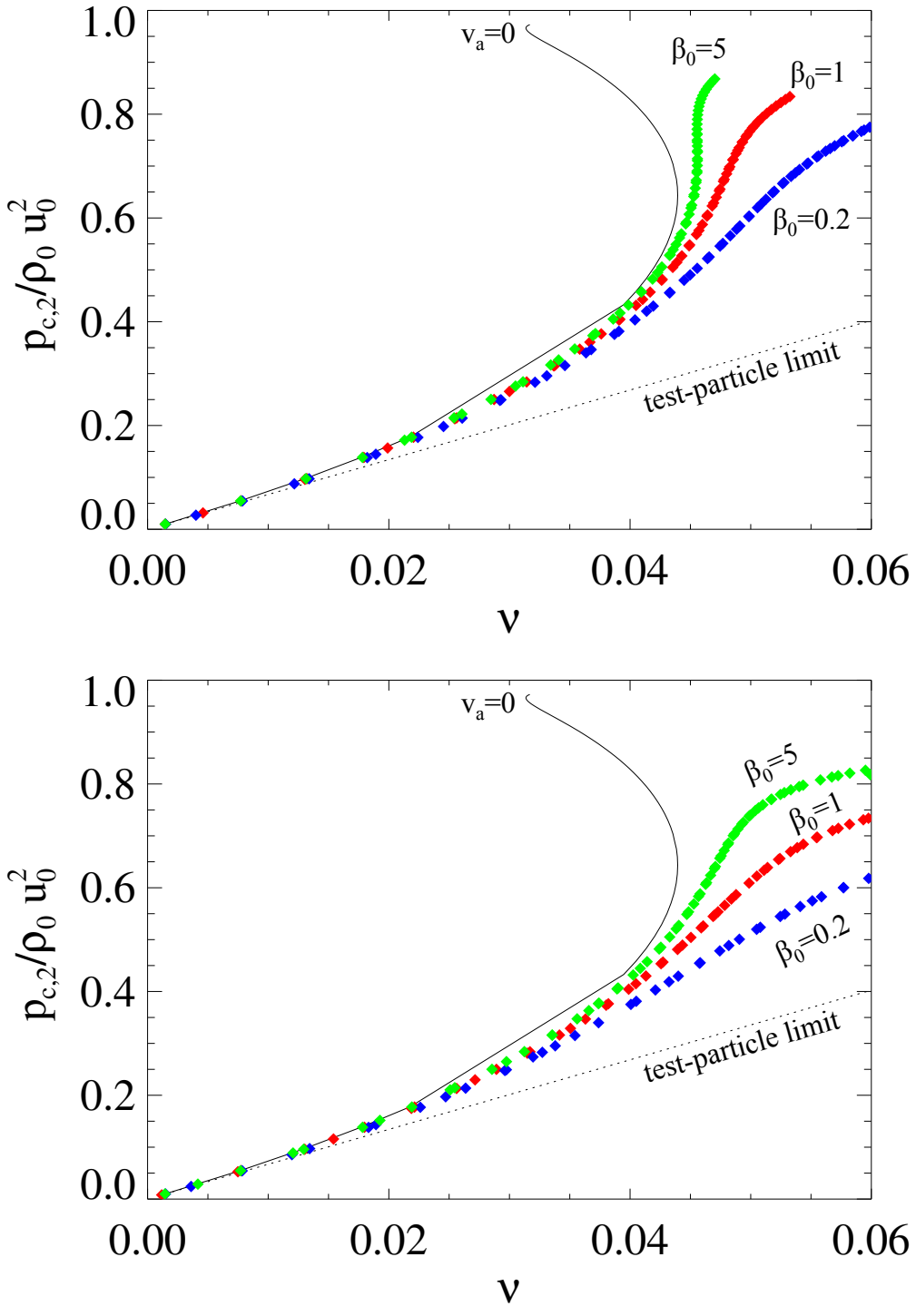

Figure 3.18: Dependence of the Alfvén velocities v_a (plasma beta β_0) (blue: $\beta_0 = 0.2$, red:1, green:5). Upper: downstream CR pressure p_c as a function of the normalized injection parameter $\nu = (4\pi/3)(mc^2/\rho_0 u_0^2)p_0^4 f_{sub}(p_0)$ of $M_0 = 500$, $\xi = 10$ and $\alpha_h = 0$. The solid line and dotted line indicate the results of the case without waves ($v_a = 0$) and the test-particle limit. Lower: the same format and the same parameters other than $\alpha_h = 0.9$.

by the CRs but also by the waves. Our results of this chapter can be summarized as follows.

First and most important point is that the downstream CR pressure effectively decreases by the effect of the Alfvénic waves. This suggests that the standard argument such that the CR production efficiency is enhanced in the framework of NLDSA should be carefully discussed. This is because the additional wave pressure decrease the total compression ratio of the shock. The weakening of CR production efficiency are also associated with the steepening of the CR spectrum index especially in the high energy range.

Second, the dissipation of waves energy suppresses the CR production. In the course of the wave energy dissipation, the background plasma in precursor is heated, and the sound velocities in precursor also rises. This leads to the sufficient decrease of Mach number of the subshock, and as the result, the subshock compression ratio is further reduced. A large CR pressure can be realized for the ideal case without any wave dissipation, but a careful treatment by taking into account of the wave dissipation effect is necessary.

Third, the CR production efficiency is not sensitive to the upstream Mach number, the compression ratio of wave pressure at the subshock, Alfvén velocity and the injection parameter of CRs. In the limit of higher Mach number, or larger wave compression at the subshock, or smaller Alfvén velocities, or larger CR injection efficiency, our results converge to the case where there is no dynamical feedback from the waves. It is natural because the effect of waves becomes relatively less in such regimes. However, even in such regimes, these are definitely non-negligible.

In our study, the dissipation model is very simple one, where a certain ratio of generated wave energies always dissipate independent from the any wave parameter such as wavelength of each amplitude of waves, which is a very ideal assumption. Therefore, the dependency of the dissipation can possibly change from monotonic dependency shown by our results, when another dissipation model is applied. However, our results show that the decline of CR production is observed in the extreme case where there is no dissipation. It means our most important results suggesting the less efficient CR production are independent of dissipation model.

Our kinetic model does not consider the pre-existing CRs in the far upstream region that corresponds to ISM, i.e. $p_{c,0} = 0$. Hence the conservation of the momentum flux is written as

$\rho_0 u_0^2 + p_{g,0} = \rho u^2 + p_g + p_w + p_c$ in our calculations. In the two-fluid model, when the fraction of far upstream (pre-existing) CRs increases, subshocks disappear and the upstream and downstream flows are smoothly (adiabatically) connected, and ultimately, total compression ratio becomes maximum (7). On the other hand, in the kinetic model, such a smooth transition without the subshock is prohibited. This is because the particle injection mainly occurs at the subshock. The situation of the larger fraction of pre-existing CRs qualitatively corresponds to the situation of the stronger particle injection in the kinetic model, since more injected CRs at the subshocks enhance the precursor compression ratio. In such a situation, the Mach number of the subshock becomes less than 1, and the subshock can not exist physically. We eliminate these solutions in our parameter surveys, and choose the relatively low injection parameter ($\nu \lesssim 0.1$). Furthermore, in the actual situations of ISM, the CR pressure is roughly equal to the gas pressure ($p_{c,0} \simeq p_{g,0}$). Even if the pre-existing CRs are considered, the effect of them can be neglected because the kinetic energy density is sufficiently large ($\rho_0 u_0^2 \gg p_{g,0} \sim p_{c,0}$) in the high Mach number shocks like SNR shocks.

We chose the momentum boundary and the CRs whose momentum are above p_{max} escape from the system. In the real SNR shocks, the high energy CRs escape from upstream region because of their larger mean free path than the length scale of the confinement by the self-generated waves. The momentum boundary is the mimic of such a free-escaping spatial boundary. Our choice of the momentum boundary is mainly due to the simplification of the numerical calculations. Nevertheless, the use of the momentum boundary does not compromise the essential nature of NLDSA. Reville et al. [2009] investigated the behaviors of the steady-state solutions of NLDSA with both of the momentum and free-escaping spatial boundary of CRs in the kinetic model. They argued that the there is no significant difference between them when the spatial free-escaping boundary is located at $x = -L_{esc} = -\kappa(p = p_{max})/u_0$, where the subshock is at $x = 0$. In our study, L_{esc} is equal to $x/(\kappa_0/u_0) = 1000$, when p_{max}/mc and p_0/mc are 1 and 1000, respectively.

Chapter 4

CONCLUDING REMARKS

4.1 Summary and Conclusions

In this thesis, we have studied the behaviors of the cosmic ray modified shocks (CRMSs), which involve the dynamical feedback from the cosmic rays (CRs) in the regime of nonlinear diffusive shock acceleration (NLDSA), by the numerical simulations. It is known that CRMSs can be more compressive due to the additional compression effect induced by the CR pressure, and can lead to be a more efficient accelerator of CRs than those without the modification of CRs, because the efficiency of acceleration is mainly due to the shock compression in the standard theory of DSA. The feedback effect from CRs works as a "positive feedback", because the larger population of CRs around the shocks raises the compression ratio of the shocks, and because eventually it enhances the acceleration of higher energy CRs. However, due to the total energy conservation, the above positive feedback process must be balanced with a negative feedback process. The physics of the negative feedback, however, is not clearly understood so far. Our fundamental motivation was to examine how much the CR feedback effects control the efficiency of acceleration of CRs. For this purpose, we have conducted two different problems described in Chapter 2 and Chapter 3.

In Chapter 2, we adopted the two-fluid model where both of the background plasma and CRs are approximated by fluids. This model is simple but useful to understand the essential behavior of CRMSs. With this model, we revisited the stability of CRMSs mainly involving the

three multiple steady-state solutions, which are generally seen in CRMSs. Among these three solutions (efficient, intermediate and inefficient solutions), we revealed by the nonlinear time evolutions that the efficient and inefficient solutions are stable and the intermediate solution is unstable, which result is robust against any shock parameters such as the Mach numbers, the fractions of CRs, the shock angles and injection parameters. Furthermore, we also found that only the inefficient one is realized by taking into account of the time evolutional effect of CRs. Although this result can be applied only in the regime where the multiple solutions exist, our finding suggested inherent "negative feedback" effect of the CRs production in CRMSs. Additionally, when the finite perturbations are added to the CR pressure, CRMSs evolve not in the physical state where the perturbations are enhanced, but in the state where they are suppressed. This negative-feedback effect also supports the above inefficiency of CRMSs.

In Chapter 3, we extended the previous two-fluid model so as to include the momentum dependent kinetics of CRs. This model is called CR-kinetic model. As suggested by many authors, the diffusive flow of CRs streaming towards the upstream in the precursor region can carry the electric currents and can drive some plasma instabilities. In the efficient case of NLDSA, the CR precursor becomes well-developed, and such plasma instabilities more likely to occur. The observations for the supernova shocks also mention the possibilities of the amplified magnetic fields around the shock regions. Although the Alfvénic wave generation/magnetic field amplification is still controversial, it is theoretically believed that the feedback from the excited (or amplified) waves can regulate the existing NLDSA theory. In order to understand the physical behaviors, we study the effect of the wave generation and dissipation by including their effects into the CR-kinetic model of NLDSA. By using the semi-analytical method, we can obtain the numerical steady-states of our CR-kinetic model including waves. Although our wave generation and dissipation model may be a simplified toy model, our conclusions seem to be robust in terms of the Mach number, the injection parameter, Alfvén velocity and the subshock compression ration of the waves. The important results in the Chapter 3 are summarized in Table 4.1. The "standard" NLDSA (SNLDSA) means the NLDSA theory without considering the generation of the waves and the dissipation. The excitation of waves reduces the precursor

Table 4.1: The magnitude relationships among the test-particle limit, the standard NLDSA (cases without waves), the case with waves ($\alpha_h = 0$) and the case with waves ($\alpha_h = 1$), in the fixed far upstream Mach number M_0. Each row is the precursor compression ratio R, subshock compression ratio r_s, total compression ratio Rr_s, downstream CR pressure $p_{c,2}$, downstream gas pressure $p_{g,2}$, spectral indices at the injection momentum $q(p_0)$ and at the maximum momentum $q(p_{max})$, from the top.

R	test-particle ($=1$) $<$ with waves ($\alpha_h = 1$) $<$ with waves ($\alpha_h = 0$) $<$ SNLDSA
r_s	SNLDSA $\lesssim$ with waves ($\alpha_h = 1$) $\lesssim$ with waves ($\alpha_h = 0$) $\lesssim$ test-particle ($=4$)
Rr_s	test-particle ($=4$) $<$ with waves ($\alpha_h = 1$) $<$ with waves ($\alpha_h = 0$) $<$ SNLDSA
$p_{c,2}$	test-particle $<$ with waves ($\alpha_h = 1$) $<$ with waves ($\alpha_h = 0$) $<$ SNLDSA
$p_{g,2}$	SNLDSA $<$ with waves ($\alpha_h = 0$) $<$ with waves ($\alpha_h = 1$) $<$ test-particle
$q(p_0)$	SNLDSA $\lesssim$ with waves ($\alpha_h = 0$) $\lesssim$ with waves ($\alpha_h = 1$) $\lesssim$ test-particle ($=-4$)
$q_(p_{max})$	test-particle ($=-4$) $<$ with waves ($\alpha_h = 1$) $<$ with waves ($\alpha_h = 0$) $<$ SNLDSA

compression ratio R from that of the SNLDSA in the case with waves ($\alpha_h = 0$), due to the convert of energies from the CRs to the waves, and enhances the subshock compression ratio r_s because of the compression of waves at the subshock. The significant decline of R suppresses the total compression ratio Rr_s from that of the SNLDSA. As the results, the spectral index at the maximum momentum p_{max} becomes softer than the SNLDSA, so the positive feedback of CRs is weakened and the downstream CR pressure $p_{c,2}$ decreases.

The heating of the background plasma in the precursor leads further decline of R from the SNLDSA in the case with waves ($\alpha_h = 1$). The hotter background plasma increases the local sound velocities and reduces the Mach number of the subshock M_1. This results in the decrease of the subshock compression ratio r_s from the case of $\alpha_h = 0$. Therefore, the total compression ratio Rr_s in the case of $\alpha_h = 1$ also becomes smaller and $q(p_{max})$ is softer than the case of $\alpha_h = 0$. Consequently, the downstream CR pressure $p_{c,2}$ shows the further decrease.

Although our wave generation and dissipation model may be a simplified toy model, our conclusions seem to be robust in terms of the Mach number, the injection parameter, Alfvén velocity and the subshock compression ration of the waves. Theoretically, the amplification of the magnetic fields, which is caused by the CR feedback in NLDSA, has the possibility of the enhancement of the maximum attainable energy of the CRs. Therefore, many authors have dealt with the topic for a long time. Our conclusions of this thesis suggests that the strong

magnetic fields do not necessarily give an optimistic answer to the problem.

As for the accelerations of the CR electrons, the observations imply that the amplified strong magnetic fields suppress the generation of CR electrons. For the typical example of RX J1713.7-3946, where the leptonic γ-ray is seems to be dominant, the ratio of the emission power of the synchrotron radiation and IC scattering becomes

$$\frac{P_{sync}}{P_{IC}} \sim (B^2/8\pi)/U_{rad}, \tag{4.1}$$

which only depends on the strength of the magnetic fields if U_{rad} is given. In the case of the CMB photons, $U_{rad} \sim 4 \times 10^{-13}\,\mathrm{erg/cm^3}$, then the ratio is

$$\frac{P_{sync}}{P_{IC}} \sim 9.9 \times 10^{-2} \left(\frac{B}{\mu\mathrm{G}}\right)^2. \tag{4.2}$$

If the B is $B \sim 0.1 - 1\,\mathrm{mG}$, P_{sync}/P_{IC} becomes $P_{sync}/P_{IC} \sim 10^3 - 10^5$, which is much larger than the observational value (~ 10). This is inconsistent with the strong magnetic fields inferred from the thin X-ray filaments or the rapid variability of X-ray hotspots. On the other hands, when the hadronic model is adopted, the estimated CR electron/proton number ratio K_{ep} from the strong magnetic fields was $K_{ep} \sim 10^{-6}$ [Uchiyama et al., 2003], which means the inefficient acceleration of the CR electrons compared with the global value ($K_{ep} \sim 10^{-2}$).

Our results also show the spectra of the CRs become steeper than the test-particle limit at the lower energies. This feature is consistent with the recent γ-ray observations of middle age SNRs, like W44 and IC443. These observations suggest the steeper spectrum around the GeV energies than the test-particle limit, i.e. $N(E) \propto E^{-2}$. This softening cannot be explained by the "standard" NLDSA without consideration of the wave generation, because their concave spectra become harder than the test-particle limit in all energy bands, in the sufficiently high Mach number shocks. Even in the recent γ-ray observations, there is still no clear evidence indicating the acceleration of CR protons up to the knee energies. This detection will be expected in the future observations. Our findings suggest that in such challenges, the more careful treatments in the estimation of the spectrum should be required, because not only the classical DSA, but

also the "standard" NLDSA may not provide the real picture of the parent particle distributions responsible for those emissions.

4.2 Open Issues and Future Works

In our studies of this thesis, one dimensional, plain shocks have been considered. The effect of the spherical topology and the expanding effect of the shock is not included. In the actual situation of SNR shocks, shocks expand spherically towards the ambient ISM medium. On the contrary to the plane shocks, the upstream volume increase with expansion, and the energy density of CRs also decreases. In such cases, the feedback effect from the CRs may not be so significant and shocks may be moderately modified. In addition, the generation of waves might be more or less suppressed due to the reduction of the free energy. The multidimensional effect of the CRMSs is also important. Mond and Drury [1998] theoretically predict that the corrugation of the shock surface occurs on the intermediate branch of the multiple solutions in the two-fluid model. This corrugation may not change the stability features, but might affect the transition time to the inefficient branch.

In our treatment of wave generation, we chose the model proposed by McKenzie and Völk [1982] based on the resonant instabilities. Bell [2004] also proposed the wave amplification by the non-resonant instability. Hence, the wave excitation mechanism due to the plasma instabilities can have various origins. We should re-examine our results in other wave generation models or the combination of them. Nevertheless, the fraction of energy density may be more or less limited in the shock waves of much high Mach number, such as SNR shocks. We can expect that our result is independent of the difference of the detail mechanism of wave generation.

The particle injection process is controversial matter, depending on the kinetic physics of the collisionless shocks. In the CR-kinetic model, we assume that the particle injection occurs only at the subshock. In addition to this, the dissipation of wave energies can drive the extra injection in the precursor due to the heating of the background plasma. This can lead to the increase of the CR energy densities. However, the effect of such an extra injection at the precursor may not affect our results of this thesis, because our results in both of the two-fluid and the CR-kinetic

model are robust against the particle injection.

The excitation and amplification of Alfvénic waves in the precursor lead to the spatial and temporal variation of the diffusion coefficient. Some parameters such as the acceleration time of CRs, the escaping flux from the shock region, and the maximum energy of the accelerated particles depends on the diffusion coefficient. In order to estimate them correctly, we have to adopt more realistic diffusion of CRs, which is totally different from the simple Bohm diffusion.

Appendix A

The multiple solutions with changes of the specific heat ratio of cosmic rays γ_c in the two-fluid model

Figure A.1 shows the downstream CR pressure p_c as a function of far upstream Mach number M for the different specific heat ratio of CR γ_c in the two-fluid model, when the upstream CR pressure ratio $N = p_c/(p_g + p_c) = 0.1$. In the two-fluid model, γ_c is chosen arbitrarily in the range $1 < \gamma_c < \gamma_g (= 5/3)$. When $\gamma_c = 4/3$ (red dots in the figure) that is the assumed value in the simulation studies in Chapter 2, the multiple solutions are seen at the low Mach number ($M \sim 5.5$), and the range where the multiple solutions exist is limited in the narrow parameter space. However, as discussed in Section 2.4, γ_c can decrease from 4/3 when the escape of CRs are taken into account. The decrease of γ_c drastically changes the picture of the steady-state solutions. When $\gamma_c = 1.32$ (blue dots in the figure) that is slightly lower than 4/3, the range where the multiple solutions exist becomes broader ($6 \lesssim M \lesssim 9$ and $13 \lesssim M$). In the results of $\gamma_c = 1.3$ (green dots in the figure), the multiple solutions always exist in $6.5 \lesssim M$. It is noted that the multiples solutions disappear and solutions shift in the left in the figure, when γ_c increase from 4/3 (brown: $\gamma_c = 1.35$, orange: 1.34)

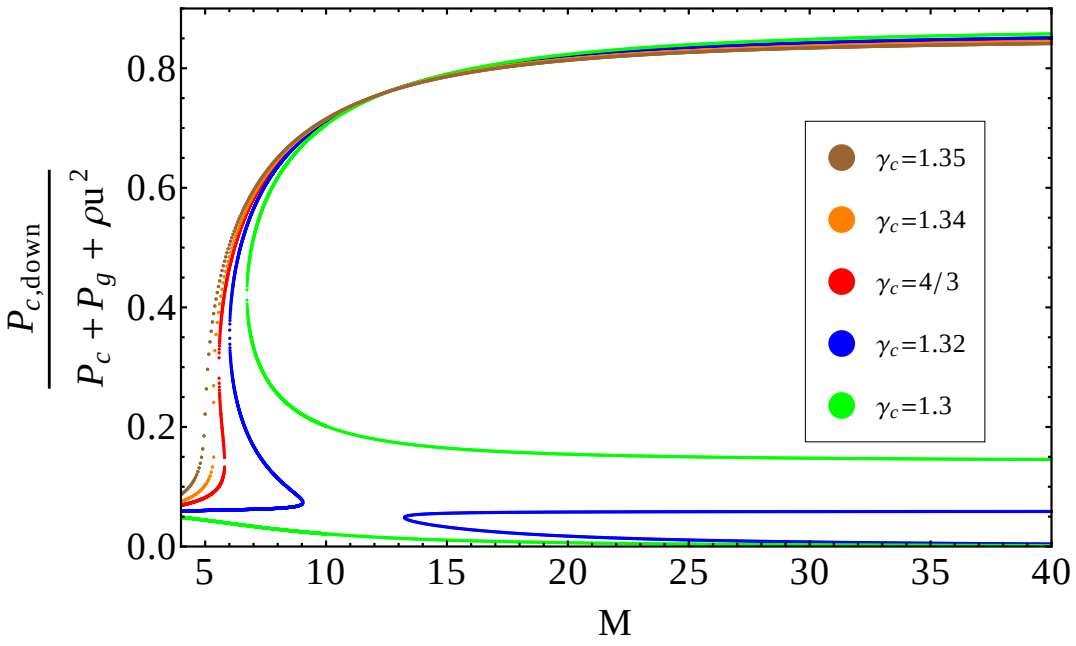

Figure A.1: Downstream CR pressure p_c as a function of the upstream Mach number M. Each dot shows the results of the upstream CR pressure ratio $N = p_c/(p_g + p_c) = 0.1$ and the different specific heat ratio of CRs γ_c (brown: 1.35, orange: 1.34, red: 4/3, blue: 1.32, green: 1.3).

Appendix B

Derivation of f_{sub}

The analytical form of f_{sub},

$$f_{sub} = \frac{3R_w r_{s,w}}{R_w r_{s,w} U(p) - 1} \frac{\eta n_0}{4\pi p_0^3} \exp\left[- \int_{p_0}^{p} \frac{dp'}{p'} \frac{3R_w r_{s,w} U(p')}{R_w r_{s,w} U(p') - 1} \right], \tag{3.39}$$

is derived from the diffusion-convection equation in the steady-state,

$$(u - v_a)\frac{\partial f}{\partial x} - \frac{\partial}{\partial x}\left(\kappa \frac{\partial f}{\partial x}\right) = \frac{1}{3}\left(\frac{\partial}{\partial x}(u - v_a)\right) p \frac{\partial f}{\partial p} + \frac{\eta n_{g1} u_1}{4\pi p_0^2} \delta(p - p_0)\delta(x), \tag{B.1}$$

By taking the integral of the Equation (B.1) from x_0 to $x(< 0^-)$, we can obtain the following,

$$\kappa \frac{\partial f}{\partial x} - (u - v_a) f = \left(\kappa \frac{\partial f}{\partial x}\right)_{x=x_0} - \frac{1}{3p^2} \int_{x_0}^{x} dx' \frac{\partial}{\partial x'}(u - v_a) \frac{\partial}{\partial p}(p^3 f). \tag{B.2}$$

Similarly, the integral of the Equation (B.1) from x_0 to 0^- (just ahead of the subshock) gives,

$$\frac{p}{3}\frac{\partial f_{sub}}{\partial p}(u_1 - v_{a,1} - u_p) = -\left(\kappa \frac{\partial f}{\partial x}\right)_{x=0^-} + \left(\kappa \frac{\partial f}{\partial x}\right)_{x=x_0} + f_{sub}\left[\frac{p}{3}\frac{\partial u_p}{\partial p} + u_p\right], \tag{B.3}$$

where

$$u_p(p) = (u_1 - v_{a,1}) - \frac{1}{f_{sub}} \int_{-\infty}^{0-} dx f \frac{d}{dx}(u - v_a). \tag{3.38}$$

Besides, the integral from 0^- to 0^+ also gives,

$$\kappa\left(\frac{\partial f}{\partial x}\right)_{x=0^-} = \frac{p}{3}\frac{\partial f_{sub}}{\partial p}(u_2-u_1)+\frac{\eta n_{g1}u_1}{4\pi p_0^2}\delta(p-p_0). \tag{B.4}$$

By substituting the Equation (B.4) into the Equation (B.3),

$$\frac{p}{3}\frac{\partial f_{sub}}{\partial p}(u_2-v_{a,2}-u_p) = \left(\kappa\frac{\partial f}{\partial x}\right)_{x=x_0} + f_{sub}\left[\frac{p}{3}\frac{\partial u_p}{\partial p}+u_p\right] - \frac{\eta n_{g1}u_1}{4\pi p_0^2}\delta(p-p_0), \tag{B.5}$$

which is simplified to

$$\frac{\partial f_{sub}}{\partial p}+\frac{3}{p}\frac{1}{u_p-u_2+v_{a,2}}\left[u_p+\frac{p}{3}\frac{\partial u_p}{\partial p}+(u_0-v_{a,0})\left(\kappa\frac{\partial f}{\partial x}\right)_{x=x_0}\right]f_{sub} = \frac{3}{p}\frac{1}{u_p-u_2+v_{a,2}}\frac{\eta n_{g1}u_1}{4\pi p_0^2}\delta(p-p_0). \tag{B.6}$$

This normal differential equation for $f_{sub}(p)$ is easily solved and the general solution is

$$f_{sub} = \frac{3R_w r_{s,w}}{R_w r_{s,w}U(p)-1}\frac{\eta n_0}{4\pi p_0^3}\exp\left[-\int_{p_0}^{p}\frac{dp'}{p'}\frac{3R_w r_{s,w}U(p')}{R_w r_{s,w}U(p')-1}\right]. \tag{3.39}$$

In the limit $v_a \to 0$, Equation (3.39) becomes Equation (3.15) given by Blasi [2002].

Appendix C

Variation of p_{max} in the kinetic model

In Chapter 3, all numerical simulations are conducted with the fixed momentum boundary, i.e. $p_0/mc = 1$ for the minimum (injection) boundary and $p_{max}/mc = 1000$ for the maximum. When the protons are considered as the accelerated particles, these minimum and maximum momenta are approximately equal to the energies of $10^9\,\mathrm{eV}$ and $10^{12}\,\mathrm{eV}$, respectively, because the rest energy of the protons is about $10^9\,\mathrm{eV}$. Figure C.1 shows the dependence of the downstream CR pressure $p_{c,2}$ on the maximum momentum p_{max}. The black solid line is the result of the test-particle limit and four colored solid lines are the results of the cases without waves ($v_a = 0$) and $M_0 = 100$. The diamonds in four colors are the results of the cases with wave generation and the finite dissipation ($\alpha_h = 0.1$). Four colors show $p_{max}/mc = 10^3$ (blue), 10^4 (red), 10^5 (green) and 10^6 (orange). The maximum momentum $p_{max}/mc = 10^6$ is approximately equivalent to the energy of $10^{15}\,\mathrm{eV}$. In the cases without waves (four colored solid lines), the efficient branches become dominant in the parameter space with the increase of p_{max}, and the multiple solutions are seen at the lower injection parameter ν. This is because the positive feedback effect of CRs is enhanced with larger p_{max}. The modification by CRs hardens the spectrum in the higher energies regime, and such hard spectra enhance the CR pressure p_c defined as follows,

$$p_c(x) = \frac{4\pi}{3}\int_{p_0}^{p_{max}} v p^3 f(x,p) dp, \tag{3.4}$$

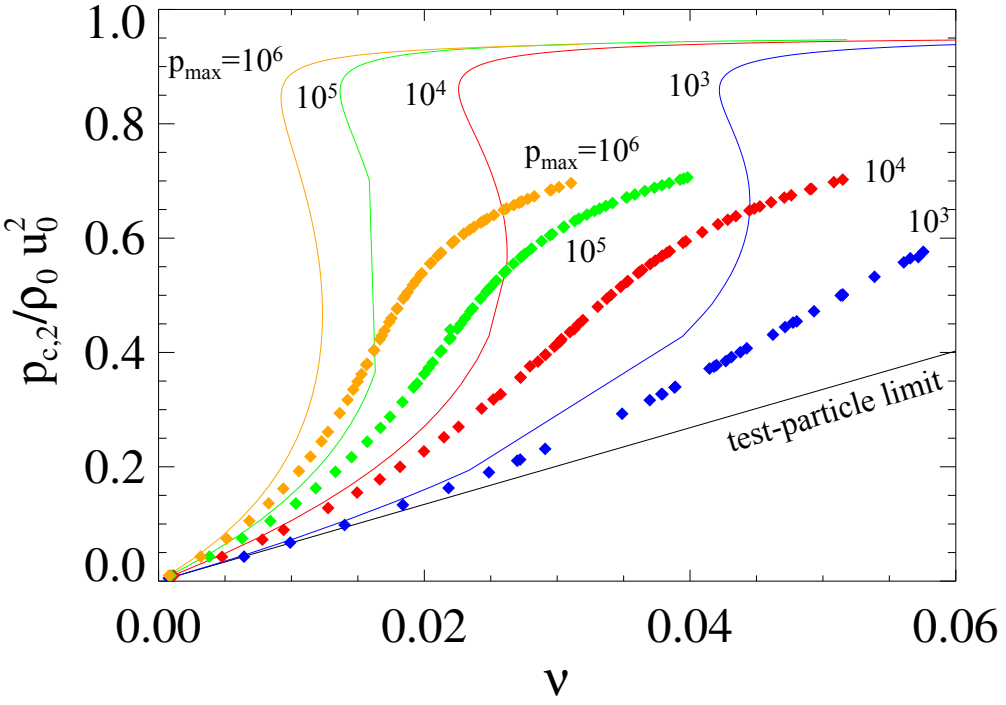

Figure C.1: Downstream CR pressure p_c as a function of the normalized injection parameter $\nu = (4\pi/3)(mc^2/\rho_0 u_0^2)p_0^4 f_{sub}(p_0)$. Each diamond shows the results of $v_{a,0}/u_0 = 1.1 \times 10^{-2}$ ($\beta_0 = 1$), $\alpha_h = 0.1$, $\xi = 10$, $M_0 = 100$ and the different maximum momentum p_{max}/mc (blue: $p_{max}/mc = 10^3$, red: 10^4, green: 10^5, orange: 10^6). Each colored solid line shows the results of $v_a = 0$, $M_0 = 100$ and the different p_{max}/mc (blue: 10^3, red: 10^4, green: 10^5, orange: 10^6). The black line shows the result of the test-particle limit when $p_{max}/mc = 10^3$.

when the integral interval $[p_0, p_{max}]$ becomes larger. The increasing p_c more hardens the spectrum, as the results, the CR production rate becomes efficiently high regardless of the low injection efficiency.

Above positive feedback is weakened by the generation of waves and the dissipation of them (colored diamonds). The CR energies decrease by the generation of waves, and heating of the background plasma in the precursor reduces the precursor compression ratio. As the results, the spectrum in the higher energies, which reflects the total compression ratio, becomes softer than those of the cases without waves. This leads to the suppression of the CR production.

Reference

A. A. Abdo, M. Ackermann, M. Ajello, et al. FERMI-LAT DISCOVERY OF GeV GAMMA-RAY EMISSION FROM THE YOUNG SUPERNOVA REMNANT CASSIOPEIA A. *The Astrophysical Journal Letters*, 710(1):L92–L97, 2010.

A. A. Abdo, M. Ackermann, M. Ajello, et al. Gamma-Ray Emission from the Shell of Supernova Remnant W44 Revealed by the Fermi LAT. *Science*, 327(5969):1103–1106, 2010.

A. A. Abdo, M. Ackermann, M. Ajello, et al. Observation of Supernova Remnant Ic 443 With the Fermi Large Area Telescope. *The Astrophysical Journal*, 712(1):459–468, 2010.

A. A. Abdo, M. Ackermann, M. Ajello, et al. OBSERVATIONS OF THE YOUNG SUPER-NOVA REMNANT RX J1713.73946 WITH THE FERMI LARGE AREA TELESCOPE. *The Astrophysical Journal*, 734(1):28, 2011.

F. Acero, M. Lemoine-Goumard, M. Renaud, et al. Study of TeV shell supernova remnants at gamma-ray energies. *Astronomy & Astrophysics*, 580:A74, 2015.

F. Aharonian, A. G. Akhperjanian, A. R. Bazer ‐ Bachi, et al. A detailed spectral and morphological study of the gamma-ray supernova remnant RX J1713.73946 with HESS. *Astronomy and Astrophysics*, 449(1):223–242, 2006.

F. Aharonian, A. G. Akhperjanian, A. R. Bazer-Bachi, et al. Primary particle acceleration above 100 TeV in the shell-type supernova remnant RX J1713.7-3946 with deep HESS observations. *Astronomy and Astrophysics*, 464:235–243, 2007.

F. A. Aharonian, A. G. Akhperjanian, K.-M. Aye, et al. High-energy particle acceleration in the shell of a supernova remnant. *Nature*, 432(7013):75–77, 2004.

G. E. Allen, J. W. Keohane, E. V. Gotthelf, et al. EVIDENCE OF X-RAY SYNCHROTRON EMISSION FROM ELECTRONS ACCELERATED TO 40 TeV IN THE SUPERNOVA REMNANT CASSIOPEIA A. *The Astrophysical Journal Letters*, 487:L97–L100, 1997.

T. Amano and M. Hoshino. A Critical Mach Number for Electron Injection in Collisionless Shocks. *Physical Review Letters*, 104(18):181102, 2010.

E. Amato. The origin of galactic cosmic rays. *International Journal of Modern Physics D*, 23 (07):1430013, 2014.

E. Amato and P. Blasi. Non-linear particle acceleration at non-relativistic shock waves in the presence of self-generated turbulence. *Monthly Notices of the Royal Astronomical Society*, 371:1251–1258, 2006.

E. Amato and P. Blasi. A general solution to non-linear particle acceleration at non-relativistic shock waves. *Monthly Notices of the Royal Astronomical Society*, 364:L76–L80, 2005.

E. Amato, P. Blasi and S. Gabici. Kinetic approaches to particle acceleration at cosmic ray modified shocks. *Monthly Notices of the Royal Astronomical Society*, 385:1946–1958, 2008.

B. Aschenbach. Discovery of a young nearby supernova remnant. *Nature*, 396:141–142, 1998.

W. I. Axford, E. Leer and G. Skadron. The acceleration of cosmic rays by shock waves. In *International Cosmic Ray Conference*, volume 11 of *International Cosmic Ray Conference*, pages 132–137, 1977.

W. I. Axford, E. Leer and J. F. McKenzie. The structure of cosmic ray shocks. *Astronomy and Astrophysics*, 111:317–325, 1982.

J. Ballet. X-ray synchrotron emission from supernova remnants. *Advances in Space Research*, 37:1902–1908, 2006.

A. Bamba, R. Yamazaki, M. Ueno, et al. Small-Scale Structure of the SN 1006 Shock with Chandra Observations. *The Astrophysical Journal*, 589:827–837, 2003.

A. Bamba, R. Yamazaki, M. Ueno, et al. Fine structure of the thermal and non-thermal X-rays in the SN 1006 shell. *Advances in Space Research*, 33(4):376–380, 2004.

A. Bamba, R. Yamazaki, T. Yoshida, et al. A Spatial and Spectral Study of Nonthermal Filaments in Historical Supernova Remnants: Observational Results with Chandra. *The Astrophysical Journal*, 621:793–802, 2005.

P. A. Becker and D. Kazanas. Exact Expressions for the Critical Mach Numbers in the Two-Fluid Model of Cosmic-Ray-modified Shocks. *The Astrophysical Journal*, 546:429–446, 2001.

A. R. Bell. The acceleration of cosmic rays in shock fronts. I. *Monthly Notices of the Royal Astronomical Society*, 182:147–156, 1978.

A. R. Bell. Turbulent amplification of magnetic field and diffusive shock acceleration of cosmic rays. *Monthly Notices of the Royal Astronomical Society*, 353:550–558, 2004.

E. G. Berezhko and D. C. Ellison. A Simple Model of Nonlinear Diffusive Shock Acceleration. *The Astrophysical Journal*, 526:385–399, 1999.

E. G. Berezhko and H. J. Völk. Direct evidence of efficient cosmic ray acceleration and magnetic field amplification in Cassiopeia A. *Astronomy and Astrophysics*, 419:L27–L30, 2004.

E. G. Berezhko and H. J. Völk. Hadronic versus leptonic origin of the gamma-ray emission from supernova remnant RX J1713. 7-3946. *Astronomy and Astrophysics*, 492(3):695–701, 2008.

R. D. Blandford. On the mediation of a shock front by Fermi-accelerated cosmic rays. *The Astrophysical Journal*, 238:410, 1980.

R. D. Blandford and J. P. Ostriker. Particle acceleration by astrophysical shocks. *The Astrophysical Journal Letters*, 221:L29–L32, 1978.

P. Blasi. A semi-analytical approach to non-linear shock acceleration. *Astroparticle Physics*, 16: 429–439, 2002.

P. Blasi. Nonlinear shock acceleration in the presence of seed particles. *Astroparticle Physics*, 21:45–57, 2004.

P. Blasi, S. Gabici and G. Vannoni. On the role of injection in kinetic approaches to non-linear particle acceleration at non-relativistic shock waves. *Monthly Notices of the Royal Astronomical Society*, 361:907–918, 2005.

P. Blasi. Origin of Galactic Cosmic Rays. *Nuclear Physics B Proceedings Supplements*, 239: 140–147, 2013.

P. Blasi. Recent Results in Cosmic Ray Physics and Their Interpretation. *Brazilian Journal of Physics*, 44(5):426–440, 2014.

K. J. Borkowski, J. Rho, S. P. Reynolds, et al. Thermal and Nonthermal X-Ray Emission in SNR RCW 86. *The Astrophysical Journal*, 550:334–345, 2001.

D. Caprioli. Understanding hadronic gamma-ray emission from supernova remnants. J. Cosmology Astropart. Phys., 5:026, 2011.

D. Caprioli. Cosmic-ray acceleration in supernova remnants: non-linear theory revised. J. Cosmology Astropart. Phys., 7:038, 2012.

D. Caprioli, P. Blasi, E. Amato, et al. Dynamical feedback of self-generated magnetic fields in cosmic ray modified shocks. *Monthly Notices of the Royal Astronomical Society*, 395:895–906, 2009.

D. Caprioli, E. Amato and P. Blasi. Non-linear diffusive shock acceleration with free escape boundary. *Astroparticle Physics*, 33:307–311, 2010.

D. Caprioli, H. Kang, A. E. Vladimirov, et al. Comparison of different methods for non-linear diffusive shock acceleration. *Monthly Notices of the Royal Astronomical Society*, 407:1773–1783, 2010.

G. Cassam-Chenaï, J. P. Hughes, E. M. Reynoso, et al. Morphological Evidence for Azimuthal

Variations of the Cosmic-Ray Ion Acceleration at the Blast Wave of SN 1006. *The Astrophysical Journal*, 680:1180–1197, 2008.

R. B. Dahlburg, C. R. Devore, J. M. Picone, et al. Nonlinear evolution of radiation-driven thermally unstable fluids. *The Astrophysical Journal*, 315:385–407, 1987.

A. Decourchelle, D. C. Ellison and J. Ballet. Thermal X-Ray Emission and Cosmic-Ray Production in Young Supernova Remnants. *The Astrophysical Journal Letters*, 543:L57–L60, 2000.

R. L. Dewar. Interaction between Hydromagnetic Waves and a Time-Dependent, Inhomogeneous Medium. *Physics of Fluids*, 13(11):2710, 1970.

D. J. Donohue, G. P. Zank and G. M. Webb. Time-dependent evolution of cosmic-ray-modified shock structure: Transition to steady state. *The Astrophysical Journal*, 424:263–274, 1994.

L. O. Drury. An introduction to the theory of diffusive shock acceleration of energetic particles in tenuous plasmas. *Reports on Progress in Physics*, 46:973–1027, 1983.

L. O. Drury and T. P. Downes. Turbulent magnetic field amplification driven by cosmic ray pressure gradients. *Monthly Notices of the Royal Astronomical Society*, 427:2308–2313, 2012.

L. O. Drury and S. A. E. G. Falle. On the Stability of Shocks Modified by Particle Acceleration. *Monthly Notices of the Royal Astronomical Society*, 223:353, 1986.

L. O. Drury and J. H. Völk. Hydromagnetic shock structure in the presence of cosmic rays. *The Astrophysical Journal*, 248:344–351, 1981.

G. Dubner and E. Giacani. Radio emission from supernova remnants. *The Astronomy and Astrophysics Review*, 23:3, 2015.

D. C. Ellison and D. Eichler. Monte Carlo shock-like solutions to the Boltzmann equation with collective scattering. *The Astrophysical Journal*, 286:691–701, 1984.

D. C. Ellison, D. J. Patnaude, P. Slane, et al. Efficient Cosmic Ray Acceleration, Hydrodynamics, and Self-Consistent Thermal X-Ray Emission Applied To Supernova Remnant RX J1713.7-3946. *The Astrophysical Journal*, 712(1):287–293, 2010.

R. Enomoto, T. Tanimori, T. Naito, et al. The acceleration of cosmic-ray protons in the supernova remnant RX J1713.7-3946. *Nature*, 416:823–826, 2002.

E. Fermi. On the Origin of the Cosmic Radiation. *Physical Review*, 75:1169–1174, 1949.

A. Frank, T. W. Jones and D. Ryu. Oblique magnetohydrodynamic cosmic-ray-modified shocks: Two-fluid numerical simulations. *The Astrophysical Journal Supplement*, 90:975–980, 1994.

A. Frank, T. W. Jones and D. Ryu. Time-dependent simulation of oblique MHD cosmic-ray shocks using the two-fluid model. *The Astrophysical Journal*, 441:629–643, 1995.

Y. Fukui. Molecular and atomic gas in the young TeV gamma-ray SNRs RX J1713.7-3946 and RX J0852.0-4622; evidence for the hadronic production of gamma-rays. *arXiv:1304.1261*, 2013.

T. K. Gaisser. *Cosmic rays and particle physics*. 1990.

F. Giordano, M. Naumann-Godo, J. Ballet, et al. FERMI LARGE AREA TELESCOPE DETECTION OF THE YOUNG SUPERNOVA REMNANT TYCHO. *The Astrophysical Journal*, 744(1):L2, 2012.

A. Giuliani, M. Cardillo, M. Tavani, et al. Neutral Pion Emission From Accelerated Protons in the Supernova Remnant W44. *The Astrophysical Journal*, 742(2):L30, 2011.

L. J. Gleeson and W. I. Axford. Cosmic Rays in the Interplanetary Medium. *The Astrophysical Journal Letters*, 149:L115, 1967.

D. A. Green. A catalogue of 294 Galactic supernova remnants. *Bulletin of the Astronomical Society of India*, 42(2):47–58, 2014.

A. F. Heavens. Particle acceleration in shocks - The effect of finite cosmic-ray pressure on the energy distribution. *Monthly Notices of the Royal Astronomical Society*, 204:699–708, 1983.

E. A. Helder, J. Vink, C. G. Bassa, et al. Measuring the Cosmic-Ray Acceleration Efficiency of a Supernova Remnant. *Science*, 325:719–, 2009.

E. A. Helder, D. Kosenko and J. Vink. Cosmic-ray Acceleration Efficiency versus Temperature Equilibration: The Case of SNR 0509-67.5. *The Astrophysical Journal Letters*, 719:L140, 2010.

V. F. Hess. Observations in low level radiation during seven free balloon flights. *PHYSIKALISCHE ZEITSCHRIFT*, 13:1084–1091, 1912.

J. P. Hughes, C. E. Rakowski and A. Decourchelle. Electron Heating and Cosmic Rays at a Supernova Shock from Chandra X-Ray Observations of 1E 0102.2-7219. *The Astrophysical Journal Letters*, 543:L61–L65, 2000.

J. R. Jokipii. Propagation of cosmic rays in the solar wind. *Reviews of Geophysics and Space Physics*, 9:27–87, 1971.

F. C. Jones and D. C. Ellison. The plasma physics of shock acceleration. *Space Science Reviews*, 58:259–346, 1991.

T. W. Jones and H. Kang. Time-dependent evolution of cosmic-ray-mediated shocks in the two-fluid model. *The Astrophysical Journal*, 363:499–514, 1990.

H. Kang and T. W. Jones. Diffusive cosmic-ray acceleration - Two-fluid models with in situ injection. *The Astrophysical Journal*, 353:149–158, 1990.

H. Kang and T. W. Jones. Efficiency of Nonlinear Particle Acceleration at Cosmic Structure Shocks. *The Astronomical Journal*, 620:44–58, 2005.

H. Kang and T. W. Jones. Self-similar evolution of cosmic-ray-modified quasi-parallel plane shocks. *Astroparticle Physics*, 28:232–246, 2007.

H. Kang, T. W. Jones and U. D. J. Gieseler. Numerical Studies of Cosmic-Ray Injection and Acceleration. *The Astrophysical Journal*, 579:337–358, 2002.

H. Kang and T. W. Jones. Diffusive Shock Acceleration in Oblique Magnetohydrodynamic Shocks: Comparison with Monte Carlo Methods and Observations. *The Astronomical Journal*, 476:875, 1997.

K. Koyama, R. Petre, E. V. Gotthelf, et al. Evidence for shock acceleration of high-energy electrons in the supernova remnant SN1006. *Nature*, 378:255–258, 1995.

K. Koyama, K. Kinugasa, K. Matsuzaki, et al. Discovery of Non-Thermal X-Rays from the Northwest Shell of the New SNR RX J1713.7-3946: The Second SN 1006? *Publications of the Astronomical Society of Japan*, 49:L7–L11, 1997.

P. O. Lagage and C. J. Cesarsky. The maximum energy of cosmic rays accelerated by supernova shocks. *Astronomy and Astrophysics*, 125:249–257, 1983.

J. S. Lazendic, P. O. Slane, B. M. Gaensler, et al. A High-Resolution Study of Nonthermal Radio and X-Ray Emission from Supernova Remnant G347.3-0.5. *Astrophysical Journal*, 602: 271–285, 2004.

I. Lerche. Unstable Magnetosonic Waves in a Relativistic Plasma. *The Astrophysical Journal*, 147:689, 1967.

M. A. Malkov. Analytic Solution for Nonlinear Shock Acceleration in the Bohm Limit. *The Astrophysical Journal*, 485:638, 1997.

M. A. Malkov. Bifurcation, Efficiency, and the Role of Injection in Shock Acceleration with the Bohm Diffusion. *The Astrophysical Journal*, 491:584, 1997.

M. A. Malkov and L. O. Drury. Nonlinear theory of diffusive acceleration of particles by shock waves. *Reports on Progress in Physics*, 64:429–481, 2001.

M. A. Malkov and H. J. Völk. Theory of ion injection at shocks. *Astronomy and Astrophysics*, 300:605, 1995.

M. A. Malkov and H. J. Völk. Renormalized Two-Fluid Hydrodynamics of Cosmic-Ray–modified Shocks. *The Astrophysical Journal*, 473:347, 1996.

M. A. Malkov, P. H. Diamond and H. J. Völk. Critical Self-Organization of Astrophysical Shocks. *The Astrophysical Journal Letters*, 533:L171–L174, 2000.

J. F. McKenzie and H. J. Völk. Non-linear theory of cosmic ray shocks including self-generated Alfven waves. *Astronomy and Astrophysics*, 116:191–200, 1982.

J. F. McKenzie and K. O. Westphal. Transmission of Alfven waves through the Earth's bow shock. *Planetary and Space Science*, 17:1029, 1969.

R. A. Mewaldt. Solar Energetic Particle Composition, Energy Spectra, and Space Weather. *Space Science Reviews*, 124:303–316, 2006.

R. A. Mewaldt, C. M. S. Cohen, A. W. Labrador, et al. Proton, helium, and electron spectra during the large solar particle events of October-November 2003. *Journal of Geophysical Research (Space Physics)*, 110:A09S18, 2005.

M. Mond and L. O. Drury. Acoustic emission and corrugational instability of shocks modified by strong particle acceleration. *Astronomy and Astrophysics*, 332:385–390, 1998.

G. Morlino and D. Caprioli. Strong evidence for hadron acceleration in Tycho's supernova remnant. *Astronomy and Astrophysics*, 538:A81, 2012.

G. Morlino, E. Amato and P. Blasi. Gamma-ray emission from SNR RX J1713.7 − 3946 and the origin of galactic cosmic rays. *Monthly Notices of the Royal Astronomical Society*, 392: 240–250, 2009.

E. N. Parker. The passage of energetic charged particles through interplanetary space. Planet. Space Sci., 13:9, 1965.

B. Reville, J. G. Kirk and P. Duffy. Steady-State Solutions in Nonlinear Diffusive Shock Acceleration. *The Astrophysical Journal*, 694:951–958, 2009.

S. P. Reynolds and D. C. Ellison. Electron acceleration in Tycho's and Kepler's supernova remnants - Spectral evidence of Fermi shock acceleration. *The Astrophysical Journal*, 399: L75, 1992.

E. L. Rubin and S. Z. Burstein. Difference Methods for the Inviscid and Viscous Equations of a Compressible Gas. *Journal of Computational Physics*, 2:178, 1967.

D. Ryu, H. Kang and T. W. Jones. The stability of cosmic-ray-dominated shocks - A secondary instability. *The Astrophysical Journal*, 405:199–206, 1993.

M. Scholer. Diffuse ions at a quasi-parallel collisionless shock - Simulations. *Geophysics Research Letters*, 17:1821–1824, 1990.

N. Shimada, T. Terasawa, M. Hoshino, et al. Diffusive Shock Acceleration of Electrons at an Interplanetary Shock Observed on 21 Feb 1994. *Astrophysics and Space Science*, 264:481–488, 1999.

J. Skilling. Cosmic ray streaming. I - Effect of Alfven waves on particles. *Monthly Notices of the Royal Astronomical Society*, 172:557–566, 1975.

J. Skilling. Cosmic ray streaming. II - Effect of particles on Alfven waves. *Monthly Notices of the Royal Astronomical Society*, 173:245–254, 1975.

P. Slane, S.-H. Lee, D. C. Ellison, et al. A CR-HYDRO-NEI MODEL OF THE STRUCTURE AND BROADBAND EMISSION FROM TYCHO'S SUPERNOVA REMNANT. *The Astrophysical Journal*, 783(1):33, 2014.

P. Slane, B. M. Gaensler and T. Dame. Nonthermal x-ray emission from the shell-type supernova remnant G347.3-0.5. *The Astrophysical Journal*, 525:357–367, 1999.

P. Slane, J. P. Hughes, R. J. Edgar, et al. RX J0852.0-4622: Another Nonthermal Shell-Type Supernova Remnant (G266.2-1.2). *The Astronomical Journal*, 20:814–819, 2001.

T. Sugiyama, M. Fujimoto and T. Mukai. Quick ion injection and acceleration at quasi-parallel shocks. *Journal of Geophysical Research*, 106:21657–21674, 2001.

M. Tavani, A. Giuliani, A. W. Chen, et al. Direct Evidence for Hadronic Cosmic-Ray Acceleration in the Supernova Remnant Ic 443. *The Astrophysical Journal Letters*, 710(2):L151–L155, 2010.

T. Terasawa, K. Maezawa, M. Hoshino, et al. Observation of a 'Cosmic-Ray-Modified' Interplanetary Shock. *Proceedings of the 26th International Cosmic Ray Conference*, 6:528–531, 1999.

T. Terasawa, K. Nakata, M. Oka, et al. Determination of shock parameters for the very fast interplanetary shock on 29 October 2003. *Journal of Geophysical Research (Space Physics)*, 110(A9):A09S12, 2005.

T. Terasawa, M. Oka, K. Nakata, et al. 'Cosmic-ray-mediated' interplanetary shocks in 1994 and 2003. *Advances in Space Research*, 37:1408–1412, 2006.

Y. Uchiyama, F. A. Aharonian and T. Takahashi. Fine-structure in the nonthermal X-ray emission of SNR RX J1713.7-3946 revealed by Chandra. 400:567–574, 2003.

Y. Uchiyama, F. A. Aharonian, T. Tanaka, et al. Extremely fast acceleration of cosmic rays in a supernova remnant. *Nature*, 449:576–578, 2007.

Y. Uchiyama and F. A. Aharonian. Fast Variability of Nonthermal X-Ray Emission in Cassiopeia A: Probing Electron Acceleration in Reverse-Shocked Ejecta. *The Astrophysical Journal*, 677 (2):L105–L108, 2008.

Y. Uchiyama, R. D. Blandford, S. Funk, et al. Gamma-Ray Emission From Crushed Clouds in Supernova Remnants. *The Astrophysical Journal*, 723(1):L122–L126, 2010.

R. Vainio and R. Schlickeiser. Self-consistent Alfvén-wave transmission and test-particle acceleration at parallel shocks. *Astronomy and Astrophysics*, 343:303–311, 1999.

S. v. d. Bergh and G. A. Tammann. Galactic and Extragalactic Supernova Rates. *Annual Review of Astronomy and Astrophysics*, 29(1):363–407, 1991.

H. A. van der Vorst. Bi-cgstab: A fast and smoothly converging variant of bi-cg for the solution of nonsymmetric linear-systems. *SIAM Journal on Scientific and Statistical Computing*, 13 (2):631–644, 1992.

J. Vink and J. M. Laming. On the Magnetic Fields and Particle Acceleration in Cassiopeia A. *The Astrophysical Journal*, 584:758–769, 2003.

J. Vink, J. Bleeker, K. van der Heyden, et al. The X-Ray Synchrotron Emission of RCW 86 and the Implications for Its Age. *The Astrophysical Journal Letters*, 648:L33–L37, 2006.

A. Vladimirov, D. C. Ellison and A. Bykov. Nonlinear Diffusive Shock Acceleration with Magnetic Field Amplification. *The Astrophysical Journal*, 652:1246–1258, 2006.

A. Y. Wagner, S. A. E. G. Falle, T. W. Hartquist, et al. Two-fluid models of cosmic ray modified radiative shocks. *Astronomy and Astrophysics*, 452:763–771, 2006.

A. Y. Wagner, S. A. E. G. Falle and T. W. Hartquist. Two-fluid models of cosmic-ray modified radiative shocks including the effects of an acoustic instability. *Astronomy and Astrophysics*, 463:195–201, 2007.

A. Y. Wagner, J.-J. Lee, J. C. Raymond, et al. A Cosmic-Ray Precursor Model for a Balmer-Dominated Shock in Tycho's Supernova Remnant. *The Astrophysical Journal*, 690:1412–1423, 2009.

J. S. Warren, J. P. Hughes, C. Badenes, et al. Cosmic-Ray Acceleration at the Forward Shock in Tycho's Supernova Remnant: Evidence from Chandra X-Ray Observations. *The Astrophysical Journal*, 634:376–389, 2005.

G. M. Webb. The structure of oblique MHD cosmic-ray shocks. *Astronomy and Astrophysics*, 127:97–112, 1983.

G. M. Webb, L. O. Drury and H. J. Völk. Cosmic-ray shock acceleration in oblique MHD shocks. *Astronomy and Astrophysics*, 160:335–346, 1986.

R. Yamazaki, T. Yoshida, T. Terasawa, et al. Constraints on the diffusive shock acceleration from the nonthermal X-ray thin shells in SN 1006 NE rim . *Astronomy and Astrophysics*, 416: 595–602, 2004.

R. Yamazaki, K. Kohri and H. Katagiri. Gamma-ray spectrum of RX J1713. 7-3946 in the Fermi era and future detection of neutrinos. *Astronomy and Astrophysics*, 495(1):9–13, 2009.

G. P. Zank, G. M. Webb and D. J. Donohue. Particle injection and the structure of energetic-particle-modified shocks. *The Astrophysical Journal*, 406:67–91, 1993.

V. N. Zirakashvili and F. A. Aharonian. Nonthermal Radiation of Young Supernova Remnants: The Case of RX J1713.7-3946. *The Astrophysical Journal*, 708:965–980, 2010.